The Stone Jug Fault: Facilitating Sinistral Displacement Transfer During the M_w7.8 Kaikōura Earthquake

By

Bradley Scott

30.6.2019

A thesis submitted in partial fulfilment of the requirements for

the degree of Master of Science in Geology at the

University of Canterbury

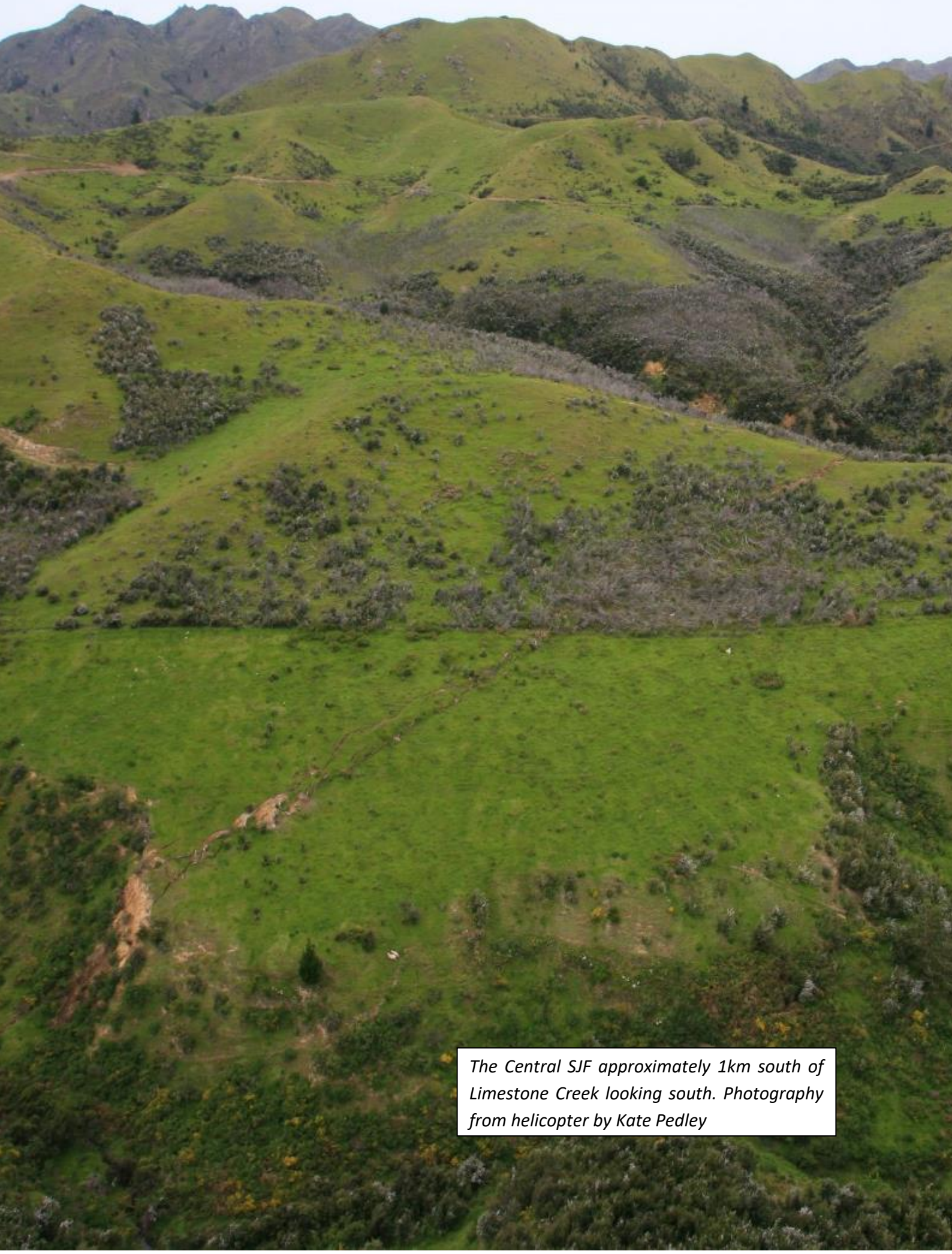

The Central SJF approximately 1km south of Limestone Creek looking south. Photography from helicopter by Kate Pedley

Abstract

The Stone Jug Fault (SJF) ruptured during the November 14th, 2016 (at 12:02 am), M_w 7.8 Kaikōura Earthquake which initiated ~40 km west-southwest of the study area, at a depth of approximately 15 km. Preliminary post-earthquake mapping indicated that the SJF connects the Conway-Charwell and Hundalee faults, which form continuous surface rupture, however, detailed study of the SJF had not been undertaken prior to this thesis due to its remote location and mountainous topography. The SJF is 19 km long, has an average strike of ~160° and generally carries approximately equal components of sinistral and reverse displacement. The primary fault trace is sigmoidal in shape with the northern and southern tips rotating in strike from NNW to NW, as the SJF approaches the Hope and Hundalee faults. It comprises several steps and bends and is associated with many (N=48) secondary faults, which are commonly near irregularities in the main fault geometry and in a distributed fault zone at the southern tip. The SJF is generally parallel to Torlesse basement bedding where it may utilise pre-existing zones of weakness. Horizontal, vertical and net displacements range up to 1.4 m, with displacement profiles along the primary trace showing two main maxima separated by a minima towards the middle and ends of the fault. Average net displacement along the primary trace is ~0.4m, with local changes in relative values of horizontal and vertical displacement at least partly controlled by fault strike. Two trenches excavated across the northern segment of the fault revealed displacement of mainly Holocene stratigraphy dated using radiocarbon (N=2) and OSL (N=4) samples. Five surface-rupturing paleoearthquakes displaying vertical displacements of <1 m occurred at: 11,000±1000, 7500±1000, 6500±1000, 3500±100 and 3 (2016 Kaikōura) years BP. These events produce an average slip rate since ~11 ka of 0.2-0.4 mm/yr and recurrence intervals of up to 5500 years with an average recurrence interval of 2750 yrs. Comparison of these results with unpublished trench data suggests that synchronous rupture of the Hundalee, Stone Jug, Conway-Charwell, and Humps faults at ~3500 yrs BP cannot be discounted and it is possible that multi-fault ruptures in north Canterbury are more common than previously thought.

Acknowledgements

A lot of people have helped make this thesis what it is and supported me through the process. I would firstly like to thank my principal supervisor Andy Nicol for his valuable time, insight, and support in making this thesis happen. You have been a great source of need clarity. I would also like to thank Jarg Pattenga and Tim Stalh who have also been a great help and cheerful faces. Thank you to all those that aided in the trenching project: Dale Cusack, Kate Pedly, Jarg Pettinga, Andy Nicol, and Rinze Schuurmans. Thanks for suffering with me in the heat, it was most enjoyable. To Anekant Wandres and Sacha Baldwin your technical support is always appreciated. I would also like to thank EQC for providing funding for research like this to happen in such an effortless manner. I hope it is of use. I would like to thank my parents for their endless support throughout my life and tertiary studies. You are always there for me and I appreciate it. A final thanks to my wonderful partner Hannah Lynch for putting up with me while I pushed through the final days of this process, I am indebted.

Table of Contents

1. Introduction 1

1.1. Research motivation 1

1.2. Kaikōura Earthquake 2

1.3. Tectonic setting 3

1.3.1. NCD 2016 fault ruptures 4

1.4. Stratigraphy of study area 9

1.5. Thesis outline 11

2. Geometry and Kinematics of Fault Rupture 13

2.1. Introduction 13

2.2. Methods 14

2.2.1. Fault surface mapping and displacements 14

2.2.2. Near-surface fault strike and dip 15

2.2.3 Geomorphic and 3D photogrammetry maps 17

2.3. Fault geometry 18

2.3.1. Overview 18

2.3.2. Primary fault trace 20

2.3.2. Secondary fault traces 23

2.3.3. Fault strikes and dips 24

2.4. Kinematics 24

2.4.1. Overview 24

2.4.2. Displacement profiles 28

2.4.3. Fault orientations influence on the direction of lateral motion 29

2.4.4. Right-lateral displacement of primary trace 32

2.4.5. On-fault and off-fault displacement 34

2.5. Discussion 36
2.5.1. Limitations and errors 36
2.5.2. Prehistoric SJF ruptures 38
2.6. Conclusions 39
3. Relationship of fault geometry to basement bedding 40
3.1. Introduction 40
3.2. Methodology 42
3.3. Observations from maps 44
3.4. Box-sample analysis 45
3.5. Discussion 47
3.5.1. Limitations and errors 47
3.5.2. SJF and the transpressional fault model 47
3.6. Conclusion 49
4. Paleoseismic history of the Stone Jug Fault 50
4.1. Introduction 50
4.2. Data and Methods 51
4.2.1. Trench locations and methods 51
4.3. SJT-1 Observations 57
4.3.1. Unit descriptions 57
4.3.2. Fault geometry and displacement 61
4.4. SJT-2 Observations 63
4.4.1. Unit descriptions 63
4.4.2. Fault geometry and displacement 67
4.5. Paleoseismic history 70
4.6. Discussion 73
4.6.1. Assumptions and limitations 73
4.6.2. Long-term displacement rates and recurrence intervals 74
4.6.3. Relations of the SJF to other faults 76

4.7. Conclusions 77

5. Discussion and Conclusion 79

5.1. Chapter Conclusions 79

5.2. Was Kaikōura a typical event for the SJF 80

5.3. The SJF interaction with nearby faults 81

5.4. Further research opportunities 81

Appendix 1 - Collection of photographs depicting field work 83

Appendix 2 - Field data collected 91

Appendix 3 – OSL dating lab report 95

Appendix 4 – Radiocarbon dating lab report 105

References 108

List of Figures

Figure 1.1: Simplified surface traces from the 2016 Kaikōura rupture 3

Figure 1.2: Overview of faults ruptured in the NCD during Kaikōura 5

Figure 1.3: Active faults with a historical rupture, surrounding the SJF 6

Figure 1.4: cross section of interpretation of the Monkey face area 10

Figure 2.1: Trigonometric method for calculating near surface true strike 17

Figure 2.2: Overview map 2016 SJF surface traces and geometry 19

Figure 2.3: Map of 2016 surface traces of the Southern SJF and Hundalee 22

Figure 2.4: Definition of primary and secondary traces 23

Figure 2.5: Overview map SJF kinematics 26

Figure 2.6: Horizontal (A), Vertical (B), and Net (C), SJF displacement profiles 27

Figure 2.7: Direction of lateral fault movement by orientation 29

Figure 2.8: lateral sense of individual fault traces 31

Figure 2.9: 3D photogrammetry showing regional displacement in three planes 33

Figure 2.10: 3D photogrammetry / displacement profile of eastern secondary faults 36

Figure 3.1: Geological and structural map of the SJF area 41

Figure 3.2: Method of interpreting strike ridges from LiDAR 42

Figure 3.3: Data sampling boxes 44

Figure 3.4: Local fault orientation relative to local bedding orientation 45

Figure 4.1: SJF trench locations and local kinematics 53

Figure 4.2: Photographs of excavated trenches 55

Figure 4.3: Photograph of OSL sampling method 56

Figure 4.4: Photograph of SJT – 1 east wall 57

Figure 4.5: log of SJT – 1 west wall 59

Figure 4.6: log of SJT – 1 east wall 60

Figure 4.7: Photograph of SJT – 2 south-eastern wall 63

Figure 4.8: log of SJT – 2 south-eastern wall 65

Figure 4.9: log of SJT – 2 north-western wall 66

Figure 4.10: Photograph of fault gouge in SJT -2 NW wall 68

Figure 4.11: Rupture history of the SJF 69

Figure 4.12: Temporal evolution of SJT – 1 west wall 73

Figure 4.13: Map of total displacement at the Conway - Torlesse boundary 76

Table of Tables

Table 4.1: ^{14}C radio-carbon age dates. 62

Table 4.2: OSL age dates and key processing values 62

Chapter One: Introduction

1.1. Research motivation

Earthquakes represent a significant natural hazard for much of New Zealand (e.g., Stirling et al., 2012). On geological timescales, these earthquakes are recorded by, and responsible for, landscape evolution. Geological studies of time intervals of 100s to millions of years rarely provide information on individual earthquakes. Paleoseismic studies can provide data on prehistorical earthquakes, but these data are incomplete even for faults that have been studied in detail (McCalpin, 2009; Nicol et al., 2016). By contrast, historical events can provide detailed information on the rupture and displacement patterns of earthquakes and how they are related to events or stress changes on nearby faults (e.g., Stein et al., 1997). However, these data represent a small window of seismic activity for individual faults. Combining historical and prehistorical data for faults that have ruptured the ground surface, provides a means of reducing the sampling biases associated with short (last 180 yrs) and long (>10, 000 yrs) term data.

This thesis examines the 2016 Kaikōura Earthquake rupture of the Stone Jug Fault (SJF) and its mainly Holocene history of earthquakes. The SJF was one of at least 20 faults that ruptured the ground surface during the earthquake (N. J. Litchfield et al., 2018) (Fig. 1.1). South of Kaikōura many of these faults, including the SJF, were either not known to exist or only partly mapped prior to the earthquake. Prior to the Kaikōura Earthquake, only a quarter of the SJF had been mapped (Rattenbury et al., 2006; Barrell and Townsend, 2012), and very little was known about the history of displacement accumulation and earthquakes on the fault. Surface ruptures during Kaikōura provide an excellent opportunity to understand better the geometries and displacement patterns of these faults and how they interact on a timescale of individual earthquakes.

This thesis sets out to improve understanding of the geometry, kinematics and Late Quaternary earthquake history of the SJF. The thesis is based on data from detailed fault trace maps generated using field observations and remote sensing (LiDAR, orthophoto and 3D photogrammetry), field and remote sensing displacement measurements and trenching of the active trace. The thesis provides a piece of the puzzle contributing to a clearer understanding of the 2016 earthquake on the SJF. The results of this study can be combined with data from

two postgraduate theses at the University of Canterbury to constrain the active tectonics of the North Canterbury (tectonic) Domain (NCD).

1.2. Kaikōura Earthquake

On November 14th, 2016, at 12:02, a M_w 7.8 magnitude earthquake struck 15 km north-east of Culverden in New Zealand, at a depth of approximately 15km (Kaiser et al., 2017). Relocation of the earthquake epicentre suggests that it initiated on The Humps Fault (Nicol et al., 2018) and propagated NE. The earthquake lasted for about 2 minutes and when it finished had ruptured at least 20 faults over a distance of ~165km (Duputel & Rivera, 2017; N. J. Litchfield et al., 2018). It is often referred to as the most complex earthquake ever recorded (Cesca et al., 2017; Hamling et al., 2017; Shi et al., 2017; Wang et al., 2018). It was felt across the majority of New Zealand, causing substantial damage as far north as the Wellington CBD (Kaiser et al., 2017; Woods et al., 2017). The earthquake sequence ruptured faults with a range of orientations, slip types and slip magnitudes. Surface ruptures exhibited strike-slip (right and left lateral), reverse and normal displacements of up to 12 m. The larger displacements were observed north of the Hope Fault where they occurred on a handful of faults in the Marlborough fault system (MFS). These faults displayed largely continuous surface traces in a linear pattern over a considerable distance (A. Nicol, 2018; Kearse et al., 2018; N. J. Litchfield et al., 2018). The southern faults of the North Canterbury Domain had lower 2016 displacements than the faults in the MFS and display a wide range of orientations (Nicol et al 2018). Kaikōura was complex for a range of reasons including the fact that it ruptured two fault systems with varying fault kinematics and fault displacements rates.

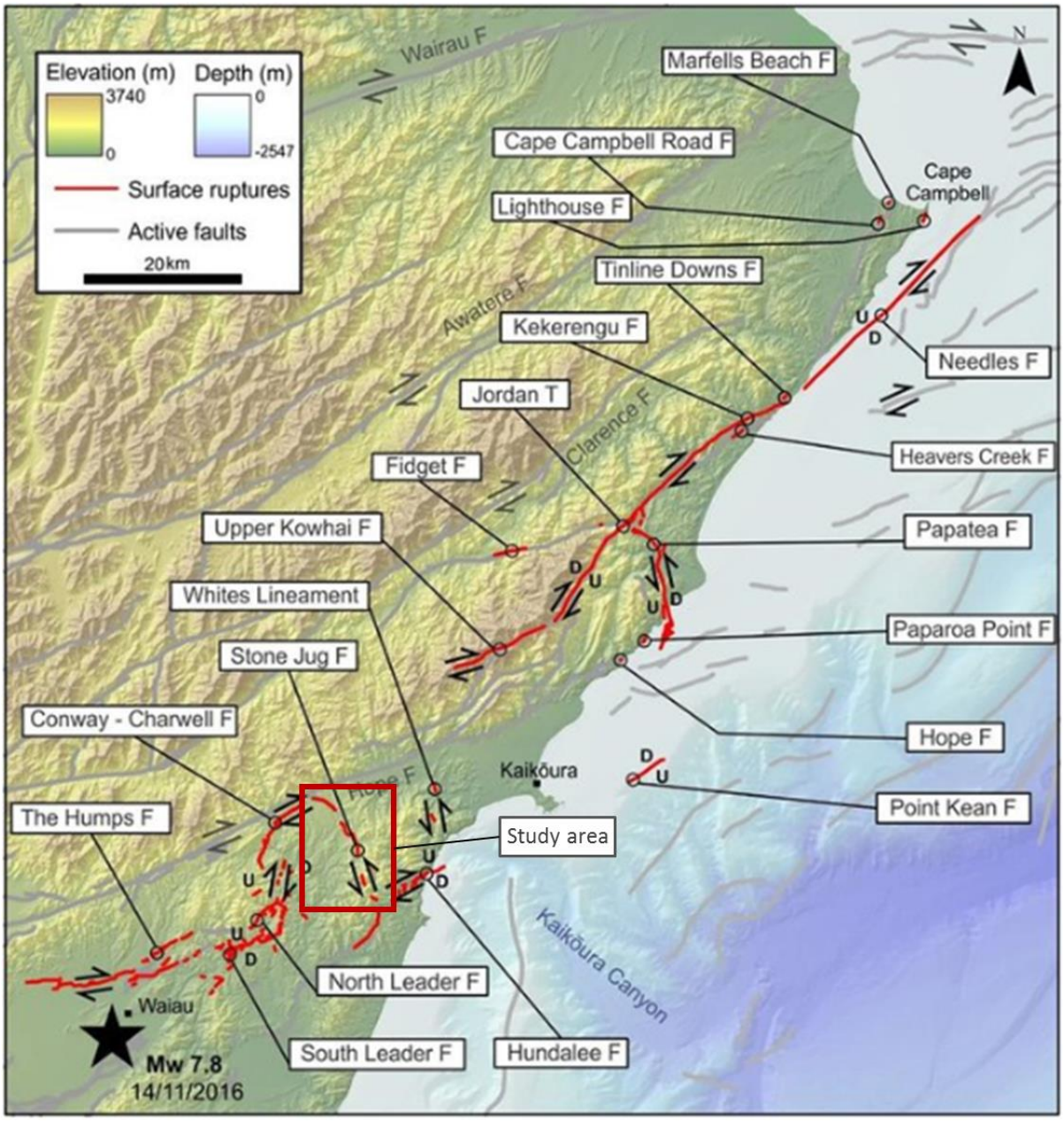

Figure 1.1: Simplified surface traces from the 2016 Kaikōura rupture. The star represents the earthquake epicentre which was at the SW end of the sequence (Stirling et al., 2017). Fault names and slip senses are indicated. Grey lines show active faults that appear not to have ruptured in the 2016 event.

1.3. Tectonic setting

The Kaikōura Earthquake resulted in slip on faults in the northeastern South Island of New Zealand that accommodate the transition from subduction east of the North Island, to continental collision and strike-slip along the Alpine fault in the South Island of New Zealand (Fig. 1.1). The MFS accommodates the transfer of the ~40 mm/yr relative plate motion from subduction to the Alpine Fault (e.g., Holt and Haines, 1995; Beavan and Haines, 2001; Pondard and Barnes, 2010; Wallace et al., 2012). The eastern MFS is underlain by the subducting Pacific Plate which extends to at least 200 km depth beneath the northern South Island (Ansell and Bannister, 1996; Eberhart-Phillips and Bannister, 2010; Eberhart-Phillips and Reyners, 2012; Williams et al., 2013). In the study area, the top of the subducted Pacific Plate is ~20-30 km beneath the surface ruptures and may define the lower limit of the upper-plate faults (Eberhart-Phillips and Bannister, 2010; Williams et al., 2013; Nicol et al., 2018).

The MFS is dominated by right-lateral strike-slip with fault displacement rates from ~3 mm/yr on the Wairau Fault in the north and up to 29 mm/yr on the Hope Fault. The Hope Fault defines the southern boundary of the system. South of the Hope Fault in the NCD, faulting and folding primarily accommodates transpression. Faults in the NCD are inferred to have low slip rates (e.g., <1 mm/yr) with total NW-SE shortening across the domain of about 3 mm/yr. As many as 50 active faults have been mapped across the NCD, however, prior to the Kaikōura Earthquake none of these faults had ruptured the ground surface historically (i.e. since 1840) (Pettinga et al. 2001; Rattenbury et al., 2006; Barrell and Townsend, 2012). Estimates of earthquake recurrence intervals for these faults are generally considered to be of the order of 5-10 kyr (Pettinga et al. 2001; Rattenbury et al., 2006; Barrell and Townsend, 2012), however, direct dating of paleoseismic events is rare.

1.3.1. NCD 2016 fault ruptures

Six main faults in the NCD ruptured during the Kaikōura Earthquake and these are (from west to east); The Humps Fault, Leader Fault, Conway-Charwell Fault, Stone Jug Fault, Hundalee fault and the Whites Fault. Preliminary accounts of the 2016 ruptures of these faults are given in Nicol et al. (2018) and Williams et al. (2018). In addition to these faults the Hope Fault appears to have accommodated minor slip (<1 m) during the 2016 earthquake. Below is a brief account of Stone Jug Fault together with the Hundalee, Conway-Charwell and Hope faults.

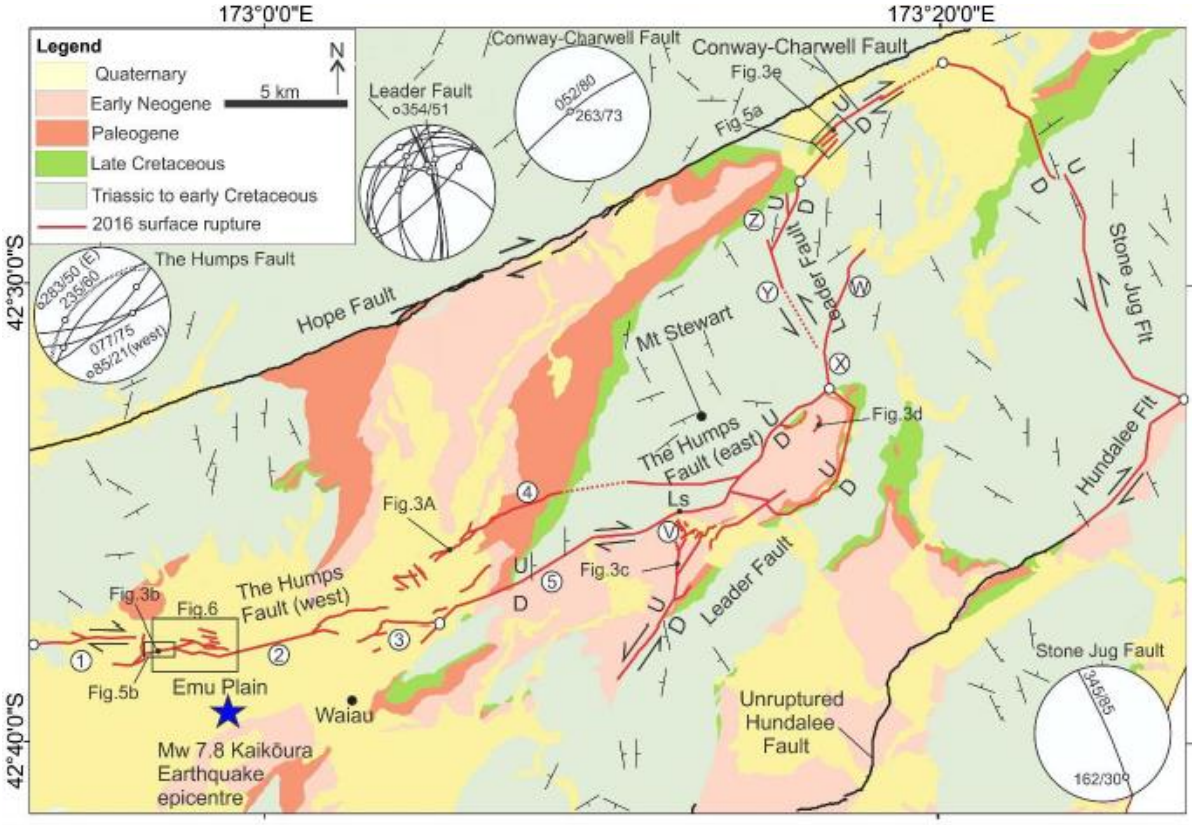

Figure 1.2: Overview of faults that ruptured in the NCD during the 2016 Kaikōura earthquake (A. Nicol, 2018). Geological units and active fault traces from Rattenbury et al. (2006). Fault traces produced by the 2016 earthquake shown by red lines. Stereonets show fault orientation and slip direction data from the faults that ruptured in 2016. For further information on this figure refer to Nicol et al. (2018).

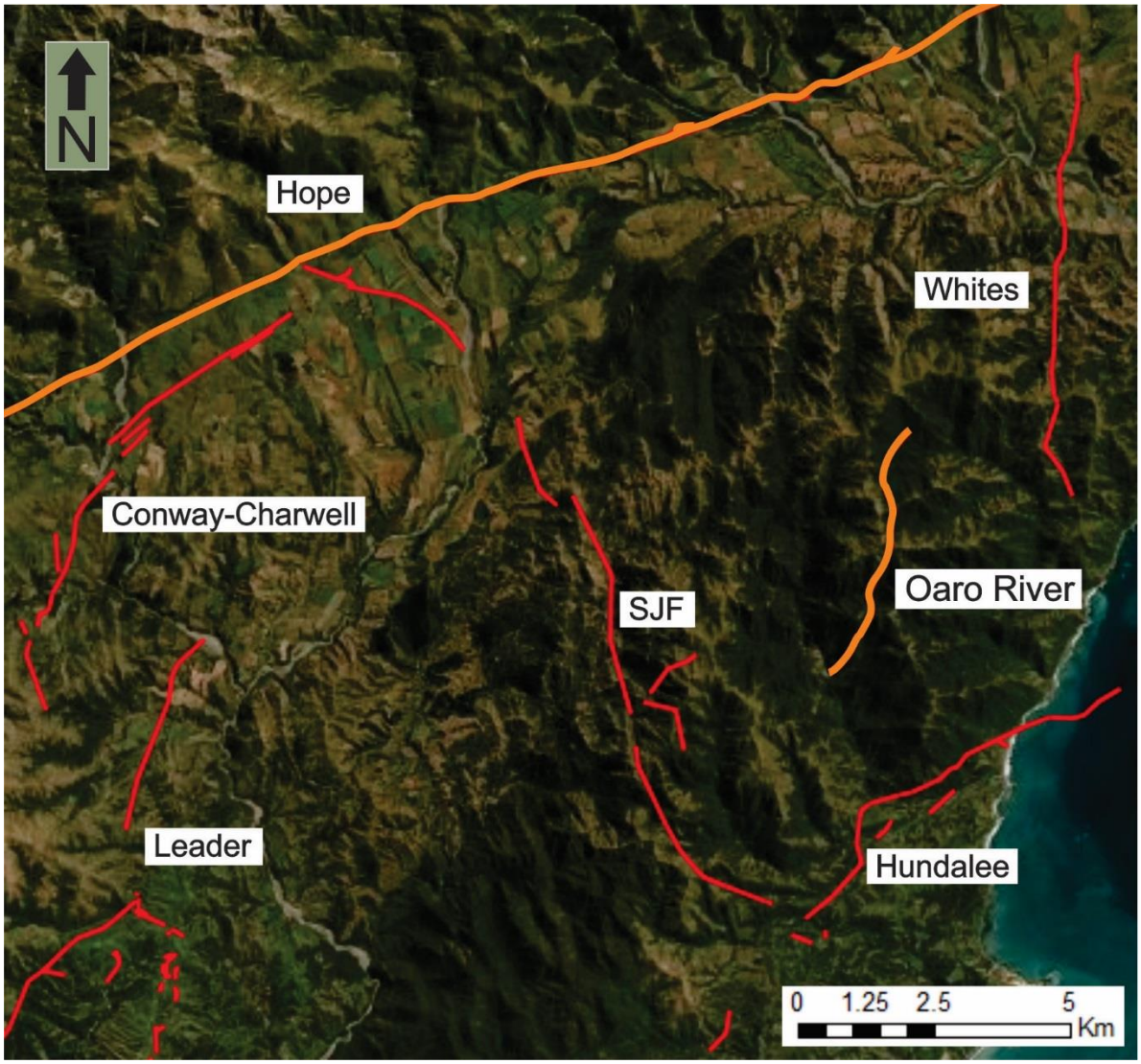

Figure 1.3: Active faults proximal to the Stone Jug Fault. Adapted from the Geonet ctive fault database (Langridge et al , 2016). Orange faults represent faults that have ruptured on the historical record and red during Kaikōura 2016. The basemap is Esri 'World Image' (2017).

Stone Jug Fault

The SJF is located in the NCD (Fig. 1.1) and until the Kaikōura Earthquake, only the northernmost 5km was known to exist. The Northern section was mapped by Crampton (1988) and Rattenbury et al. (2006) prior to the 2016 Kaikōura Earthquake, with the later authors inferring it to be active. Crampton (1988) showed the Torlesse-Late Cretaceous uniformity to be offset in an apparent left lateral sense by several hundred metres, although the timing of this displacement was not known. These authors did not perform detailed structural analysis on the SJF, and the Central and Southern sections were not known to exist.

During the 2016 earthquake initial response, preliminary field work by the University of Canterbury mapped the extent of the SJF and measured displacements at three sites on the

Northern and Central sections. Initial post-earthquake analysis during the 6 months immediately following the earthquake documented the fault to be approximately 17 km long, to strike at approximately 335° and to have a near vertical dip (Hamling et al., 2017; Nicol et al., 2018). These initial investigations indicated that the fault accommodated oblique displacements with an approximate 1:2 dip-slip to strike-slip ratio. Displacements of up to 0.9 m vertical and 0.7 m horizontal were observed. It was hypothesised that like the Leader Fault the SJF location and orientation may be determined by the dip of basement bedding, which typically appears subparallel (Nicol et al., 2018). Despite these initial investigations following the earthquake the detailed geometry and kinematics of remained unresolved. This thesis aims to resolve details of the 2016 rupture and constrain the faults paleoseismic history, which was entirely unknown prior to this thesis.

Hundalee Fault

The Hundalee Fault runs approximately perpendicular to the SJF with the Southern SJF terminating against it. Prior to 2016 a handful of studies had been conducted on the Hundalee Fault, and its entire length had been mapped within bedrock (Guyon, 1995; M. Rattenbury, 2006). Geological mapping suggests that the fault dips to the NW with about 1 km of uplift in its hangingwall and an unknown amount of strike-slip. Before the earthquake, the fault was known to be active with an inferred recurrence interval of 2-5 kyr (Barrell et al., 2015; Stirling et al., 2012; Litchfield et al., 2014). Only the northern-most 23 km of the approximately 40 – 55 km length of the Hundalee Fault ruptured during the Kaikōura Earthquake (Barrell, Canterbury, & Monitoring, 2015; Guyon, 1995; Hamling et al., 2017; Litchfield et al., 2014; Williams et al., 2018). Rupture of the fault during the earthquake was mainly confined to the area east of its intersection with the SJF and appears to have extended offshore to the southern margin of the Kaikōura Canyon (Litchfield et al., 2018; Williams et al., 2018). Fault traces that ruptured along the Hundalee Fault in 2016 are discontinuous and distributed across a zone in excess of 1 km wide. These traces typically accommodated both reverse and right-lateral displacements ranging from 0.4m to 3.7 m, with an average of approximately 0.9 m (Williams et al., 2018). In 2016 the fault accommodated oblique slip with approximately equal strike-slip and dip-slip components.

Conway-Charwell Fault

The Conway-Charwell fault is 6.5 km in length and strikes at 052°, subparallel to the Hope Fault (A. Nicol, 2018; M. Rattenbury, 2006). The fault appears to terminate against the Leader Fault and SJF in the west and east, respectively. It is located 1-1.5 km SE of the Hope Fault (Fig. 1.3). It is situated in the foothills of the Kaikōura ranges and, like the SJF, displaces Torlesse and Late Quaternary alluvial and fan gravels up to ~170 ka in age. The fault is marked by an active trace with a predominantly south-facing scarp up to ~6 m high (Bull, 1991; M. Rattenbury, 2006).

The 2016 Kaikōura earthquake is the only historical event on the fault and produced multiple continuous traces across a zone up to 0.5km wide. Fault-trace strike varies from 30° to 60° and over 20 secondary fault traces ruptured near to the main trace. The fault was typically downthrown to the southeast with vertical displacements in 2016 of up to 1.2 m (Nicol et al., 2018) which was accompanied by right-lateral displacement of up to 0.75 m. The ratio of dip-slip to strike-slip varies from 1:1 in the NE to 2:1 in the SW. Nicol et al. (2018) have proposed that the Conway-Charwell Fault merges with the Hope Fault in the upper crust and can be considered part of the Hope Fault zone.

Hope Fault

The Hope Fault passes within a kilometre of the Northern SJF and strikes at 068°. The fault accommodates mainly right-lateral strike-slip with a component of reverse slip which produced uplift of the ranges north of the fault. It is generally considered to be the southern boundary of the MFS and may have accommodated up to 70% of the 40 mm/yr plate motion proximal to the northern end of the SJF (K., 1992; Knuepfer; Langridge et al., 2003; McMorran, 1991; Van Dissen, 1989). Further east of the study area on the seaward segment of the Hope Fault displacement rates diminish to <5 mm/yr, as displacement is transferred northwards onto the Jordan Thrust, Kowhai Fault and Kekerengu fault (Van Dissen, 1989).

No clear displacements were recorded on the Hope Fault in the Charwell River area during the 2016 earthquake. However, the seaward segment of the fault accommodated slip and associated folding of geomorphic surfaces perhaps totalling 1-2 m of vertical displacement (Pettinga pers comm, 2018). The last of rupture of the Hope Fault in the study area was surprising to many researchers, given that it ruptures every ~140-330 years and has not accrued slip for at least 200 years (Langridge et al., 2003; Stirling et al., 2012).

1.4. Stratigraphy of study area

Stratigraphy in the study area comprises Mesozoic Torlesse basement unconformably overlain by Cretaceous-Cenozoic strata locally up to about 1 km thick (Crampton, 1988; Rattenbury et al., 2006). In the north of the study area, these units are unconformably overlain by Late Quaternary alluvial gravels and fan deposits. Torlesse Supergroup rocks mainly comprise interbedded greywacke and argillites of the Pahau Terrane (Rattenbury et al., 2006). Torlesse basement is the main rock unit in the study area and crops out on both sides of the fault for ~12 km along the Central and Southern sections of the fault.

In the NCD Cretaceous and Cenozoic strata are primarily preserved in synclines separated by basement which outcrops on anticlines. North of the Torlesse and SW of the Late Quaternary terraces Cretaceous and Cenozoic strata form a 2 km wide band in the Monkey Face area (Crampton, 1988). These stratigraphic units form a syncline that is fault bound to the north by the steeply dipping Charwell Fault (orientation $240/70^0$) (Figure 1.4) (M. Rattenbury, 2006; S. Crampton, 1988).

North of the SJF in limestone creek, and close to the syncline fold hinge, Early Eocene Amuri limestone outcrops (Fig. 1.4). The Amuri limestone is dominated by deep marine strata and was deposited throughout the eastern South Island. Early Eocene Waima Formation underlies the limestone and was deposited in a shallow marine setting. The Conway Formation, a Late Cretaceous (Santonian) marine sandstone, underlies the Waima Formation and overlies Mid-Late Cretaceous Gridiron Formation (Fig. 1.4). The Gridiron Formation includes the Bluff Sandstone Member with a minor conglomerate lithofacies at the base of the unit. The Bluff Sandstone lithofacies dominates in the Monkey face area. The Bluff sandstone member is a Late Cretaceous (Cenomanian) shallow marine to coastal deposit. The Gridiron Formation rest on Torlesse basement and this contact is displaced by the SJF in a left-lateral sense, consistent with the sense of displacement in the Kaikoura Earthquake (see sections 2.4 and 4.6.2. for further discussion).

Torlesse and Cretaceous-Cenozoic strata are overlain by alluvial gravels primarily deposited by the Charwell River. These deposits range in age up to ~170 ka with the youngest aggradation gravels formed beneath the Stone Jug surface and being deposited at ~13 ka. After the Stone Jug surface was abandoned at 13±2 ka, up to 75 m of degradation formed 11 resolvable terraces on the upper Charwell riverbanks. This is assumed to be currently

continuing at low rates of <1 m per kyrs. Degradation was initially gradual, then rapid, and gradual again, with 30m/kyrs of degradation at its peak between approximately 5ka and 6ka (Bull, 1991)

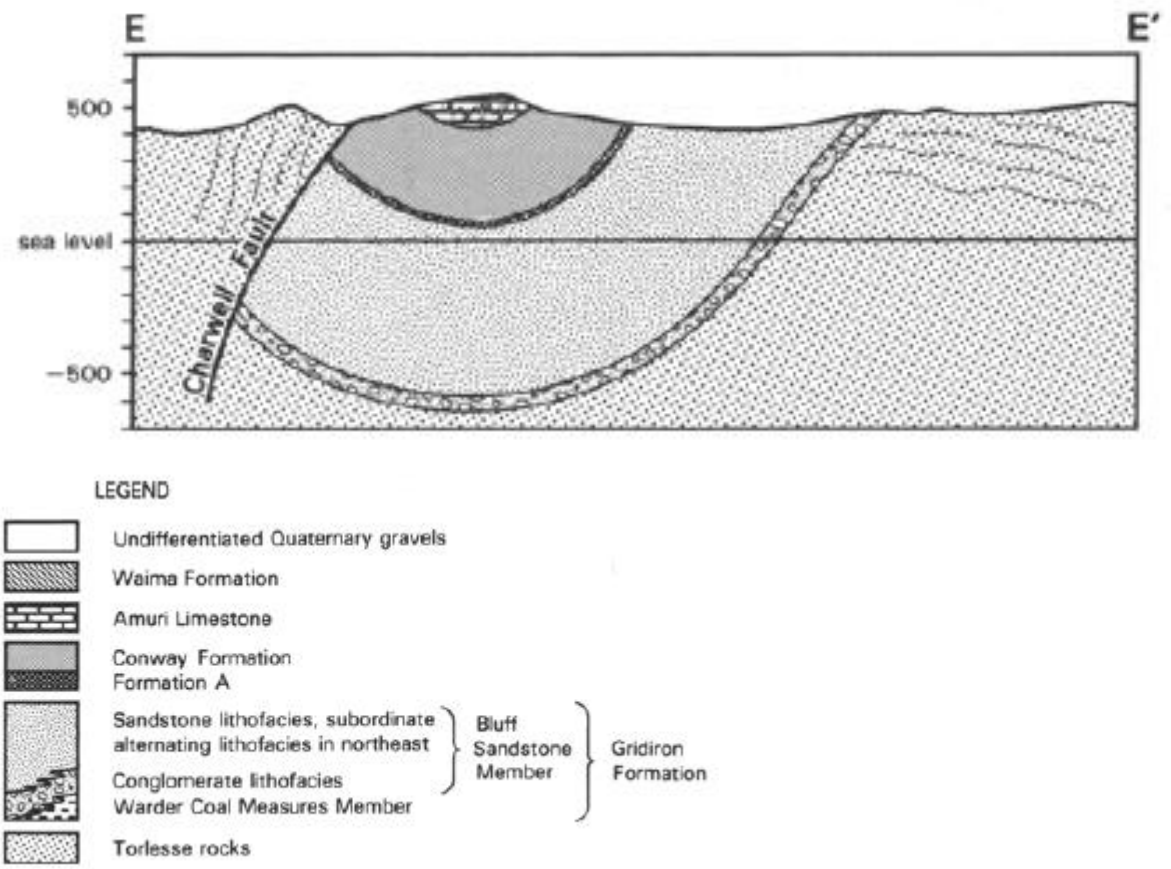

Figure 1.4: NW to SE cross section showing the structure and stratigraphy for Cretaceous-Cenozoic strata in the Monkey Face area near the SJF. Cross section starts (E) in the headwaters of Limestone Creek north of SJF (Crampton, 1988). See Fig. 3.1 for the location of the cross section.

1.5. Thesis outline

This thesis contains 5 chapters and 4 appendices. Of the remaining chapters, three focus on specific aspects of the investigation into the SJF and the final serves as a synthesis and conclusion chapter. In text references cited in each chapter are listed together at the end of the thesis.

Chapter 1

Chapter 1 presents a brief overview of the background of the study, why fault-specific studies along the SJF are valuable, and the wider context of plate boundary and North Canterbury tectonics.

Chapter 2

Chapter 2 uses remote sensing data and field work to characterise the geometry and kinematics of the 2016 rupture along the SJF. Detailed mapping with statistical analysis define in detail the geometry of the SJF. Its complexities are then discussed. Displacement magnitudes and directions are analysed to characterise the kinematics of the 2016 event. Using these learnings, the role of secondary faults and the possible interactions between the SJF and neighbouring faults is discussed.

Chapter 3

Chapter 3 investigates the idea that fault strike is controlled by pre-existing structural weaknesses in bedrock. It uses datasets presented in Chapter 2 together with datasets derived from remote sensing (e.g., DEM, Hillshades, LiDAR) to graphically, spatially and statistically analyse these data in an attempt to understand the relationship between the orientations of Torlesse bedding and faulting. It focuses on the extent to which structural weaknesses in basement influences fault orientation, but also considers other controls on fault strike.

Chapter 4

Chapter 4 is a paleoseismic study of the SJF. It is part of a wider multi-institutional effort to learn more about prehistoric earthquakes on faults that ruptured in the 2016 Kaikōura event. Members of the University of Canterbury, GNS and Lincoln University completed two rounds of trenching in consecutive summers to inform the history of faults in the North Canterbury domain. The two SJF trenches were excavated and logged by a team of University of Canterbury researches including Andy Nicol, Jarg Pettinga, Kate Pedley, Dale Cusack, Rinze

Schuurmans and myself. Chapter 4 used Optically Stimulated Luminescence (OSL) and radiocarbon dating to constrain the timing of mainly Holocene paleoearthquakes on the SJF.

Chapter 5

Chapter 5 serves as a discussion and synthesis of all ideas arising from individual chapters. It presents conclusions drawn from individual chapters before outlining potential future work.

Appendices

Appendix 1 is a series of field photographs to aid the understanding of field methodology and its limitations discussed in this chapter. It also includes a range of photos of the SJF to help relate how different structures, rupture geometries and displacements appear in the field. Appendix 2 contains all raw data collected in the field including discrete offsets, feature measured, date, sense of displacement, strike and surface geometry. Appendix 3 and 4 are lab reports for all OSL and ^{14}C radiocarbon dating samples.

The text and figures have been prepared as a thesis and not as a series of manuscripts, although it is hoped that components of the work may form part of a future publication. In particular, chapter 4 might form the basis of paper outlining the paleoseismic history of the SJF.

Chapter Two: Geometry and Kinematics of Fault Rupture

2.1. Introduction

The Stone Jug fault (SJF) surface rupture connects the Conway-Charwell and Hundalee faults (Fig. 1.3). The first-order geometry and kinematics of the SJF surface rupture are presented in Nicol et al. (2018), following preliminary post-earthquake investigations primarily using remote sensing data. This chapter utilises new field data, together with existing LiDAR, aerial photography and field observations (Litchfield et al., 2018; Nicol et al., 2018; Williams et al., 2018), to study the detailed geometry and kinematics (slip directions and magnitudes) of the 2016 SJF surface rupture. The chapter presents a range of maps and analyses to define the geometry and kinematics of the fault. These data and analysis have been used to examine how the SJF interacted with nearby faults in the Kaikōura Earthquake and its regional role for accommodating deformation in the North Canterbury (tectonic) Domain (NCD).

Preliminary investigations indicate that the SJF has an average strike of NNW (335°), dips steeply (85° E) and extends for ~19 km south of the Hope Fault in the NCD (Litchfield et al., 2018; Nicol et al., 2018; this study). During the 2016 Kaikōura Earthquake, the fault accommodated mainly left-lateral and vertical slip, with the upthrown side of the fault changing along strike (Fig. 2.5). Prior to the 2016 earthquake, a pre-existing fault scarp was mapped along the northern 5 km of the SJF where it crosses Late Quaternary alluvial terraces and fan surfaces 11-14 kyr in age (Bull, 1991; Rattenbury et al., 2006; this study – Chapter 4). The remaining ~12 km of the fault is primarily contained within Torlesse Supergroup basement and is not represented on pre-earthquake geological maps (see Rattenbury et al., 2006). For the purposes of this thesis, the 2016 SJF rupture is divided into three sections based on fault trace geometry and kinematics. The Northern section is ~5 km long, strikes NW and is marked by a fault scarp up to 5 m high and down to the NE. The Central section is ~8 km long, strikes north to NNW and was upthrown to the east. The Southern section is ~6 km long, strikes north and was upthrown to the west then to the east and is characterised by less continuous traces (than the more northerly sections of the fault) contained within a widening fault zone that bends in strike WNW. More detailed descriptions of the geometries and kinematics of these sections of the fault are presented in this chapter.

2.2. Methods

2.2.1. Fault surface mapping and displacements

This project commenced in June 2018 approximately 18 months after the Kaikōura event. Due to the remote nature of much of the field area many surface traces and strain markers (e.g., fences and tracks) had not been modified post-earthquake. Prior to this thesis University of Canterbury researchers conducted preliminary field measurements in select areas at the northern end of SJF near the highway as a part of the initial scientific earthquake response in the months following the earthquake (Nicol et al, 2018). These initial investigations provided two clusters of displacement measurements and GPS locations of some fault traces. An important goal of this thesis was to undertake end-to-end field mapping of the fault trace in a systematic manner; this goal was achieved.

Prior to the start of fieldwork, a desktop study was conducted using pre-existing field mapping, aerial photographs, LiDAR and satellite imagery to identify surface ruptures that could be visited in the field. Remote sensing data were used to study the rupture surface trace and create a shapefile of the SJF in ArcMap. From this shapefile GPS waypoints were created to aid in navigation to key field sites. InSAR and aerial photographs were analysed to find potentially unidentified fault traces that were investigated on LiDAR and in the field. LiDAR data was sourced from: GNS Science; New Zealand Transport Authority (NZTA); Land Information New Zealand (LINZ); Environment Canterbury (ECan), and AAM NZ Ltd.

During an Initial phase of fieldwork, where possible, all faults identified on LiDAR were visited. Forestry operations, and dangerously steep mountains or valleys meant some secondary fault traces were not accessible and have not been studied in the field. Through conversations with farmers and by chance new faults not seen on LiDAR were also added to the dataset. Where the surface expression was clear or LiDAR resolution was poor, the fault trace was manually mapped with a handheld GPS Trimble Geo7X at a 3D accuracy of consistently less than ±0.15 m post-processing. GPS points were also created where measurements and observations were made.

Fault trace maps were generated in ArcMap 10.2.1 using a wide variety of derived datasets. To easily generate a range of fault trace maps, all field data were georeferenced to the

corresponding polyline in shapefile of the SJF surface traces. This allowed for quick spatial analysis of different characteristics of each trace using Excel pivot tables and Arc GIS. Prior to fieldwork many secondary faults and gravity-driven scarps were identified from LiDAR. Gravitational faults and landslides were identified but mapped in a separate shapefile and not entered into the field measurement database. After fieldwork secondary faults were categorised firstly by their conformity to a linear or continuous trace, but also by their orientation, surface displacement and continuity in rupture style to neighbouring traces.

Where possible vertical and horizontal displacement measurements, surface-trace geometry, upthrown side, quality of data, features measured and any notes on the area were recorded at each field site. Displacements were measured across 9 linear cultural strain markers, such as fences and road edges. Less conventional markers, such as tree roots and animal tracks, were used to quantify slip. The reliability and uncertainty of these measurements are variable. Therefore, the strain marker and estimated error were recorded alongside all slip measurements. A total of 51 displacement measurements (vertical and/or lateral displacement) were recorded in the field and are presented in Appendix 2. Tabulation of the displacements allowed for georeferencing to polylines in ArcMap and quick statistical analysis of different parameters of each trace using Excel pivot tables and formula.

2.2.2. Near-surface fault strike and dip

For individual fault traces, true strike and dip were calculated using basic geological and geometric principles. To calculate strikes and dips for the SJF, I used the fault-trace shapefile, spot heights from the DEM (digital elevation model, derived from LiDAR) and orientation of and length of traces calculated with the Arc GIS toolbox.

Where possible, two methods of calculating fault dip from topography were used and the results averaged to create a more robust result. Stereographic and trigonometric techniques were employed in conjunction with the geometry and altitude of the mapped fault trace to estimate the strike and dip. In the stereographic method different apparent strikes and dips from proximal, but significantly different, parts of the fault trace were plotted on a stereonet to estimate the true strike and dip of the fault plane. As this method required a significant change in apparent strike to be accurate, it was typically applied across ridges, gully's and along the edges of valley floors. It, therefore, was not applicable in the Northern SJF or where the SJF consistently occupied one limb of a ridge. This method had the widest application and

was the most accurate of the two methods, producing strike and dip estimated errors of ±5° when used at a suitable site. The accuracy was due in part to being able to source data from two traces and using accurate processing to minimise error.

The trigonometry method (Fig. 2.1) uses a three-point problem strategy to estimate the strike and tip. It uses trigonometric functions to find fault dip by connecting two points on the fault surface expression, at the same elevation, either side of the valley or ridge. The distance from this imaginary line to a third point on the surface expression, along with the corresponding elevation change, provides information to calculate the dip of the fault plane. These measurements were taken from the LiDAR and the DEM in Arc GIS. This method was used in fewer circumstances than the stereonet method as it required a ridge or valley where the fault trace passed through the same elevation either side of the feature so that a surface could be projected. The trigonometric method had the advantage of being able to calculate two measurements, one on each side of a topographic feature, and averaging them. However, it contained more processing steps and more data points which lead to fractionally greater errors estimated at ±10° for strike and ±20° for dip. In most situations, the difference in Strike and dip between both methods was less than 5°. The larger errors for the trigonometric method reflects human error associated with the additional manual steps of creating the projected fault surface. The trigonometric method was particularly inaccurate for steeply dipping faults as the lateral distance between the projected fault plane and the surface fault trace was very small leading to high percentage errors. This made site selection key for maintaining high-quality data.

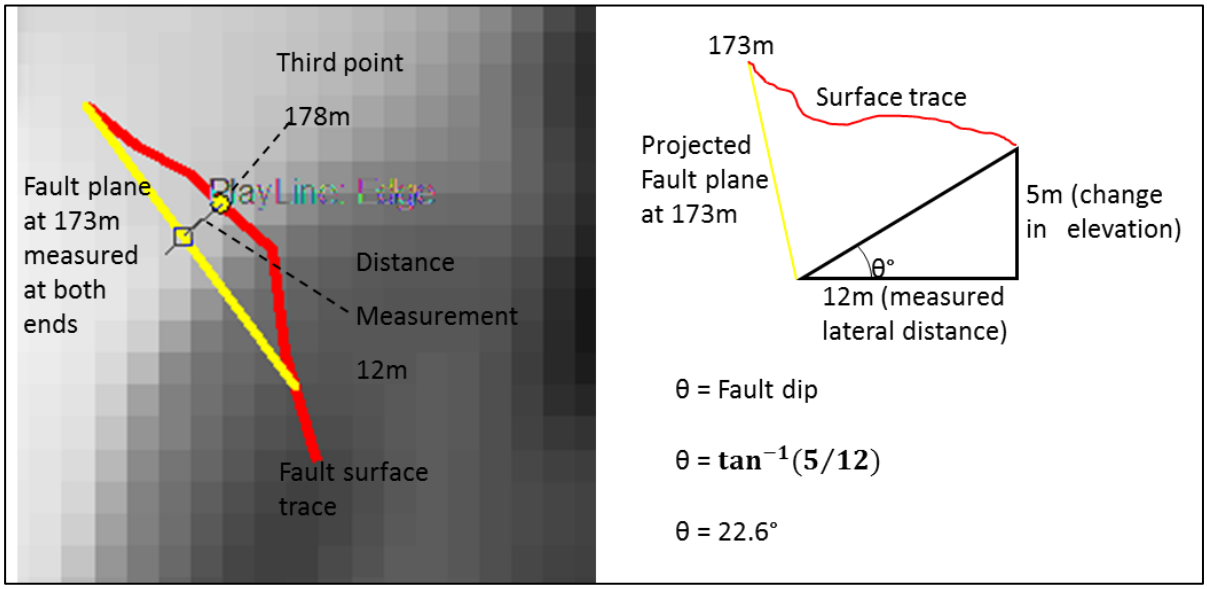

Figure 2.1: Diagram illustrating the trigonometric fault strike and dip calculation method. Fault surface trace is red and yellow line is an isotopic line on the projected fault plane. The background is a hillshade derived from LiDAR.

2.2.3 Geomorphic and 3D photogrammetry maps

In addition to the analysis described above a geomorphic map of the northern terraces was created to search for displaced landforms and other potentially unmapped faults that ruptured in 2016. Terraces were mapped with the aid of an algorithm that identified terraces by changes in elevation of surrounding pixels. This map provided points of interest that could then be investigated in the field and other datasets.

During this study Jesse Kearse at the University of Canterbury derived a 3D photogrammetry dataset from of the NCD. 3D photogrammetry matches pre and post-quake aerial photography to create a detailed point cloud of 3D vectors of total displacements. (Howell et al, 2018). It displays regional movement in three planes and covers the Central and Northern SJF sections providing information on net distributed displacement. Analysis of this dataset constrained displacements across faults and was particularly important for quantifying fault displacements on remote traces that could not be visited in the field. Estimates of displacement at these sites helped to fill gaps in field data. Additionally, total regional deformation could be compared to discrete displacement seen in the field. This helped to determine how much displacement was accommodated by distributed deformation away from the primary slip surface. In addition, contours of east-west, north-south and vertical displacements helped constrain the deformation of the blocks between faults. In this

study, these models provided data on how the SJF kinematically interacted with neighbouring faults and the impact of the multi-fault rupture on the landscape.

2.3. Fault geometry

2.3.1. Overview

Detailed mapping of the SJF shows that the primary surface trace is approximately 19 km long (Fig. 2.2). This is slightly longer than the 17 km previously indicated (Litchfield et al., 2018; Nicol et al., 2018) due to the discovery of new traces at the southern end of the fault. The exact length of the SJF is difficult to determine as both ends of the 2016 rupture exhibited low surface displacements (e.g., <0.4±0.1 m) and, in the case of the Southern section, are accommodated on multiple fault traces (Fig. 2.3). To add to these issues, the trace data at both ends of the fault were poorly resolved. This was either due to surface reworking of the trace by farmers by the time of fieldwork (northern end) or because of poor LiDAR coverage compounded and/or due to a lack of land accessibility (Southern Section).

Mapping and field measurements identified 62 fault traces along the SJF in addition to a number of scarps interpreted to have been formed by gravity processes, which were not mapped here. Tectonic fault ruptures have been differentiated into primary traces and secondary traces figure 2.4 The majority of analysis in this chapter focuses on the SJF primary traces. These traces were mainly generated entirely during the Kaikōura Earthquake, although an active fault scarp up to 5 m high was previously mapped northwest of the Charwell River (Rattenbury et al., 2006; Barrell and Townsend, 2012). In addition, five secondary fault traces displayed fault scarps of mostly <2 m prior to 2016.

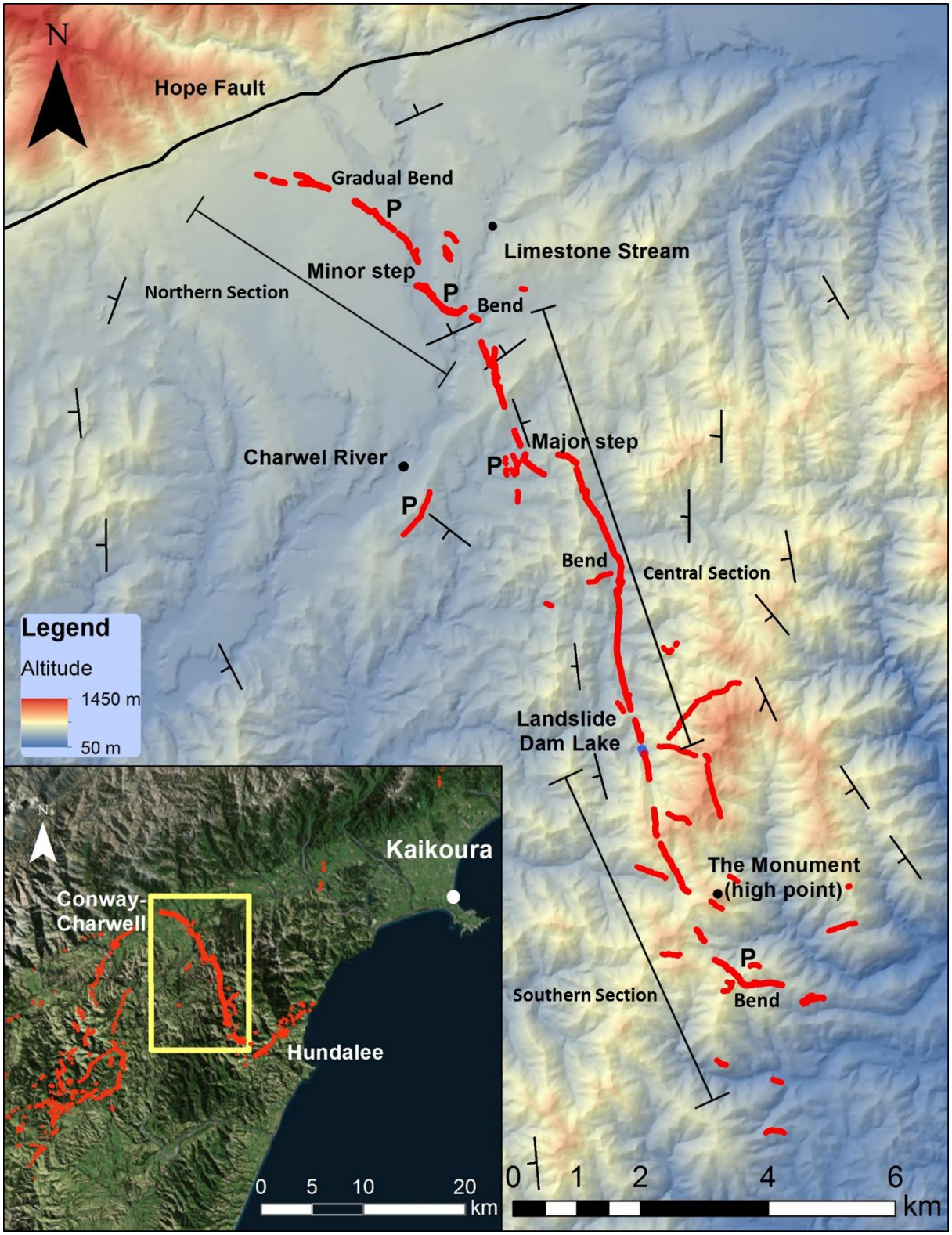

Fig 2.2: The main map shows the locations and geometries of Stone Jug Fault traces (after the 2016 Kaikōura Earthquake), presented on a DEM of the study area. Fault traces that ruptured pre-existing fault scarps are labelled "p". Northern, Central and Southern Sections of the fault are indicated. Inset map shows the location of the study area (yellow rectangle) and SJF. Inset regional map is the Esri World imagery (2017).

2.3.2. Primary fault trace

The SJF primary trace has an approximately sigmoidal shape. The trace has a Central Section about 8 km long that has an average trend of approximately 160°. At the north and south ends the SJF it swings in strike to the NW (290-300°), bending by approximately 40-50° towards the strike of the Hundalee and Conway-Charwell faults. These strike changes are comparable to changes in strike of Torlesse basement bedding (for further discussion see Chapter 3). For the purposes of this thesis, the fault has been divided into three sections (Fig. 2.2) the geometries of which are described below.

The Northern Section is approximately 5 km long and entirely on river terraces NW of limestone creek. The northern tip of 2016 ruptures was not mapped to reach the Hope Fault, although I concur with the mapping of Rattenbury et al. (2006) in suggesting that this is likely. The primary trace along this section of the fault generally strikes NW and is continuous, with few secondary fault traces. In detail, the trace comprises a ~400 m wide right step across the Charwell Riverbed and an east-west trending graben west of the Charwell River. The Graben is 30 m wide and 250 m long, comprising a main north-dipping normal fault to the south with a minor antithetic pair to the north. The fault bounding the southern margin of the graben has been trenched as part of this thesis and further details of the graben geometry, kinematics and earthquake history are presented in Chapter 4 (see Fig. 4.1 in Chapter 4 for graben map). At an individual trace scale en echelon and left stepping surface geometry is common (see Appendix 1)

The Central Section of the primary fault trace from 2016 is 8 km long, generally strikes 160-180° and is mostly continuous. In detail from north to south this section of the fault comprises a ~500 m wide left step in the trace and right bend which produces ~160° and 170° parts of the trace (Fig. 2.2). The left step coincides with a major topographic ridge and is associated with a cluster of secondary faults which accommodate distributed deformation around the step. South of this step the right bend in the fault follows an important valley, suggesting that this valley may have partly formed by erosion of weak rock along the fault zone. This interpretation is consistent with the fault positioned directly in the river in the south of the valley before the river meanders. At least 10 small (<50 m long) secondary faults are present in this valley system but are too small to be displayed on the map presented in Fig. 2.2. The north of this section displays considerable branching and parallel traces with block rotation a

barrier to accurate scarp height measurements. South of the left step en echelon and frequently stepping surface traces are typically observed (Photographs in Appendix 1).

The Southern Section of the SJF is approximately 6 km long and comprises a discontinuous primary trace associated with 1-3 km wide zone of secondary low displacement and disconnected traces. The discontinuous form of the primary trace appears to be related to the locations of scree slopes (across which the trace could not be mapped) and topographic ridges. This section of the fault crosses the most mountainous terrane of the field area and where the fault crosses ridges it often steps and becomes discontinuous. In some cases, the trace cannot be mapped across steep slopes where gravitational scarps formed due to slope failure during the 2016 earthquake may mask the primary tectonic fault. The primary fault along this section of the trace also comprises three minor left bends which, from north to south, change the fault trace trend from 170° to 155° to 140° to 90°. These bends rotate the SJF trace into sub-parallelism with the Hundalee Fault. As with the northern end of the fault, the southern limit of the mapped traces from 2016 stops several kilometres short of the Hundalee Fault. However, faulting at the southern end of the fault is distributed and difficult to trace. I believe that the SJF and Hundalee Fault likely intersect. This is an idea that is supported by the southern termination of the Hundalee Fault at about the location where with intersection might occur (Fig. 2.3).

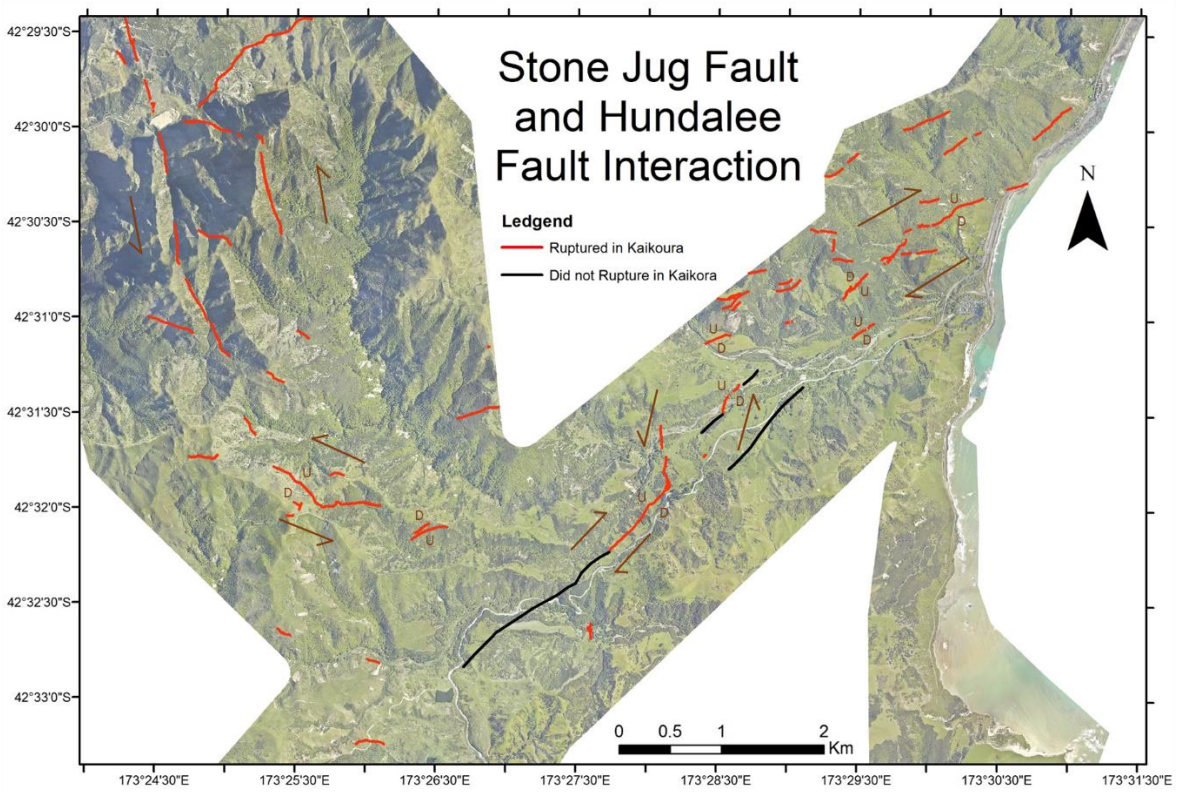

Figure 2.3: Kaikōura surface rupture of the Southern SJF and Hundalee Fault. Fault trace shapefiles are adaptations of original LiDAR interpretations by Narges Khajavi of the University of Canterbury. Hundalee Fault kinematics are from Williams et al. (2018).

2.3.2. Secondary fault traces

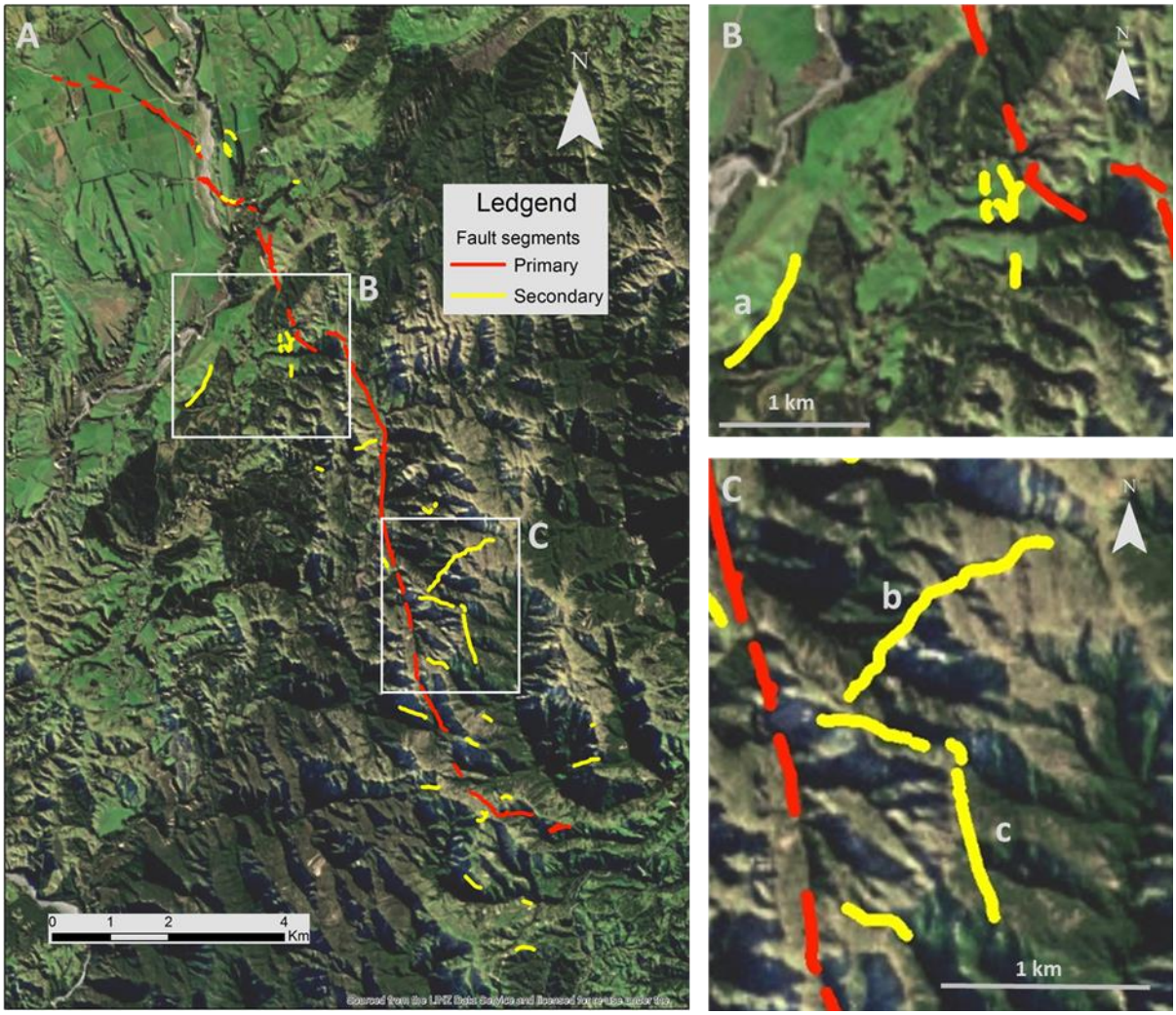

Figure 2.4: Map showing 2016 ruptures plotted on a colour orthophotograph. Red lines indicate primary traces and yellow lines secondary traces. B shows a significant western fault and cluster of small offsets faults discussed in section 2.4 and 2.5. C shows large offset continuous eastern secondary faults these are also discussed in section 2.4 and 2.5.

48 secondary fault traces have been mapped within 2 km of the SJF primary trace (Fig. 2.4). The majority of secondary fault traces appear to be both randomly orientated and distributed, although some of these secondary traces are clustered close (e.g., <300 m) to steps or bends in the primary trace. Space and time restrictions do not permit detailed descriptions of all secondary faults and here I will discuss three of the larger and more important secondary faults. The 0.8 km long fault trace was mapped west of the primary fault and strikes NE parallel to the Charwell River (labelled 'a' in figure 2.4B). This fault strikes approximately perpendicular to the primary fault trace and accommodated an average of ~25 cm vertical and ~6 cm horizontal displacement along the trace. Despite these small 2016 displacements, this

secondary fault is notable because it occurred along a pre-2016 fault scarp up to 6 m high which is upslope facing and produced ponds and swamps prior to the Kaikōura event. Two additional secondary faults are shown in figure 2.4C, where they are labelled 'b' and 'c', and again strike at a high angle to the primary fault trace. Two field measurements and differential 3D photogrammetry indicate that these secondary faults have vertical and right-lateral displacements of up to 1 m, which are a similar magnitude to the nearby SJF. In particular, the northernmost of these faults accommodate an estimated 0.6±0.3 m down to the north, with vertical displacement on the primary SJF trace decreasing by a similar magnitude southward across the intersection between this secondary fault (see section 2.4.3 for further discussion).

2.3.3. Fault strikes and dips

The average near-surface strike and dip calculated from SJF traces is 173° / 55°. This strike departs from the ~160° average value that can be inferred from fault maps. This difference is attributed to a small sample size (N=8) and a sampling bias towards the south SJF and shallow dipping faults where changes in strike are most clearly observed. Calculated near surface dips are most often about 50°, however, dips of 15° to 72° were measured. Apparent and true dips were often very close, with the majority of differences between true and apparent dip less than 15°. Fault strikes are locally sub-parallel to Torlesse basement bedding, which is considered in more detail in Chapter 3 and has been previously observed (Nicol et al., 2018). Torlesse bedding dips, which typically range from 45-80° adjacent to the fault (Fig. 31) and are comparable to calculated fault dips.

2.4. Kinematics

2.4.1. Overview

Displacement magnitudes and slip components (i.e. vertical, horizontal and net slip) change between fault traces and along the same trace. Despite this variability, it is generally the case that vertical and horizontal displacements are comparable and the SJF accommodated oblique slip during the 2016 event. 51 vertical and horizontal displacement measurements produced net displacement for a single trace from 0.05±0.1 m to 1.4±0.1 m, with a median of ~0.4±0.1 m. All but two displacement measurements for the primary SJF traces are left-lateral, while the upthrown side of the fault varies along strike (Fig. 2.5).

Vertical, horizontal and net displacement profiles for the SJF are presented in Fig. 2.6. In this section, I provide a brief summary of displacements on each of the main segments. Vertical and horizontal displacements along the Northern Section of the fault are consistently ≤0.5 m (0.4±0.1 m). However, vertical displacement is up to 1 m (0.9±0.1 m) on the southern bounding fault of the graben, where the fault scarp is up to 5 m in height on the ~11 kyr terrace surface (for further information on this site see Chapter 4 and Fig. 4.1). The Northern Section consistently shows uplift to the southwest. The Central Section of the SJF accommodated up to 1.15 m (1.05±0.1 m) of left-lateral and 1 m (0.9±0.1 m) vertical displacement on the Central Section, with median displacements of 0.4±0.1 m (horizontal) and 0.3±0.1 m (vertical). The Central Section is consistently uplifted in the east. South of the maximum displacements, they decrease then gradually increase again until the next maximum near the southern end of the section. The Southern Section of the SJF is mainly upthrown to the east and displays displacements of 0.5±0.1 m to 1.0±0.1 m, but are typically lower than the Central Section with median horizontal and vertical displacements of 0.25±0.1 m and 0.4±0.1 m respectively. The decrease in southern activity is not well represented through statistics due to sampling bias. Low offset traces in the Southern Section were often not found in the forested and scree terrain. The northern 2 km of this section of the SJF, north of the Monument, is anomalous as it exhibits dextral faulting, uplift to the west and lower displacement than adjacent traces.

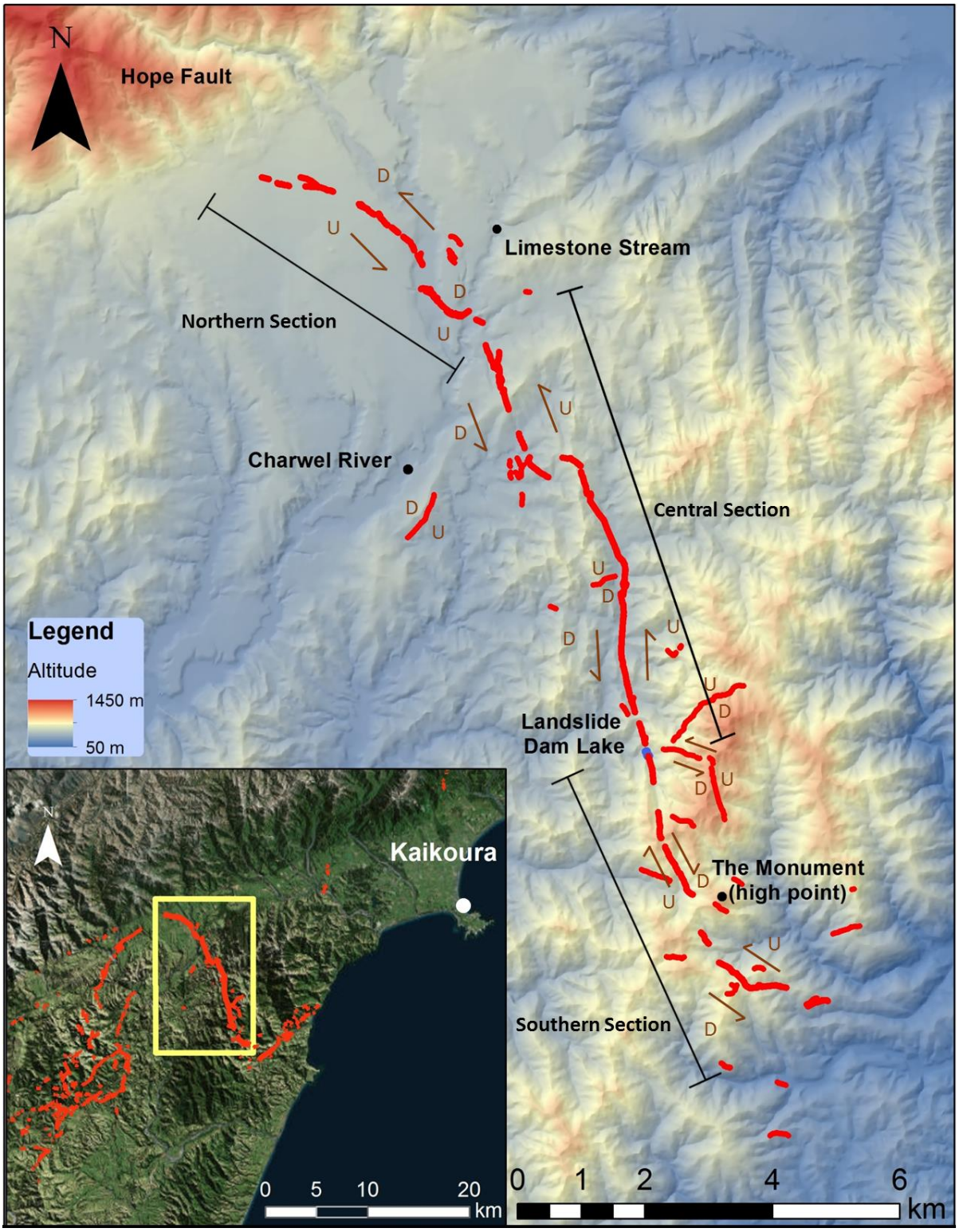

Figure 2.5: Main map shows the locations and geometries of Stone Jug Fault traces (after the 2016 Kaikōura Earthquake) mapped from surface ruptures, presented on a DEM of the study area. Diagrams shows the first-order kinematics of the SJF Kaikōura rupture. Arrows indicate directions of strike-slip displacement, while U and D indicate up and down throw directions. Inset regional map uses a Esri World Imagry (2017) basemap.

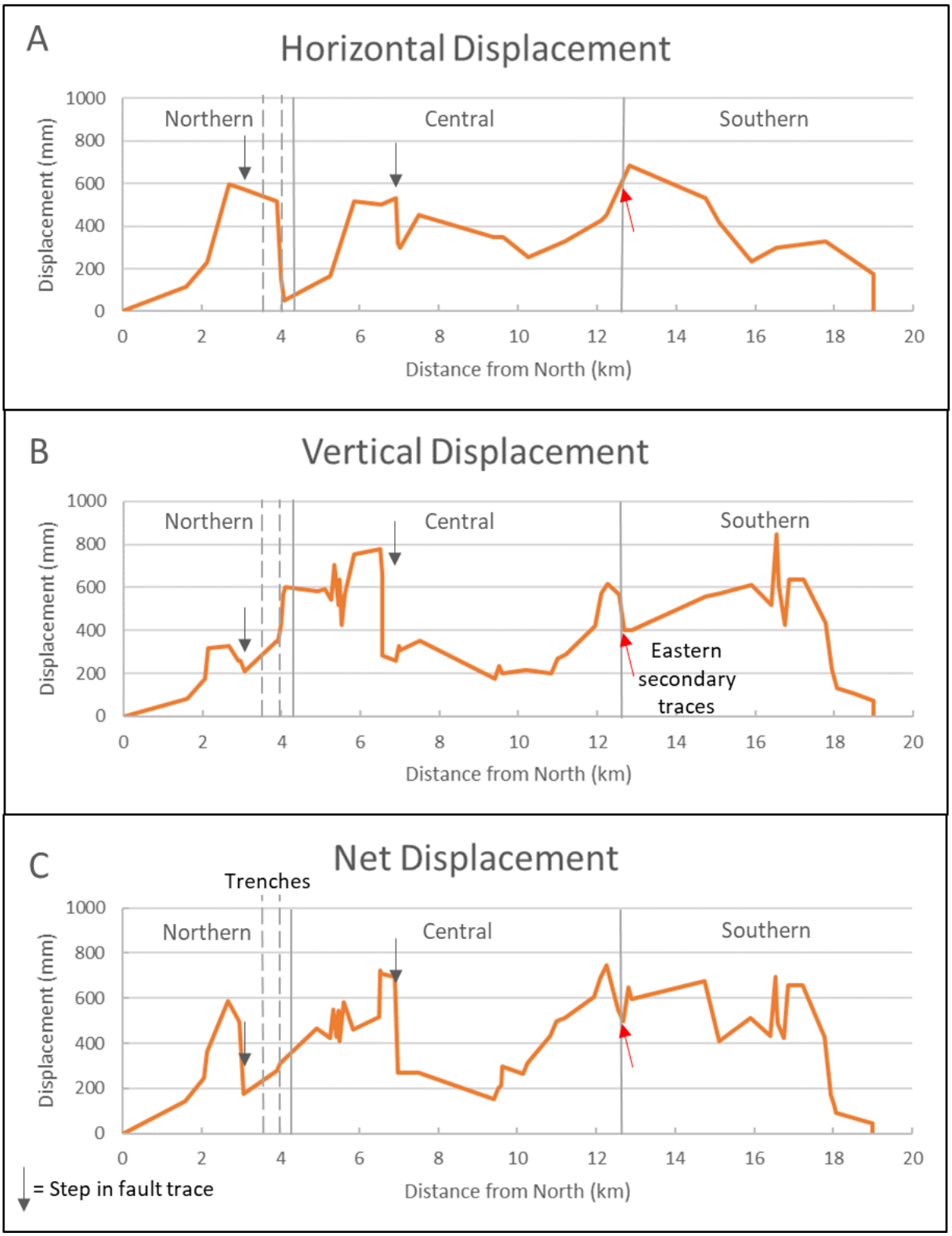

Figure 2.6: SJF displacement profiles for horizontal (A), vertical (B) and net (C) data. For the purposes of legibility, the orange line plotted is a three-point moving average. The horizontal displacement which has fewer data points (34 as opposed to 60 for vertical) and therefore lacks detail and may appear to have larger displacements than calculated net displacements in some data gaps such as at 3km. The black dashed lines show the approximate locations of trenches presented in Chapter 4 (see Figure 4.1)

2.4.2. Displacement profiles

The SJF is primarily an oblique slip left-lateral reverse fault (Fig. 2.5, Appendix 2). Vertical, horizontal and net displacement during the 2016 event have been measured along the length of the fault trace. left-lateral displacement, vertical displacement and net displacement reach values up to 1.1±0.2 m, 0.95±0.2 m and 1.4±0.2 m however the moving point average in Figure 2.6 makes these extremes appear smaller. Horizontal and vertical displacement measurements vary along the fault. These variations are observed for both the differential photogrammetry and field (tape) measurements. Neither the method of measurement nor associated uncertainties can account for the fluctuations in displacement. In some cases, displacement lows coincide with steps or branch-points along the fault trace indicating that some of the fluctuations in displacement may reflect fault segmentation (see Fig. 2.6). A potential explanation for the coincidence of displacement lows and steps in the trace is that these are sites of elevated off-fault deformation, which is generally not well sampled by our displacement measurements. This is true for the low at 5km which had multiple parallel traces, which were difficult to collectively sample. At these steps (or bends) in the fault trace, I would also expect along-fault decreases in the magnitude of horizontal displacement to coincide with increases in vertical displacement. For example, in the graben trenched and reported in Chapter 4, the strike-slip displacement decreases to zero (or to a value that is sub-resolution) and the vertical displacement increases to a maximum of 0.9±0.1 m (Fig. 4.1, Chapter 4). These changes can be directly related to fault strike, with more strike-slip observed on N-S sections of the fault and dip-slip dominating in the E-W trending graben. Therefore, extension in the graben is comparable to what would be observed in a pull-apart basin on a strike-slip fault.

In addition to the short wavelength fluctuations in displacement, the moving average profile in Fig. 2.6 best shows variations in displacement along the length of the SJF. Displacement profiles for horizontal, vertical and net slip all show rapid increases from zero at the tips. Horizontal displacements are less variable due to fewer samples. Horizontal displacements peak at distances of 3 and 13 km along strike both of which were on traces that rotated more N-S than neighbouring traces. By contrast, vertical displacement is characterised by two strong maxima at distances of ~6 and 16 km, separated by a low at 7-11 km distance. While the location of the low is approximately consistent for both horizontal and vertical displacements, the highs for each component of displacement are not. This minor variation in maximum displacements is due to local trace orientations and geometry's favouring dip-slip

of strike-slip as discussed previously. At this time the geological explanation for the regional variations in displacement along the primary fault trace of the SJF are not clear, although it seems unlikely that these changes can be simply related to fault strike. One possibility is that lows in displacement on the primary fault trace occur where the off-fault secondary faulting is greatest. For example, near the southern end of the fault the high displacement gradients on the main trace may be accommodated by an increased in displacement across a 3 km wide zone secondary faults. This zone of distributed deformation may facilitate the transfer of displacement between the SJF and the Hundalee Fault.

2.4.3. Fault orientations influence on the direction of lateral motion

The majority of SJF traces strike between NW(SE) and N(S) and are left-lateral. However, it should be noted that some traces within the SJF zone appear to have accommodated dextral strike slip. Figure 2.7 makes no distinction between primary SJF and secondary traces, although the majority of dextral traces are secondary. Only to primary traces of the SJF accommodated dextral displacement.

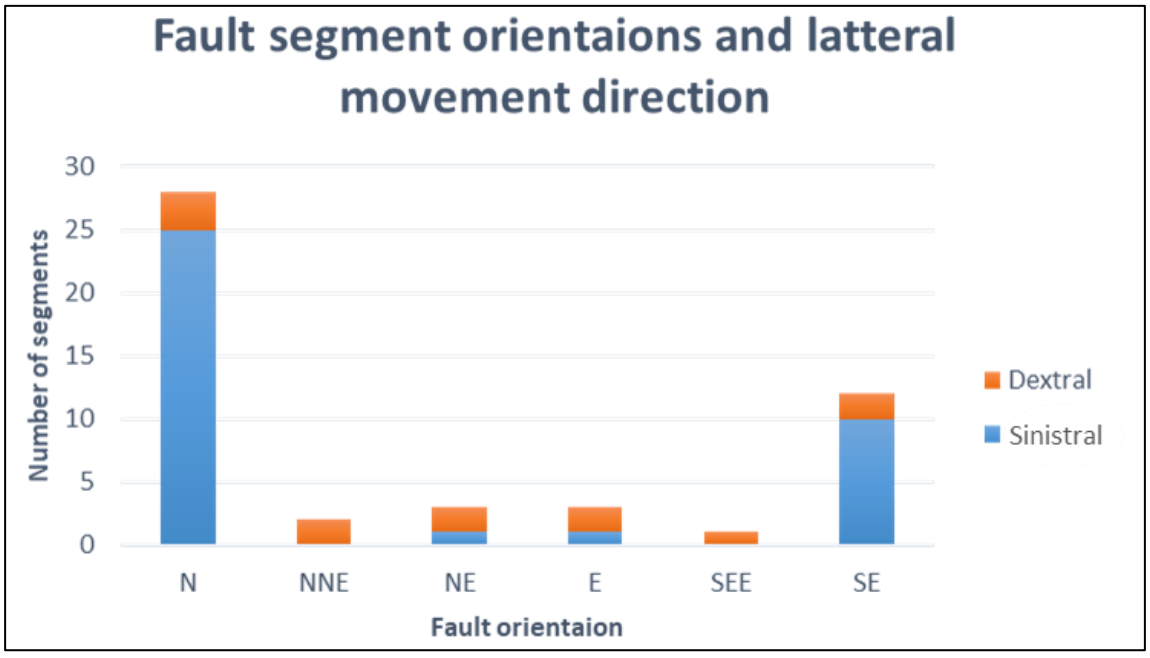

Figure 2.7: Histogram showing the relationship between fault strike and lateral slip sense for fault traces and displacements on the SJF generated during the Kaikōura Earthquake. Data from field observations and is skewed towards discontinuous traces which provide many of the trace counts in the graph and yet contribute a relatively small proportion (~15%) of the total trace length.

Secondary faults with NE to SE trends seem to favour dextral displacement. Dextral faults of this trend are consistent with the regional principal horizontal shortening (PHS) direction and have been observed on many of the ruptures south of the Hope Fault (Nicol et al., 2018). However, five secondary faults do not conform to the northern trending left-lateral fault and eastern trending dextral fault model proposed by Nicol et al. (2018). These departures in fault kinematics from the regional model require local changes in the PHS direction from the regional pattern. Gravitational overprint of the stress field on steep slopes and in mountainous areas could be one factor that locally changes fault kinematics. Further investigations are required to understand better why these local changes in fault kinematics occur.

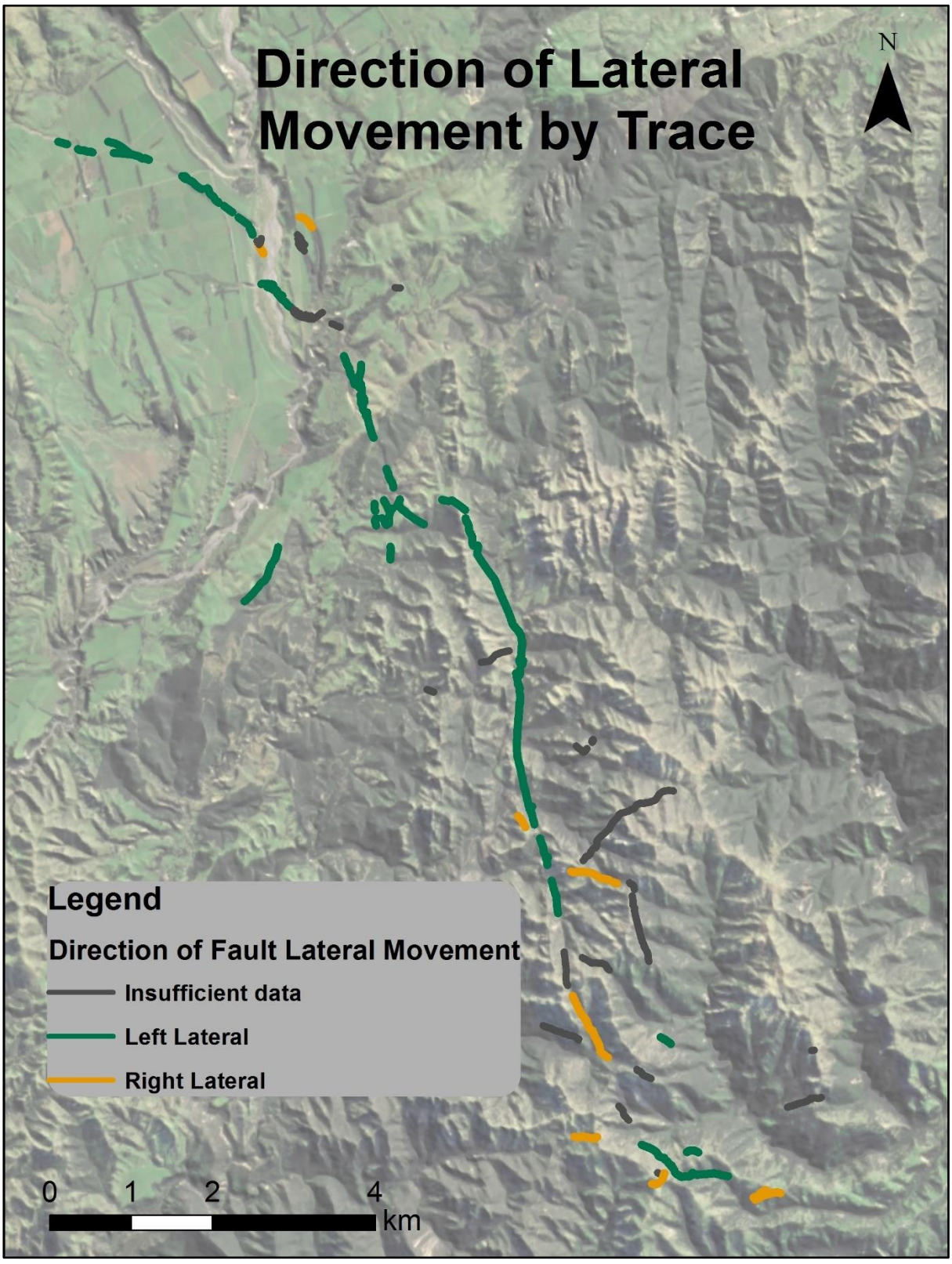

Figure 2.8: Fault map showing lateral movement sense for traces of the SJF during the Kaikōura earthquake. Basemap is a colour ortho-photograph which shows topography overlain by a hillshade.

2.4.4. Right-lateral displacement of primary trace

The majority (82%) of horizontal displacements on the primary trace of the SJF and over half (58%) of secondary traces are left-lateral. However, at two locations on the SJF dextral displacement has been recorded. Here I discuss these two sites and the possible explanations for their sense of slip. The northern-most site is on the west bank of the Charwell River where the surface trace displays a small (<100m trace) right-lateral displacement of 0.3±0.1 m and an even smaller vertical displacement <0.1 m. This trace strikes almost due north and at ~40° clockwise to the general strike of the fault in this area. I speculate that in this cast the dextral displacement occurs on a fault trace that is conjugate to the primary trace that is obscured or did not rupture the ground surface. Right-lateral displacements were also observed on the primary trace between the monument and the top of the Southern Section (Fig 2.2). While this trace has a vertical displacement of 0.55±0.1 m, on average, the right-lateral displacement measured from displaced (and severed) tree roots is 0.2±0.1 m. It was also uplift to the west rather than east like its neighbouring traces. This anomalous trace is bound by two sets of secondary faults with significant offsets to the east. These secondary faults have been interpreted to facilitate the anonymous movement sense of this isolated trace and are discussed in section 2.4.5.

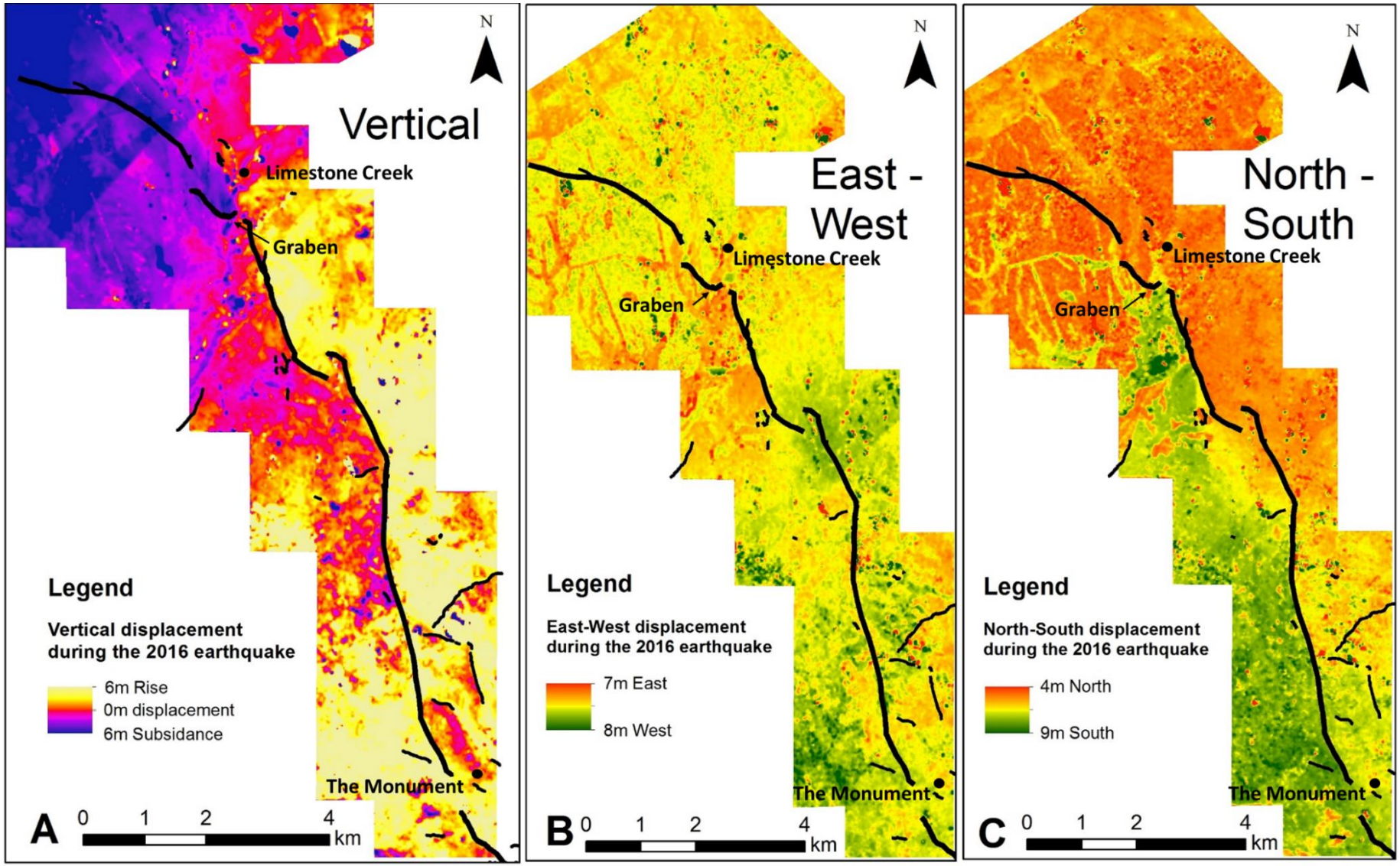

Figure 2.9: Displacements along the SJF derived from 3D differential photogrammetry. Displacements comprise three components; vertical (A), East-West (B) and North-South (C). Displacements from photogrammetry include on-fault slip and off-fault distributed deformation which can be differentiated using these data. Thick black lines are the primary fault trace, thin black lines secondary traces.

2.4.5. On-fault and off-fault displacement

Differential 3D photogrammetry helps constrain displacements and location of the primary trace of the SJF at a regional scale (Fig.2.9). The photogrammetry data was particularly useful in areas where the fault was poor surface exposed or data was scare due to limited accessibility. The photogrammetry data allows the relative importance of on-fault slip (discrete) and off-fault deformation (distributed) to be assessed. Here I use this data to determine the ratio of discrete and distributed deformation for different locations along the primary trace. A compilation of these ratios for both vertical and horizontal displacements suggests that they vary along the SJF. From the available 3D photogrammetry data about 10% to 80% of total deformation on the SJF is discrete and confined to the primary fault trace. Discrete deformation is typically <50% and often higher traces with for low total displacements.

The SJF accommodated differential uplift, however, in some areas absolute uplift was observed on both sides of the fault during the earthquake (Fig. 2.10 A). Regional uplift as observed on 3d photogrammetry gradually increases southward and averages ~5 m either side of the Southern SJF. This regional uplift is inferred to reflect slip on the Hundalee Fault, a hypothesis that is consistent with the up-to-the NW vertical displacement observed on the Hundalee Fault at the ground surface (Stirling et al., 2017; Williams et al., 2018). Previous studies have observed a range of 0.5 – 2.25 m discrete deformation on the Hundalee with an average of approximately 0.9 m (Williams et al., 2018). If distributed to discrete deformation ratios on the Hundalee are consistent with the SJF a 5m net regional displacement is consistent with these observations. Displacements are always lower than the observed regional uplift in the hangingwall of the fault and it is also possible that a component of this regional uplift reflects folding at the ground surface associated with slip at depth.

East-West movement near, or on, the SJF is typically low (<0.5 m) and cannot be resolved on Figure 2.9 B. By contrast, north-south movement in figure 2.9 C shows a clear and expected left-lateral fault motion with the western fault block moving south and the eastern block moving north. Along the Northern segment of the SJF left-lateral displacement in figure 2.9 C <20cm and left-lateral displacements observed in the field on the primary slip surface are likely close to the total left-lateral displacement (i.e. there is little off-fault left-lateral movement). Along the Southern Section of the SJF, both the east and west sides of the fault

moved south during the earthquake. This southward motion was as much as 0.5 m on the east side and 3 m on the west side of the fault and caused a maximum of approximately 2.5 m distributed left-lateral displacement directly north of the monument (Fig. 2.9C). By contrast, only 0.2±0.1 m of discrete lateral displacement was observed here on the primary fault trace. In addition, close to the primary trace along the Southern segment, two secondary faults east of the SJF perturb the uplift contours (Figs 2.10).

Figure 2.9 C also highlights a left-lateral displacement gradient which runs south from the sharp left bend across the Limestone Stream. This high displacement gradient suggests that for up to 3 km (8-11 km from the northern tip of the fault) along the fault the majority of horizontal motion in 2016 was accommodated on a blind fault which did not break the ground surface. It is possible the presence of a blind fault could partially account for a left-lateral displacement low observed in Figure 2.6 A around 10 km. That is, at this distance the displacement is low on the primary fault because some of the displacement is accommodated by a blind structure that was not included in the displacement profile (because it was not observed during field mapping).

Figure 2.10 shows the impact on regional displacement of the set of three continuous secondary faults to the east of the SJF. These structures all show downthrow to the south and east which is interpreted to facilitate the anomalous sense of displacement observed on the enclosed SJF trace. It is hypothesised these fault act to transfer stress to the nearby Oaro river fault which lies ~4 km east of them. This results in the decreased lateral displacement observed south of these structures. Unfortunately, there is no remote sensing data covering the Oaro River fault to study this hypothesis in detail within the scope of this thesis.

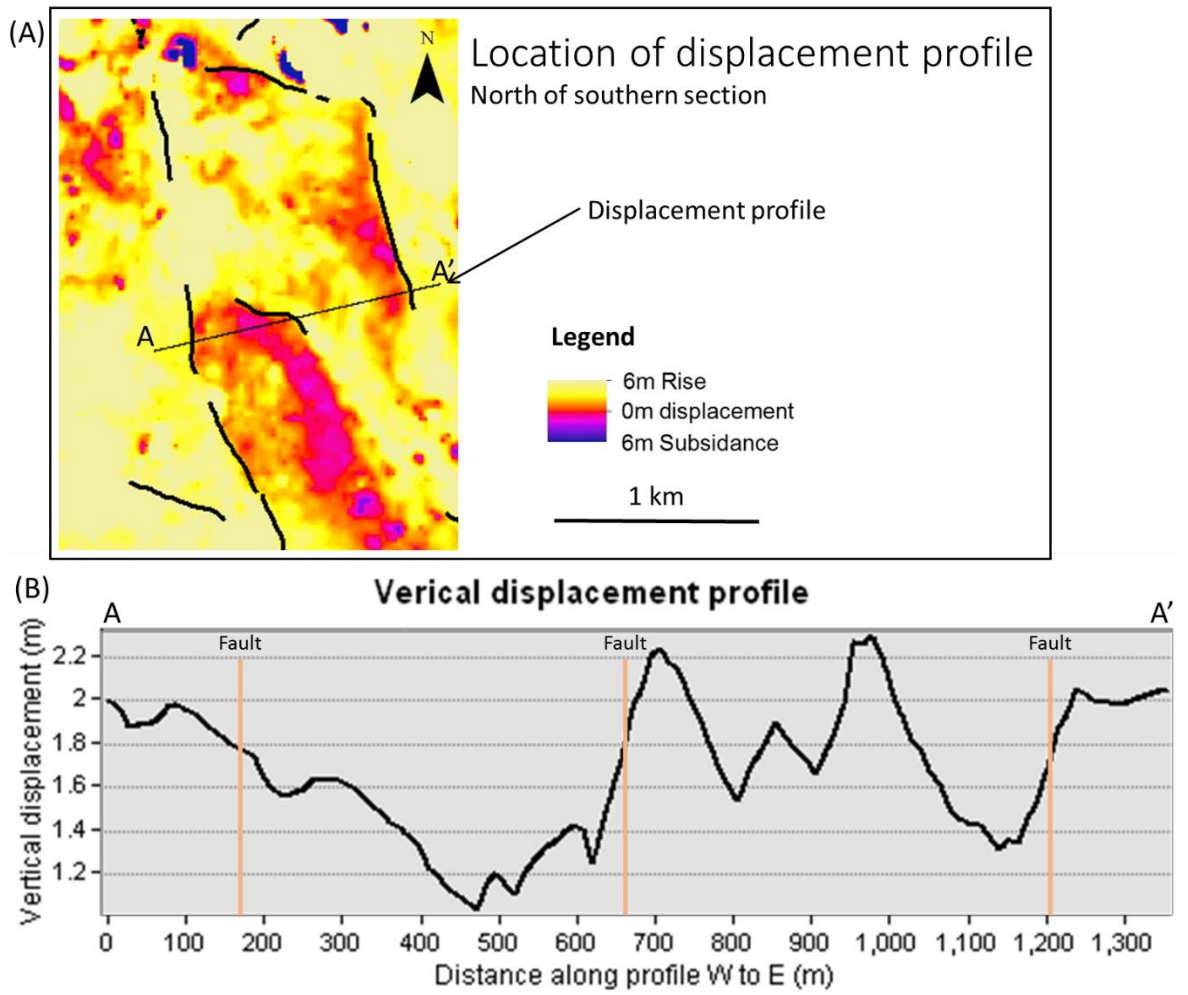

Figure 2.10: (A) Uplift map produced by differential 3D photogrammetry showing the impact of secondary faults on deformation. (B) A vertical displacement profile across the anomalous SJF trace and eastern secondary faults to emphasise their impact on uplift.

2.5. Discussion

2.5.1. Limitations and errors

The main limitations to this study are due to field accessibility and the extent and quality of datasets. Restricted access to the field area in commercial logging land and dangerous terrain meant that these zones have no field data and rely on interpretation from remote datasets. Data quality and coverage limit the level of interpretation that can be made remotely. For example, 3D photogrammetry data has significant flight-line issues in the north where the trace can also be poorly resolved. Additionally, landslides, erosion, settling, new lakes and moving waterways are an issue with all remote sensing datasets used. These factors increased the importance of field work for ground-truthing the interpretations. Even with 12 days of field work which permitted 95% to the main trace to be walked and many of the

secondary faults to be discovered and characterised, it is likely that many smaller (e.g., <200 m length and displacements <0.3 m) secondary faults in the SJF region where not catalogued and mapped during this study. This sampling issue will have been particularly important in rugged topography rarely visited by researchers and landowners. The problem of missing small secondary faults was exacerbated by the narrow width (e.g., 3-4 km) of the LiDAR swath along the SJF. For example, the long secondary trace west of the Central SJF near the Charwell River (trace b in Fig. 2.4 B) was not covered by LiDAR and was only discovered as it crossed an access road.

The Trimble GeoX7 GPS was used to georeferenced field measurements and where required, map fault surface traces. On the scale of the study error in GPS is neglectable, consistently less than 10cm.

Error in offset data is more complicated. The error in ability to measure the offset varied with the quality of the strain marker being measured. Discrete vertical displacements of a single trace faults were often measured by scarp height on flat land and typically had low errors, normally regarded as ±2cm. Dispersed multi-trace fault zones and lateral offsets measured by displaced cultural markers, tree roots and animal tracks all had significantly higher but unique errors. For example, deer fences had much larger spacing between fence posts, and not all fences were originally straight. To allow for the range of errors the estimated error and strain marker was recorded beside any complex sites. For simple situations, the strain marker was recorded and later assigned a standard error for that strain marker. When compiling data only reliable measurements where assigned to each fault in the database. Others were listed as estimates in the notes for each fault.

When studying figure 2.7 it is important to realise all traces were sampled and therefore there is a strong representation bias. Due to the consistent orientation of the SJF most fault traces are orientated N to NW, and there are few opportunities to sample SJF traces with an easterly strike to examine their slip sense see if they are dextral. In addition, too few secondary faults were recorded to establish their kinematics in a statistically robust way.

2.5.2. Prehistoric SJF ruptures

As previously noted, (section 2.3.1) the Northern Section of the SJF (i.e. across the length of the Stone Jug terrace surface west of the Charwell River), is the only part of the primary trace that had a significant pre-existing fault scarp. The low displacement (<25cm vertical) along this section of the fault during the Kaikōura event appears to be inconsistent with fault scarp heights which are up to 5 m on the 13 kyr Stone Jug surface (Bull 1991) and rise towards the Conway-Charwell and Hope faults. If displacement in 2016 was atypical of previous events along the Northern SJF, then questions can be asked as to whether rupture of the entire fault in 2016 was atypical of past behaviour. The high scarps on the Stone Jug surface may suggest that some past surface-rupturing earthquakes on the SJF only ruptured the northern end of the fault and could, for example, have been triggered by events on the Hope Fault. Therefore, it is possible that the displacement distribution and rupture patterns for the SJF vary between events, with the SJF rupturing together with other nearby faults (e.g., Hope, Conway-Charwell, Hundalee faults, Oaro river).

Finally, five of the secondary fault traces had pre-existing scarps and probably ruptured the ground surface repeatedly during the Holocene. For example, the small cluster of secondary faults the west of the central left step (highlighted on the right of figure 2.4 B) appear to be a young set of faults that have ruptured previously and produced small pre-existing swamps and ridge saddles. These faults are short, unconnected and have very low displacements (<20 cm) and appear to have formed in association with a 0.4 km wide left step in the primary SJF trace. I hypothesise that many of the secondary faults mapped in this study also ruptured with the primary trace in previous events. If this is the case then, the SJF may have ruptured multiple times during the Holocene, although the timing of these events is only constrained at the northern end of the fault (see Chapter 4). The absence of a mapped pre-existing Holocene trace along the Central and Southern Sections of the primary fault trace could reflect the fact that these parts of the trace run along active streams and steep terrain which would not favour fault scarp preservation.

2.6. Conclusions

The SJF has an average strike of 160, connecting the Conway-Charwell and Hundalee faults and has a length of ~19 km. It ruptured along almost its entire length during the 2016 Kaikōura Earthquake and comprises a primary fault trace and many smaller secondary traces. In detail, the primary trace comprises of 2 steps and multiple bends. These bends facilitate the sigmoidal shape of the primary trace, which generally strikes N-S in its Central Section and NW at both ends. The SJF is mainly an oblique slip fault comprising varying amounts of left-lateral displacement and contraction. Displacement profiles for horizontal, vertical and net slip along the primary trace of the entire fault show two main maxima separated by a section of low displacement towards the middle of the fault and zero displacement at both ends of the fault. In detail variations in the relative amounts of horizontal and vertical displacements on the primary trace are related to changes in fault strike and intersections of the primary trace with secondary faults. Complementary changes in displacements of the primary and secondary faults suggested that they are kinematically related and may frequently rupture together. Pre-existing fault scarps on both the primary and secondary 2016 traces support this kinematic coherence argument, suggesting that both may have ruptured repeatedly during the Holocene. Despite these this co-rupture it remains possible that prehistorical surface ruptures of the fault had dissimilar rupture patterns and displacements to the 2016 event.

Chapter Three: Relationship of fault geometry to basement bedding

3.1. Introduction

Previous studies in the North Canterbury region have postulated that the orientation of many faults that ruptured in the 2016 Kaikōura Earthquake, including the leader and Stone Jug faults (SJF), partly or entirely utilised pre-existing bedrock fabric (e.g., Nicol et al., 2018). For these faults, regional stresses during the Quaternary are inferred to reactivate pre-existing planes of weakness in Torlesse Supergroup basement. Preliminary visual inspection of maps created in Chapter 2 suggests that the SJF often strikes sub-parallel to basement bedding. In this chapter I use statistical analysis of previous geological mapping of basement (e.g., Rattenbury et al., 2006) and remote sensing data (LiDAR-derived digital elevation models), to test the parallelism of basement bedding and 2016 faulting in the study area. The analysis enables conclusions to be drawn about the control of basement structure on the strike and dip of the SJF.

The SJF displaces Quaternary river and fan deposits, Late Cretaceous and younger coastal to marine strata immediately south and west of the Charwell River and interbedded greywackes and argillites of the early Cretaceous Torlesse Supergroup (Crampton, 1988; Warren, 1994; Rattenbury et al., 2006). Thick (e.g. 2-50 m) greywacke beds within the Torlesse produce strike ridges that are widely observed across the study area and indicate that bedding mainly strikes N-NW (Fig. 3.1). Mapping of basement suggests that this bedding mainly dips steeply (≥60°). Basement is separated from Late Cretaceous and younger strata by a regional angular unconformity, with basement bedding typically steeper than that of the overlying strata. The southern-most 11 km of the SJF displaces Torlesse basement (Fig. 3.1) and this investigation is confined to the Central and Southern sections of the SJF.

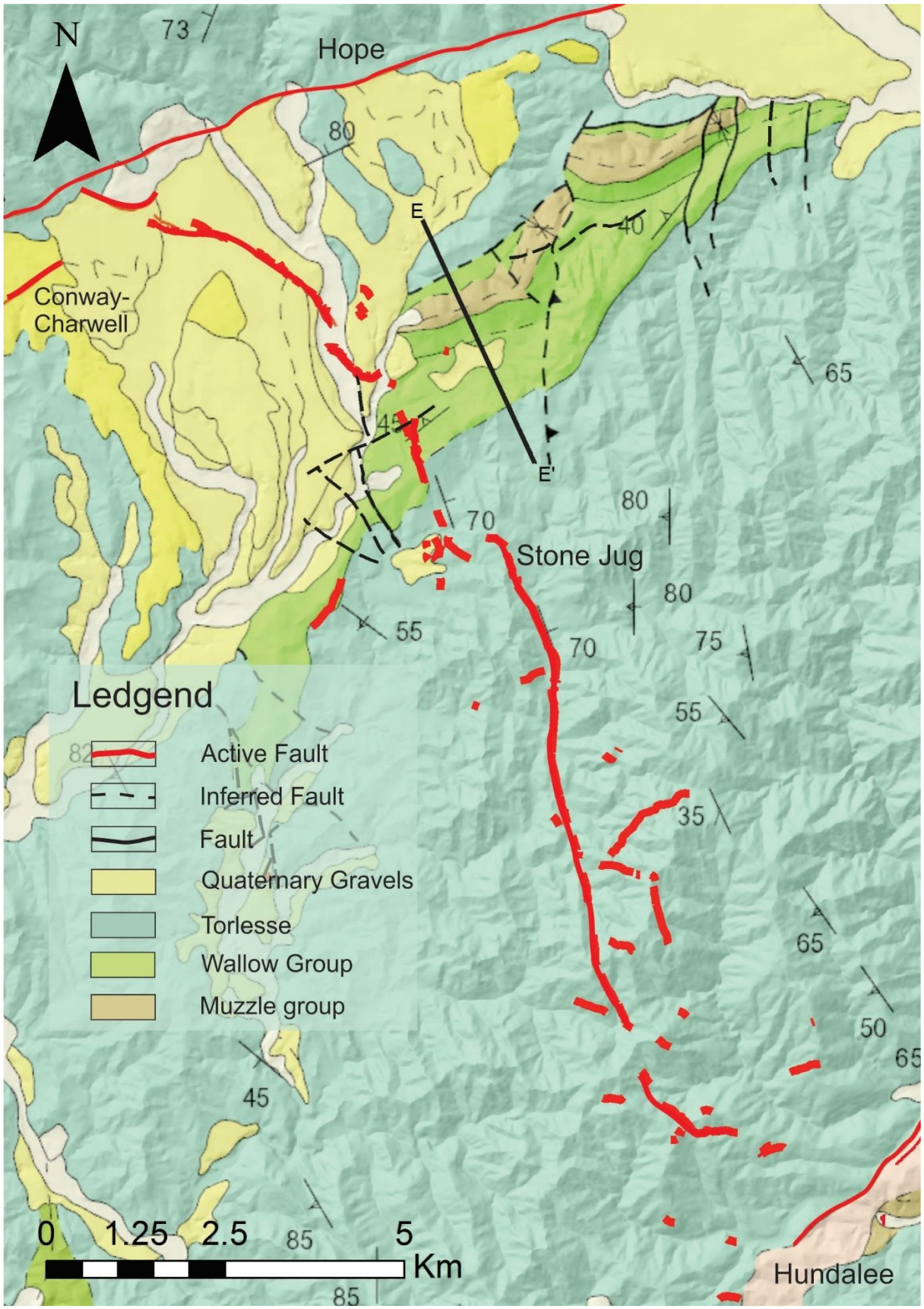

Figure 3.1: Geological map of the region surrounding the SJF modified from Rattenbury et al. (2006) (Crapton 1988). This map includes all known faults, bedding (lines with ticks, triangles on bedding symbols indicate younging direction) and key rock units. Figure 1.4 contains the cross-section E to E'.

3.2. Methodology

To analyse the relationships between the orientations of basement bedding and the SJF, as defined by the 2016 rupture, both remote-sensing datasets and field outcrop data were sampled manually. The majority of bedding data were acquired remotely by manually identifying bedding strike-ridges for resistant sandstone beds in LiDAR where they protrude above the surrounding landscape. LiDAR interpretation was limited to the mountainous regions along the Central and Southern sections of the SJF, south of Limestone Creek, and excluded the Northern section of the SJF where it crosses river terraces and Late Cretaceous or Cenozoic strata.

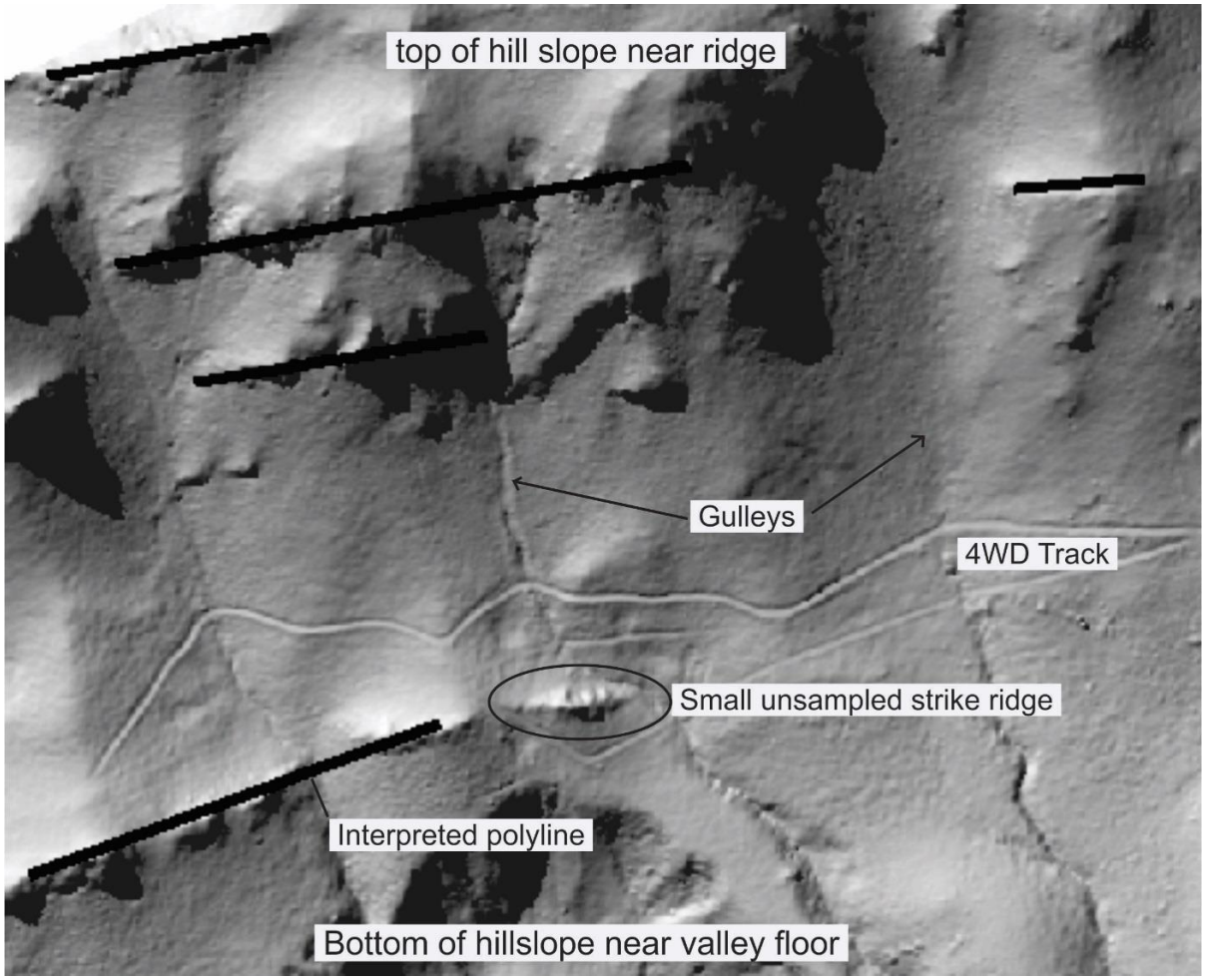

Figure 3.2: Interpreted Torlesse strike ridges on a hillshade derived from LiDAR. This figure shows an example of how strike ridges were identified and sampled.

The strike of Torlesse bedding was remotely analysed through manual interpretation by LiDAR (Fig. 3.2). For individual strike ridges, a linear polyline was manually fitted by eye to the centre of each bed (Fig. 3.2). As these strike ridges are typically long relative to their width (aspect ratios generally exceed 50:1) uncertainties in the measured strikes are estimated to be <±5°. In some instances the orientation of the strike ridge varied by up to 20° along strike and an average strike for the bed was estimated by eye, resulting in uncertainties in strike of up to <±10°. In all cases, the 'Linear Directional Mean' tool in ArcMap was used to calculate the precise ridge trend, which for the purposes of this study is assumed to provide a proxy for strike of bedding. Where possible the inferred strike values were compared to bedding measurements from the strike ridge or within several hundred metres of the ridge. These field measurements were from this thesis and from previous publications (Warren, 1994; Rattenbury et al., 2006). The comparisons indicated that the measured bedding strike and the remotely inferred bedding strikes were similar and support the use of the technique. All bedding strikes were normalised to orientate south (between 90° and 270°) in accordance with field observations, as individual bed dip direction was unknown.

The trends of the primary fault-trace have been compared to all local bedding trends within six 2x2 km boxes. Figure 3.3 shows the SJF trace, interpreted basement bedding data polylines and the six boxes that they were interpreted within. The box analysis was devised to reduce the subjectivity associated with deciding which fault and bedding measurements to compare. As fault trends were generally uniform throughout each box, along strike changes in fault trend do not significantly impact the comparison of beds with the fault. The 2x2 km size of each box was selected to capture a statistically significant data population in each box and to minimise the possibility of inadvertently capturing along-strike variations in the fault orientation. The precise locations of the boxes do not impact the first-order conclusions of this chapter. The datasets include a total of 27 fault traces and 187 remote bedding measurements which were analysed in Excel and ArcMap to produce the plot in Fig. 3.4.

Probability density and linear regression modelling were both used to determine the strength of the bedding-fault relationships. Spatial analysis of the data helped help improve understanding of bedding-fault relationships, biases in the data and anomalies where fault traces differed from bedding.

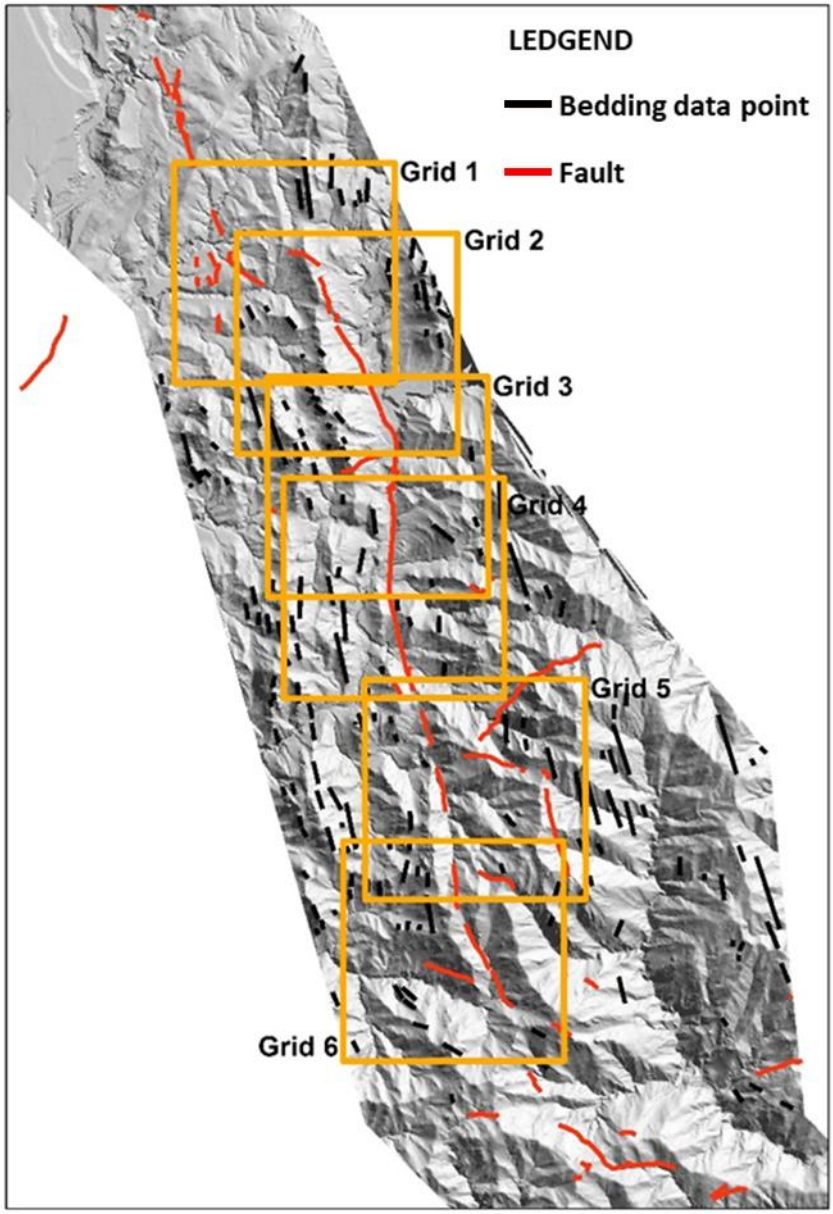

Figure 3.3. Map showing the locations of data sampling boxes (orange lines), remotely derived basement bedding trends (black lines) and active fault traces (red lines. Six 2x2 km boxes (labelled box 1-6 from north to south) were used for the analysis presented in Fig. 3.4. The background is a hillshade illuminated from the northeast.

3.3. Observations from maps

Visual analysis of the SJF in Figure 3.1 indicates that the main trace appears to be sub-parallel to basement bedding for much of its length. In the south basement bedding mainly strikes about ~150°, dips steeply and is approximately parallel to trend of the primary fault trace. In the Central section of the fault, the trends of the trace and of the bedding are also approximately parallel with ~170° orientations. Further north in the monkey face area and

south of the Charwell River, the trends of fault traces locally vary from ~270-360° and display a regional northward swing in trend towards the NW. These northern traces have significant branching and multiple parallel traces at the surface, which is not routinely observed along the entire length of the SJF.

3.4. Box-sample analysis

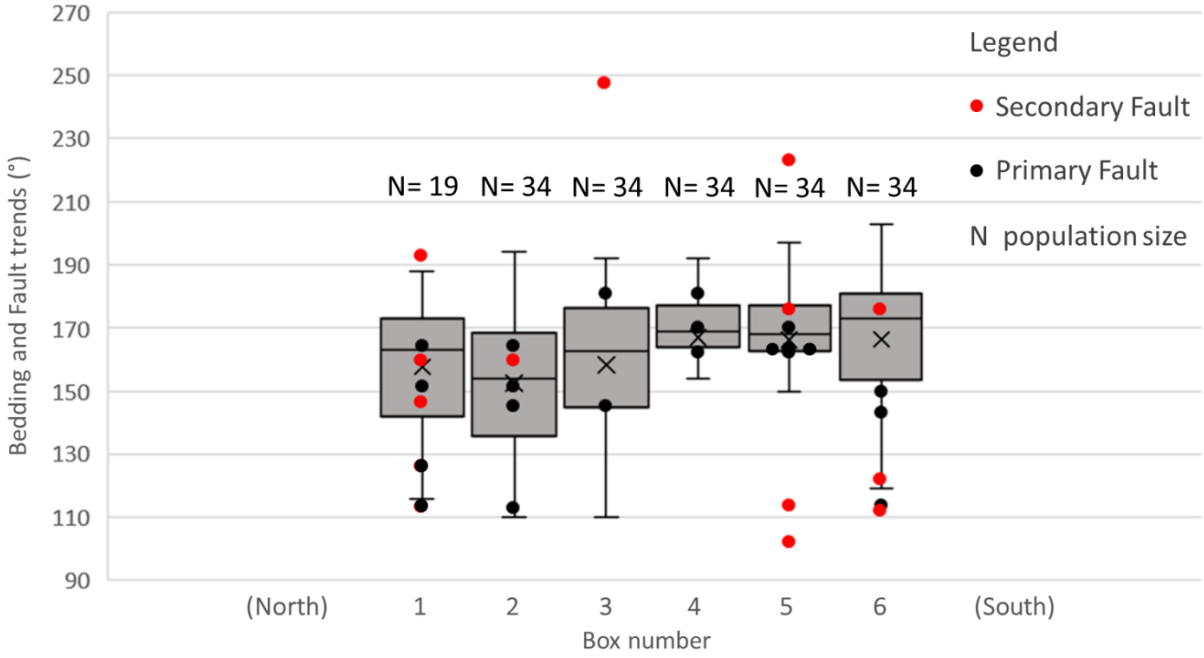

Figure 3.4: Comparison of local fault-trace and bedding trends. Data presented separately for each 2x2 km sampling box (see Fig. 3.3. for box locations). The orientations of fault traces are shown by the black (primary trace) and secondary (red) dots, while the trends of bedding are displayed as grey box (interquartile range) and whisker (range). The horizontal line and "x" in each box are the median and mean values for bedding trends. Numbers adjacent to each box indicate the number of bedding observations used to generate each box and whisker. For the purposes of this plot, the structural trends are considered uni-directional and plotted in the southern quadrants.

Figure 3.4 shows that most fault traces are generally parallel to the trend of bedding. Analysis of the data for each box indicates that in all cases except box 6 one or more of the measured fault trends falls within the interquartile range of bedding trends indicated by the grey box. The mismatch of bedding and faulting in box 6 suggests a ~20° discordance between bedding and faulting with the latter apparently having a more easterly trend. This more easterly trend may arise because to SJF is swinging more rapidly in strike towards the strike

of the Hundalee Fault than the bedding. Local differences in fault and bed trends may also arise due to complexities in the fault trace. For example, 114° fault-trace outlier in both boxes 1 and 2 was measured at a local step over which does not reflect the regional fault trend and may locally depart from the trend of bedding. All SJF traces that deviate from the interquartile range can be explained by similar local variations in fault geometry.

The following observations are borne out of the statistical comparison of the primary fault trace and basement bedding within a 1 km radius of that trace. There is a strong correlation between basement bedding and fault strike for all but the left stepping fault trace in box 1 (see description above). When this left step is removed from the statistical analysis, the average difference between the mean trend of bedding and the nearest fault trace was 7.9° with a standard deviation of 5.9°. This analysis indicates that ~95% of fault traces are within 19.7° of the average trend of local bedding. Additionally, linear least-squares regression of a plot of bedding trend versus primary-fault trend produced an R^2 value of 0.6 suggesting a reasonable correlation between these two variables (and trend parallelism).

Many secondary fault traces have trends in the range ESE-ENE and are not parallel to the trends of bedding or the primary fault. This conclusion is supported by statistical analysis of the data which suggest that the mean and standard deviation for the difference in trends between bedding and secondary traces are 44° and 27°, respectively. Additionally, linear least-squares regression of a plot of bedding trend versus secondary-fault trend produced an R^2 value of 0.02, suggesting a very poor correlation between these two variables. Therefore, secondary faults generally did not utilise planes of weakness in the Torlesse. As observed in chapter 2 some of the secondary traces coincide with changes in the geometry and displacement of the primary fault trace. In such cases, the location and geometry of these secondary faults may be driven by changes in the geometry and kinematics of the primary fault and not by the locations and properties of heterogeneities in the basement.

3.5. Discussion

3.5.1. Limitations and errors

The combined analysis of geology and LiDAR data produces internally consistent results, which I believe are broadly defendable. However, like all such studies, the analysis is associated with some uncertainties. Firstly, the sampling method only recorded larger-scale (100+ metres) general trends of resistant beds and fault-trace orientations in mountainous regions. In general, there were insufficient data to compare the strike of bedding and fault planes at outcrop scale. Therefore, although it is assumed that the conclusions presented here are independent of scale, this assumption has not been tested. Secondly, the box-sampling technique was used to overcome subjectivity, however, it may have introduced some sampling artefacts. For example, in the NW corner of box 6 (Fig. 3.3) bedding was sampled up to 2.8 km from the primary fault trace which, at this location, is bending in strike towards sub-parallelism with the Hundalee Fault. To address such sampling problems a 2x2 km box size was adopted (larger box sizes exacerbated the problem). Thirdly, strike ridges were not uniformly distributed across the study area and in some areas LiDAR coverage was not available. These sampling issues resulted in some traces not being compared to all bedding in the target area. Conversely, areas of clearly defined bedding resulted in high densities of data points. In such cases, all bedding samples were recorded and assumed to be representative of the bedding adjacent to the fault trace. In addition, the box-sampling method had the effect of averaging data over 2x2 km regions and smoothing variations in the spatial distribution and orientations of the bedding (thus removing local anomalies).

3.5.2. SJF and the transpressional fault model

All measures used here indicate a strong correlation between fault-trace trends and Torlesse bedding trends, consistent with the view that orientation of Mesozoic basement has locally influenced the location and orientation of the SJF. The northerly strike of this mainly left-lateral fault varies by ~30-40° from the strike of left-lateral faults that would be predicted for a transpressional fault model and a ~120° trending PHS direction (Sibson et al., 2011; Nicol et al., 2018). The data presented here suggests that the more northerly strike of the SJF (than predicted by the transpressional model), may partly reflect its reactivation of basement heterogeneity (e.g., bedding surfaces and bedding parallel pre-existing faults). For such reactivation, the basement fabric contains zones of weakness that, despite being misaligned

to the present-day stress field, are sufficiently weak to promote slip and possibly also cause local rotation of the principal stress axes (Sibson et al., 2011; Massiot et al., 2019). Such weak zones may comprise clay-rich material with a low coefficient of friction (e.g., <0.3) or elevated pore fluid pressure, although no data was collected as part of this thesis to test these possibilities.

At the Northern and Southern sections the SJF strike bends approximately to the NW and have an orientation that is close to what is predicted for left-lateral faults in the transpressional fault model for a homogeneous medium in North Canterbury (see Fig. 14 in Nicol et al., 2018). Despite the close alignment of the model and the SJF strike, it appears that the fault may still parallel Torlesse bedding in these areas. Inspection of the bedding and fault data in Fig. 3.1 suggest that bedding and the primary fault trace are parallel in the southern area. To the north the fault is buried by up to 600 m on Late Cretaceous to Cenozoic rocks and the parallelism of basement bedding and fault strike cannot be demonstrated. Independent of whether the northern and southern ends of the SJF were influenced by basement bedding, displacement data presented in Chapter two suggests that slip in 2016 was lowest on those parts of the fault most favourably aligned for slip. These low displacements suggest that the slip on a fault surface during earthquakes are less to do with how favourable oriented they are in the regional stress regime and perhaps more related to changes in the stress field induced by nearby faults.

3.6. Conclusion

For most of its length, the Stone Jug Fault is contained within Torlesse basement rocks. Comparison of the trends of sandstone strike ridges and fault trace trends formed along the SJF has been conducted using LiDAR data and outcrop measurements. These data indicate that the trends of Torlesse bedding and the primary SJF trace are similar, suggesting that the orientation of the fault surface is at least partly controlled by the basement fabric. Although the bedding surfaces appear to be misaligned for slip in the contemporary stress regime, they may accommodate slip because they represent zones of weakness that are exploited by the active faulting.

Chapter Four: Paleoseismic history of the Stone Jug Fault

4.1. Introduction

The Kaikōura Earthquake ruptured at least five discrete faults at the ground surface south of the Hope Fault and in the North Canterbury region (Fig. 1.2). Fault ruptures in the North Canterbury region appear to have occurred on low slip rate faults (e.g., < 1 mm/yr; Pettinga et al., 2001; Barrell and Townsend, 2012) and are critical for establishing how frequently Kaikōura type events occurred in the geological past (Litchfield et al., 2018; Nicol et al., 2018). This MSc thesis is part of a wider project to determine the paleoseismic histories of four faults that ruptured during the Kaikōura Earthquake ('The Humps', Leader, Conway-Charwell and Stone Jug faults), and two faults that do not appear to have ruptured during the earthquake (Jordan Thrust and Hope faults) (Fig. 1.1). With the exception of the Hope Fault (see McMorran 1991; Pope, 1994; Langridge et al. 2003; Coulter, 2007), no paleoseismic data were available for these faults (including the Stone Jug Fault) prior to the 2016 earthquake, although age estimates for displaced landforms in North Canterbury suggest possible recurrence intervals in the order of ~5-10 thousand years (Pettinga et al., 2001; Barrell and Townsend, 2012).

Excavation of two trenches across the Stone Jug Fault (SJF) was undertaken in January to February 2019 to determine the paleoseismic history of the fault. In this chapter radiocarbon dating (^{14}C) of organic material and dating of feldspar in silts using Optically Stimulated Luminescence (OSL) have been employed to characterise the timing of prehistoric fault rupture of the SJF during the Holocene. These data together with apparent vertical displacements of horizons exposed in the trench walls constrain the earthquake recurrence intervals (RI), single event displacements (SED) of surface ruptures and slip rates on the SJF. Here data are presented in support of estimates of these parameters. The implications of these data for seismic hazard and their relations to nearby faults that ruptured during the Kaikōura Earthquake are discussed.

4.2. Data and Methods

Late Quaternary stratigraphy exposed in trenches excavated across active faults yield information about the timing of prehistoric earthquakes, near-surface geometry and displacements of active faults (e.g., Sieh, 1978; Meghraoui et al., 1988; Fumal et al., 1993; McCalpin, 2009). At carefully chosen trench sites, varying degrees of deformation of dateable stratigraphy provide a means of dating prehistoric earthquakes. In these circumstances, absolute dating of the stratigraphy, usually by radiocarbon dating (14C) of organic material, provides a means of estimating the timing and size (displacement of the ground surface) of events. We adopt these well-established techniques to determine the history of surface rupturing earthquakes on the SJF at two trench sites (Fig. 4.1). Data from the trenching are combined with slip magnitudes and orientations from the 2016 rupture to determine whether this recent event was 'characteristic' of past events on the fault.

4.2.1. Trench locations and methods

The location of suitable trench sites is key for yielding information on the paleoseismic histories of active faults. In selecting two trench sites on the SJF the following criteria was used; 1) little or no cultural disturbance of the ground and/or near-surface deposits (e.g., deep ploughing or road construction); 2) the prospect of dateable stratigraphy adjacent to the fault deformed or displaced by the fault (e.g., carbonaceous material and/or silts); 3) a vertical component of displacement that may promote accumulation of fine sediment against the fault; 4) a single slip surface or narrow (<20 m wide) zone that can be trenched across its entire width; 5) geomorphic evidence of faulting prior to the Kaikōura Earthquake, 6) excavator access to the sites; and 7) landowner permission to undertake trenching. Poor excavator access and stratigraphy ruled out most potential trench sites along the SJF leaving only locations on northern terraces adjacent to the Charwell River to consider. Northwest of the Charwell River the SJF accommodated <20cm surface displacement during the Kaikōura Earthquake and was either vegetated, submerged in a swamp or defined by a large 2m – 5m scarp that would be difficult to trench and correlate stratigraphy across. Two potential sites, northwest of the Charwell River, were investigated in the field and found to present a flood risk with little prospect of dateable sub-surface stratigraphy. Following a series of hand augers across 2016 fault scarps, two locations were selected for excavation. These trenches are referred to as "Stone Jug trench 1" (SJT-1) and "Stone Jug trench 2" (SJT-2). They were

excavated to maximum depths of ~2 m (SJT-1) and 1.8 m (SJT-2), into the Stone Jug terrace surface and across a swamp formed on a degradation surface, respectively. The Stone Jug terrace surface at the SJT-1 site is approximately 55m above the active channel of the Charwell River, was abandoned about 11±1 kyr BP (Bull, 1991; this study) and is the oldest terrace displaced by the fault. All Bull's errors for ages are quoted at the 1σ level unless stated otherwise. The SJT-2 trench terrace is 21 m above the modern river (the 5th oldest terrace of 11; see Fig 4.1.A) and based on the down-cutting curve of Bull (1991), has an estimated age of 6.3±0.5 kyr (see text in section 4.4 for further discussion). The trench was excavated across a swamp containing peat and carbonaceous soil up to ~0.4 m thick, which appears to have formed in an abandoned river channel crossed by the fault trace (Fig. 4.1.C). Therefore, the trenches collectively provide information on Holocene paleoearthquakes, with SJT-1 providing a possible record of Early Holocene and younger events, and SJT-2 mid-late Holocene surface-rupturing earthquakes.

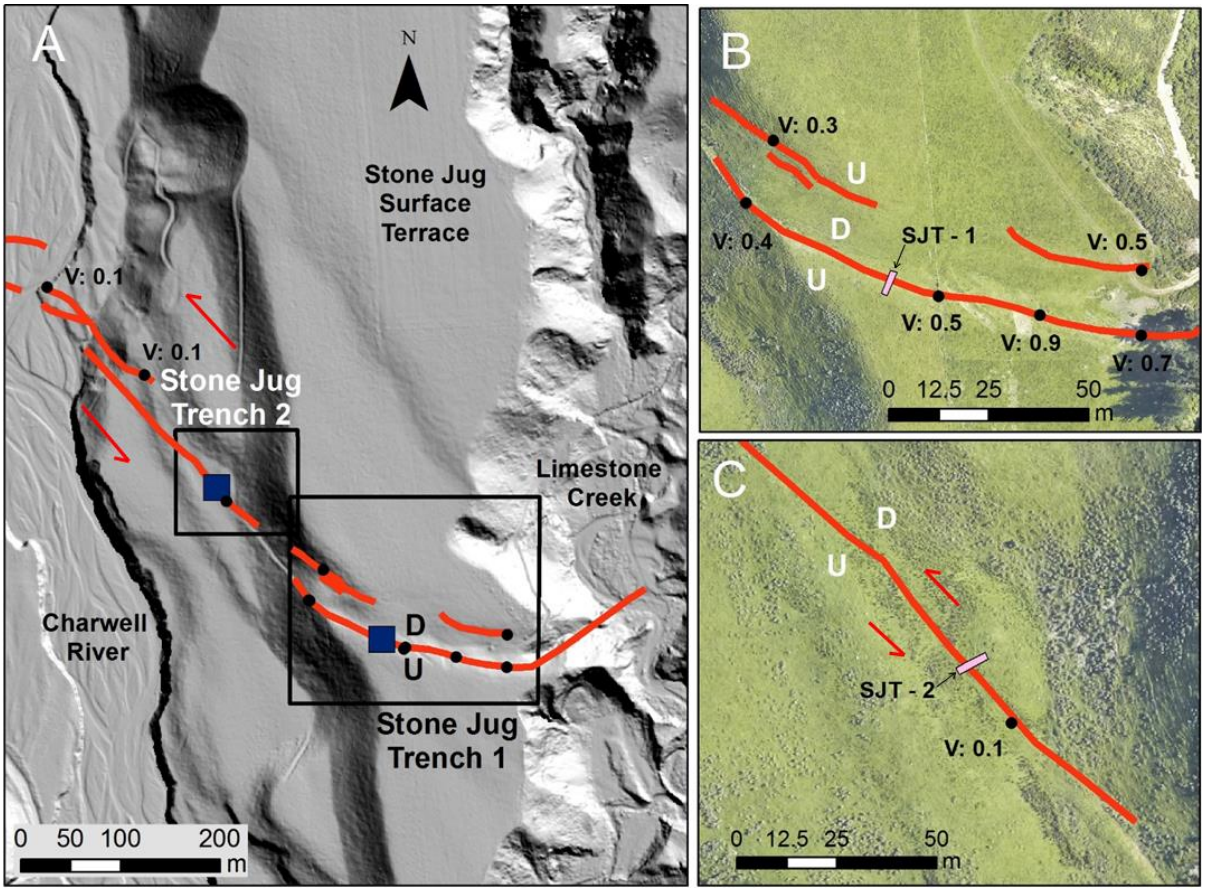

Figure 4.1: SJF trench locations. A shows trench locations relative to the Charwell River on the left of the frame with a Lidar hillshade as a background. B shows an aerial photograph of the SJT-1 trench and the graben structure it is located in. C shows an aerial photograph of the terrace and swamp the trench would be excavated in immediately post the Kaikōura earthquake. The swamp appears as darker green reeds rather than grass or shrubs and has grown since the photo was captured. All displacements are in meters with errors of 0.05m.

The trenches were excavated using a 12-tonne excavator. SJT-1 was 3m wide, 13m long and ranged in depth from 1 m in the footwall to 2.2 m in the immediate hangingwall of the fault. The walls of the trench were approximately vertical and oriented N-S perpendicular to the fault trace (Fig. 4.1.B). The SJT-2 trench was excavated across the swamp for 15 m normal to the fault trace in a SW-NE direction (Fig. 4.1.C). The trench crossed the fault on the NE side of the swamp where 6 m of both walls were logged to a depth of up to 1.8 m.

Following excavation, the walls of both trenches were cleaned and gridded at 1x1 m using string lines. The walls of the trenches were then photographed and logged at a 1:20 scale. Logging of stratigraphic contacts and fault zone structure was undertaken using a tape measure to locate key boundaries relative to grid nodes. The resulting trench logs are presented in Figures 4.5, 4.6, 4.8 and 4.9.

Stratigraphic units were described, and samples were taken for two radiocarbon (C-14) and four Optically Stimulated Luminescence (OSL) dates of key stratigraphic units (Tables 4.1 & 4.2). For details of these dating techniques refer to the literature (McCalpin, 2009) and for information on the samples and their processing see Appendix 3 and 4. C-14 samples were extracted from the outcrop using a sharp knife, placed in air-tight bags and labelled. OSL samples were collected by hammering 8 cm steel pipes into silt layers until they were full of sediment. Once extracted from the trenches walls each sample was wrapped in tinfoil, completely covered in duct tape and labelled. Samples were dated by the Waikato University Radiocarbon Dating Laboratory and by the OSL Dating laboratory at the Victoria University of Wellington. Unless otherwise stated C-14 ages in the text and on the trench logs are presented in calibrated years BP (i.e., years before 1950) with 2σ measurement uncertainties. OSL samples are quoted in years BP at the 1σ level.

Slip orientations and magnitudes during the Kaikōura Earthquake at the trench sites may provide additional information to constrain the timing and size of paleoseismic events. The orientation and kinematics of the SJF differ between the two trenches. At the SJF-1 site, the trench was excavated across the primary southern trace of an asymmetrical graben which is defined by faults striking approximately WNW-ESE. During the Kaikōura Earthquake displacements at this site were dominated by vertical slip which locally produces thickening of cover beds on the terrace surface adjacent to the fault. On a fence line 80 m west of SJT-1, and at the western end of the WNW-ESE striking section of the fault, displays 0.4±0.1 m vertical displacement and 0.15±0.1 m horizontal displacement. On a second fence line, 25 m east of SJT-1 at the edge of the graben recorded 0.4±0.1 m vertical displacement and no measurable horizontal displacement (i.e. <0.1 m). At SJT-1 0.6±0.1 m and 0.8±0.1 m, vertical displacements were observed in the west and east walls of the trench, respectively. Therefore, an average of 0.7±0.1 m vertical displacement and zero horizontal displacement has been adopted for the 2016 surface rupture at SJT-1. At this site the fault is upthrown to the south and dips northwards, accommodating mainly normal displacement and extension, consistent with the formation of the graben.

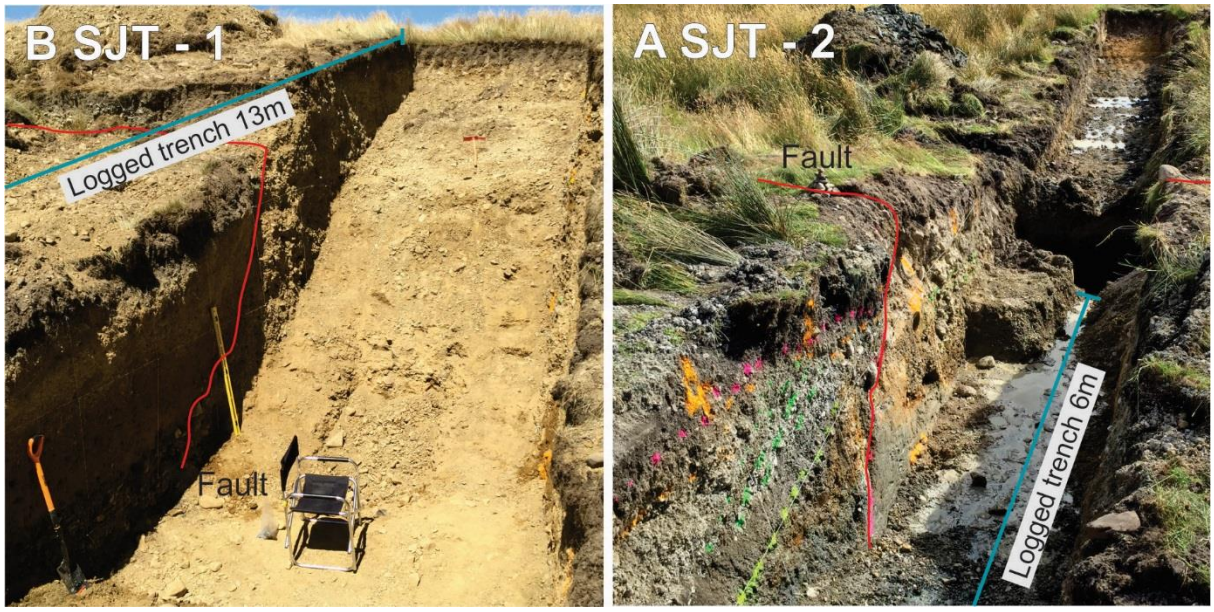

Figure 4.2: Excavated trenches. Photographs taken by Kate Pedley.

At the SJT-2 site, the 2016 rupture forms a right-stepping, semi-continuous rupture at the ground surface, which trends approximately northwest. The closest reliable single trace displacement measurements on the northwest striking section of the fault were recorded on a deer fence along the southern edge of the Inland Road, 2.0 km north of SJT-2. On this deer fence, we measured 0.4±0.1 m horizontal (left-lateral) and 0.15±0.1 m vertical displacement (down to the northeast). The magnitude and direction of vertical displacements are consistent with the SJT-2 site where the 2016 scarp was ~0.1 m high. We infer that 2016 slip at SJT-2 was also dominated by left-lateral displacement, although this interpretation does not impact our interpretation of pleoearthquakes.

Figure 4.3: Colin Amos and Bradley Scott inserting an OSL sampling pipe, to sample (SJM1/WLL1269) from a silt lens on the western wall of SJT-1. This photograph was taken by Kate Pedley.

Stratigraphic mapping and dating from each trench, in combination with measurements of 2016 displacements at the trench sites, have been used to infer the timing and vertical displacement of paleoseismic events during the Holocene. Earthquake recurrence intervals have been estimated for the last three events (including 2016), while average recurrence intervals (RI_a) for the Holocene were calculated using the single event displacement (SED), total vertical displacement (TD) and the maximum age (MA) of cover beds in SJT-1 (i.e. RI_a = SED/(TD/MA)). Vertical displacements of units correlated across the fault were used to determine displacements. Displacement of Kaikōura and any previous events can be used to determine an average event for the SJF. In SJT-1 geometries and sedimentology of colluvial material sourced from the fault scarp can also be used to estimate SEDs. This data has also been used to estimate a minimum slip rate at the SJT-1 site.

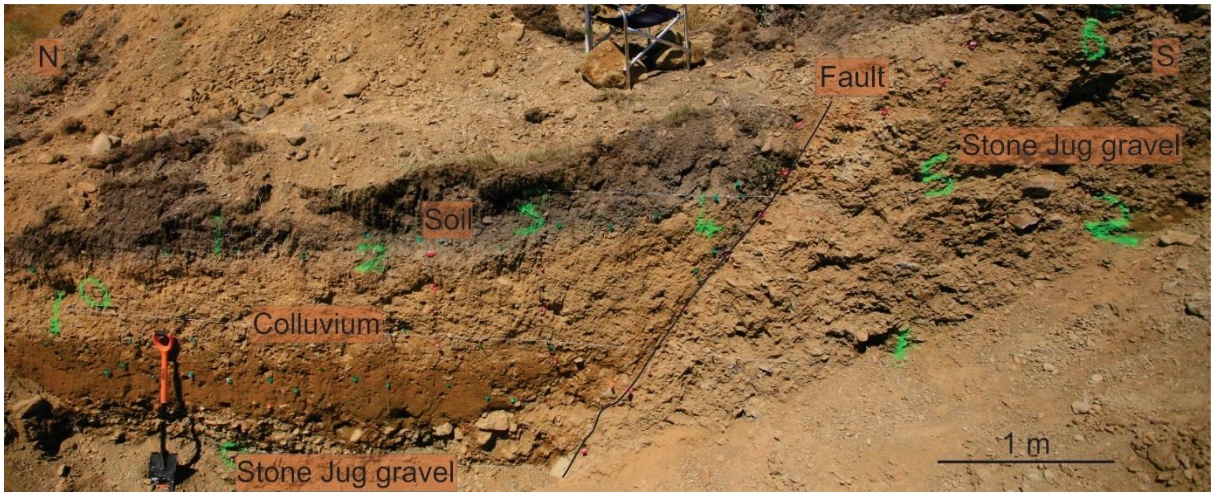

Figure 4.4: SJT-1 east wall during initial analysis. The hanging wall discolouration is due to gradual drying from the top. This photograph was taken by Kate Pedley. Paint numbers denote the grid used to log the wall.

4.3. SJT-1 Observations

4.3.1. Unit descriptions

SJT-1 exposed four primary stratigraphic and pedalogical units, here labelled 1, 2, 4, 8. The basal alluvial gravel deposit (unit 1) continuously exposed along the lower 0.5-1.5 m of the trench (Figs. 4.5, 4,6). This unit (1) is dominated by poorly to well sorted, sub-rounded clasts up to 30cm long. These clasts mainly comprise Torlesse Supergroup sandstone. These gravels are locally interbedded with lens-shaped silt and sand interpreted to have been deposited in paleochannels. Two significant lenses were logged separately as unit 5 in the trench walls, although multiple smaller-scale (< 1 m long or < 0.2 m thick) lenses are also present. In addition to these silt/sand layers, unit 1 has a weak bedding fabric produced by weak sub-horizontal clast long-axis orientations and subtle changes in gravel clast sizes. An OSL sample from a silt lens in the western wall of the trench at a depth of 1.3 m, returned an age of 29.3±2.5 kyr and indicate that these gravels were likely deposited during the last glaciation (Table 4.2, sample SJM1 / WLL1269).

A silt and fine sand lens (unit 2) overlie the basal gravel unit in the hanging wall of the fault. This unit is massive and approximately wedge-shaped (Figs. 4.5, 4.6). On the western wall of the trench unit 2 forms a sharp contact with the overlying unit 4a and abuts the fault surface. On the eastern wall unit 2 is inter-fingered with unit 3, which is a poorly sorted sandy pebble gravel with a silt matrix and sub-rounded clasts. Similarly, unit 4 comprises a mix of silt, sand

and sub-rounded pebbles, with the occasional cobble-sized clast; unit 4a containing fewer pebbles than 4b. Unit 4 in the east wall and unit 4a in the west wall of the trench are typically matrix supported and thin (from ~1.3 to 0.8 m) with increasing distance from the fault. Unlike unit 2, units 3 and 4 display a weak bedding fabric which reflects minor changes in grain size and dips away from the fault. No stratigraphic boundaries are identifiable in unit 4, although the lower third has a higher sand content and the upper third more cobbles. Units 4 and 1 grade upwards into the soil A horizon (unit 8) which is 15-20 cm thick in the fault footwall, thickens to ~40cm in the immediate hangingwall of the fault and thins away from the fault to ~15 cm at the northern end of the trench. The gradational base of unit 8 is marked by a downward decrease in carbon content and an upward decrease in pebble content.

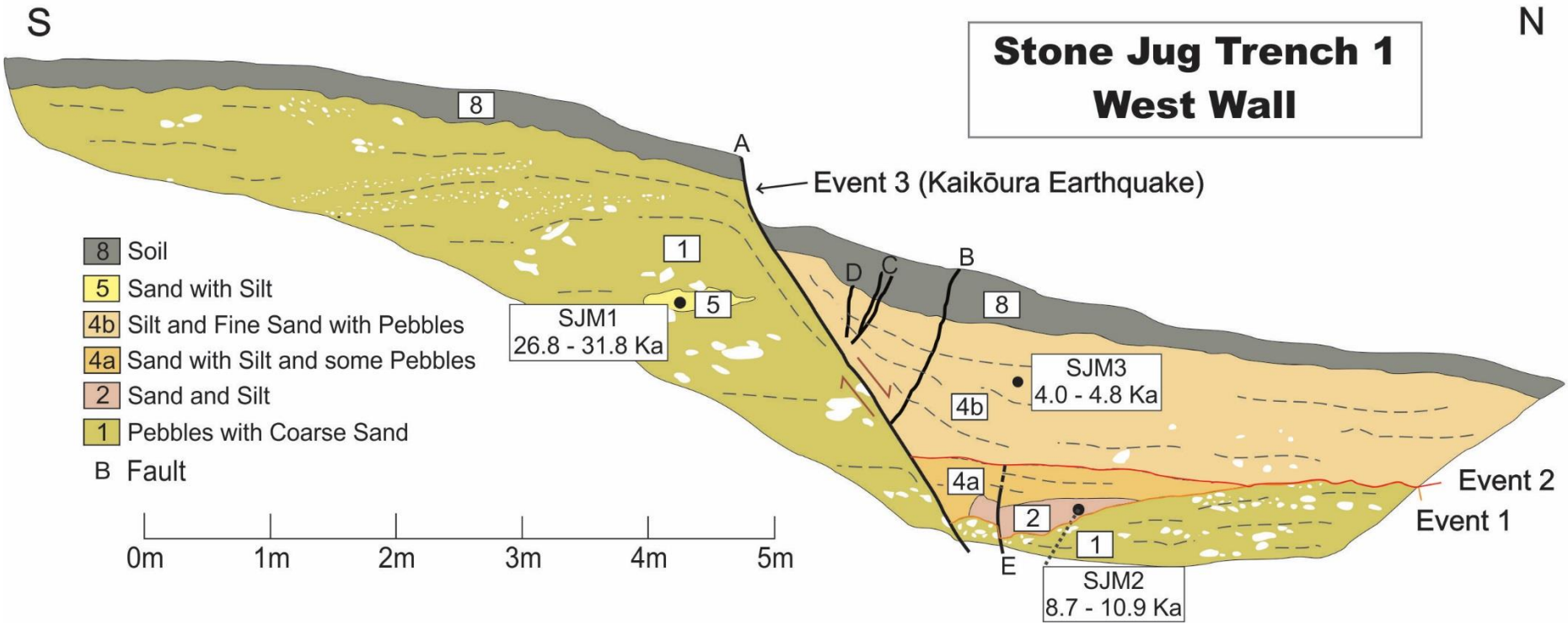

Fig 4.5: The western wall of SJT-1. The trench is located at the highest terraces the SJF crosses east of the Charwell. White resembles clasts that are significantly larger than the composition of that unit.

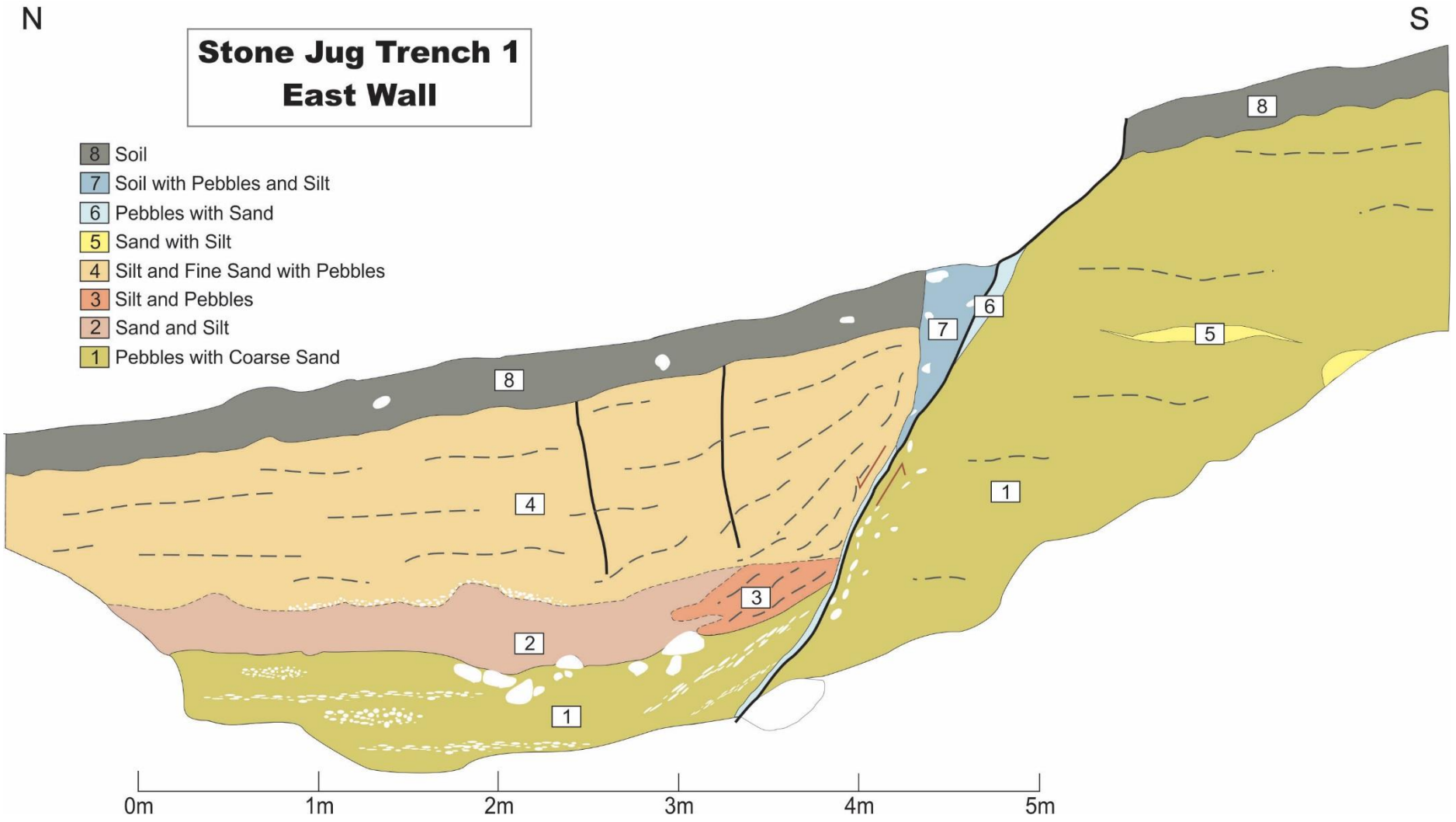

Fig 4.6: The eastern wall of SJT-1. This wall differs from the west due to the considerable width of the trench. The east contains a more continuous unit 2 and fissure infill structures.

4.3.2. Fault geometry and displacement

The fault zone was clearly observed on both walls of the trench (Figs. 4.5, 4.6). On the west wall, the fault comprises a main slip surface (fault A), which has a strike and average dip of 58° NNE. The fault in this wall steepens up to 78° at the ground surface. Four secondary faults (labelled flt B, C, D & E in Fig. 4.5) were observed in the hangingwall of the main fault and primarily dip steeply antithetic to the main fault. Fault E displaces the top of unit 1 and terminates within unit 2. On the east wall of the trench, the main fault surface varies in dip from 54° - 68°, again with multiple (two) antithetic minor faults in the hangingwall. These two fractures are sub-vertical, restricted to unit 4, up to 5mm wide (when dry) and appear to primarily accommodate extension (i.e. no vertical or lateral slip was observed). The upper ~80 cm of the fault zone comprises a wedge-shaped zone of mixed A horizon, silt, pebbles and cobbles. Inspection of post- Kaikōura aerial photographs suggest that unit 7 is a fissure fill formed in the 2016 earthquake. In addition, a thin sliver (<10 cm) of silt and A horizon is preserved along the fault. This sliver of fine material and the primary slip surface on the west wall are associated with rotation of the gravel clasts into parallelism with the fault slip direction. Clast rotation occurs up to 1m from the fault near the surface, but only 0.1m from the fault below 1 m depth.

Unit 1 can be correlated across the fault and the vertical displacement on the top of this unit is estimated to be 2.8±0.1 m. This measurement does not account for significant erosion of the footwall up to 3 m from the 2016 fault scarp (Fig. 4.5). Further minor erosion observed as surface rounding may occur up to 20m from the trench. Taking this immediate erosion (5m from the scarp) into account provides a total observed fault displacement post unit 1 of 3.5 m. Therefore, I propose a total vertical displacement of 3.5±0.5 m. Measurement of the 2016 earthquake scarp height in the trench walls suggests a displacement of the ground surface on the primary slip surface of 0.7±0.1 m, which is approximately one-fifth of the total displacement. These measurements are both minimum values as they do not take account of minor faulting or folding beyond the primary fault observed in the trench.

Tables of dates

Name	Trench Unit	Material Dated	C14 age	Calibrated Age Min*	Calibrated Age Max*
SJS2	10	Carbonaceous dark grey clay	3337 ± 18	3450	3590
SJS3	16	Soil	593 ± 17	520	560
SJS4	16 (within 10)	Entrained Soil	Not sent to lab	-	-
SJS4	16	Soil	Not sent to lab	-	-

Table 4.1: ^{14}C radio-carbon age dates. See Appendix 4 for full lab report.

**95.4% confidence*

Trench (unit)	Field Name	Laboratory number	Material Dated	Depth (M)	Water %	Total dose rate (GY/Ky)	Equivalent dose (Gy)	Optical age (ka)
2 (7)	SJS 1	WLL1368	Silt	1.1	17.9	3.82±0.33	76.84±0.42	20.1±1.8
1 (5)	SJ M1	WLL1269	Silt lens	1.3	20.0	3.81±0.33	111.49±0.57	29.3±2.5
1 (2)	SJ M2	WLL1370	Silt	1.65	37.3	3.25±0.35	31.96±0.25	9.8±1.1
1 (4b)	SJ M3	WLL1371	Silt	0.8	18.0	3.70±0.34	16.12±0.17	4.4±0.4

Table 4.2: OSL age dates and key processing values. See Appendix 3 for full lab report.

Figure 4.7: SJT-2 during initial analysis. The photograph was taken by Kate Pedley.

4.4. SJT-2 Observations

4.4.1. Unit descriptions

This trench encountered a number of stratigraphic units, none of which (except the soil A horizon – unit 16) could be confidently correlated across the fault. Unit 1 is the stratigraphically oldest unit exposed in this trench and was only present in the footwall of the fault (Figs 4.8 & 4.9). It consists of a blue clay with carbonaceous laminations containing coal fragments; this unit appears to be part of the bedrock sequence. Geological maps of the study area indicate that SJT-2 is underlain by the Late Cretaceous Bluff Sandstone member of the and Wallow Group (S. Crampton 1988; M. Rattenbury 2006), and we interpret unit 1 to be a mudstone-rich part of the Bluff Sandstone. Unit 1 has been sheared along the length of the fault in the north-western wall of the trench and has been displaced in an apparent reverse sense by two faults in the SE wall, where the uppermost part of bedrock is weathered to a light brown and contains granules of oxidised material (this weathered zone is referred to as unit 2).

In the SE wall units 1 and 2 are overlain by unit 4 a clay matrix supported layer with pebble-cobble sized clasts (mostly <10 cm diameter) of silt and fine sand derived from Torlesse basement. Unit 4 has also been mapped on the NW wall of the trench whether it is separated from bedrock by units 17-19. Unit 4 is weakly bedded to massive and in the SE wall is overlain

by a clast-supported cobble gravel (unit 6). Unit 6 terminates abruptly approaching the main fault in the SE wall of the trench, a termination that may be sedimentary or tectonic (see section 4.5 for further discussion). Unit 7 is a fine sand and silt with rare pebbles, many of which are oxidising. Unit 7 has been OSL dated at 20.1±1.8 ka (see Fig. 4.8, Table 4.2, sample SJS1 / WLL1368), however, the age of the trenched terrace surface is here estimated to be 6.3±0.5 kyr based on the down-cutting curve of Bull (1991) for the Charwell River and the 21 m height of the terrace above the active river bed. Given the Holocene age for the terrace surface, it seems likely that the age of the OSL was not reset during Holocene transportation and deposition. Units 8, 9, 20, 11, 12 & 13 are gravels with a silt dominated matrix and sub-angular to sub-rounded clasts of Torlesse sandstone. These units are distinguished by varying clast sizes, matrix composition and clast-matrix ratio. For example, unit 8 has more clasts which have slightly smaller sizes (unit 8 <15 mm vs 5-80 mm for unit 9) than unit 9.

In both trench walls unit 10 is triangular-shaped and defined by sharp boundaries. Unit 10 contains a mixture of lithologies including randomly aligned clasts 5 to 500 mm in diameter and fragments of paleosol within a silty clay matrix. There is no clear stratification in unit 10. A radiocarbon sample was collected from a 10x20 cm block of paleosol and returned a calibrated radiocarbon age of 3520 ± 70 years BP at a 95.4% confidence interval (Table 4.1, sample SJS3. The eastern margin of unit 10 is partly juxtaposed against unit 12 which is dominated by granule to fine pebble grain sizes (3 – 8mm diameters) and contains only sparse silt or sand matrix (i.e. is clast supported). Beds of coarser grain sizes (8 – 50 mm) were Imbricated and approximately 50 - 100 mm thick. The pea gravels are overlain by a silt matrix supported pebble unit, only observed at the very top of unit 12 and on the NE wall. Units 10 and 12 are overlain by unit 13 and the modern soil A horizon (unit 16). The soil A horizon had a high percentage of cobbles and is overthickened on the downthrown side of the fault. A sample for the basal 5 cm of the A horizon was also radiocarbon dated and returned an age of 540 ± 20 years old at a 95.4% confidence interval (Table 4.1, sample SJS3).

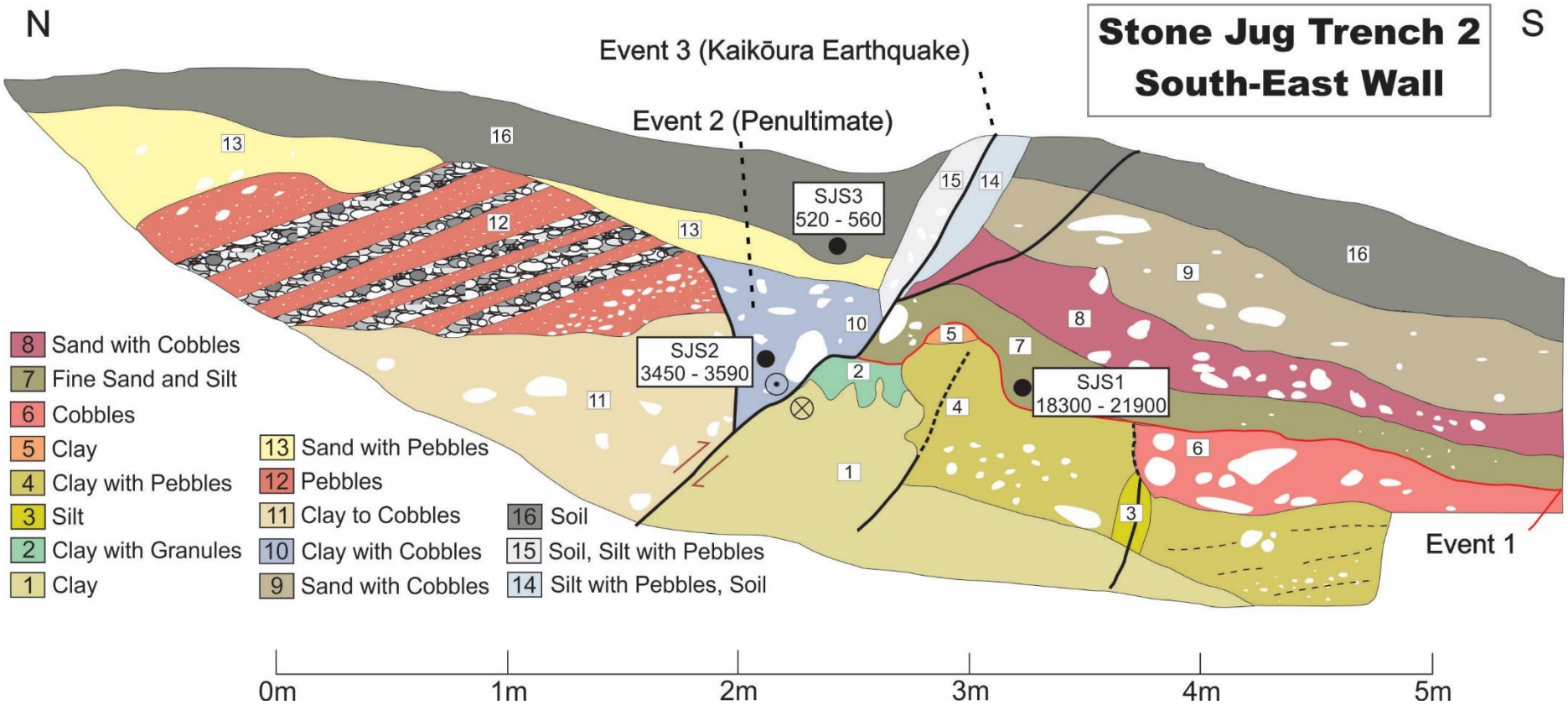

Fig 4.8: South-eastern wall of SJT-2. The black and white texture in unit 12 denotes coarser pea gravels with very little matrix (<5%).

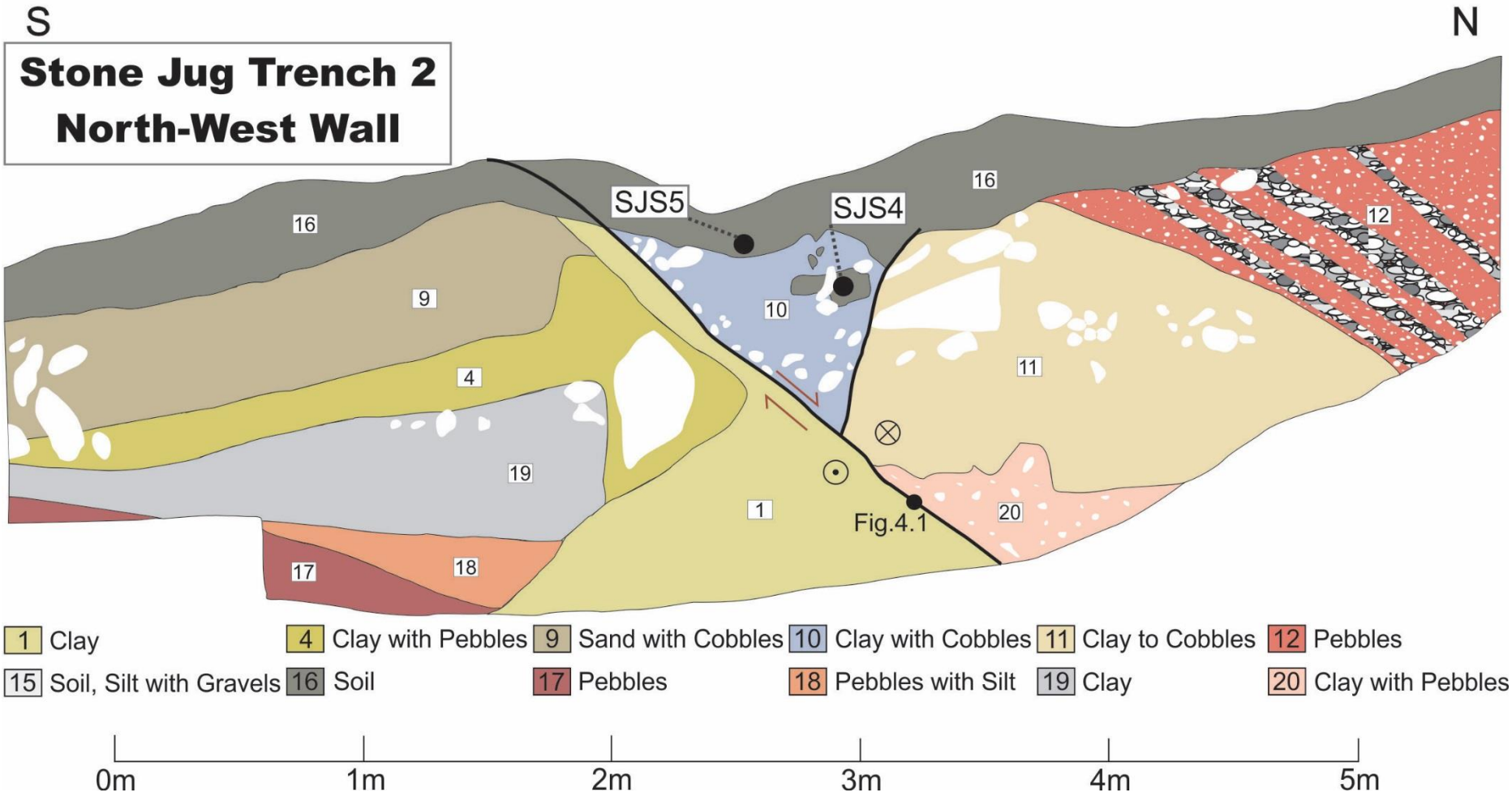

Fig 4.9: The north-western wall of SJT-2. When sampling RC-SJS4 the entire enclave was collected.

4.4.2. Fault geometry and displacement

The primary fault is confined to a narrow zone (<10 cm wide) that forms a predominantly linear trace with some steps often related to movement around large clasts. In the trench, this fault plane has an average strike of 310° and an average dip of 50° east (Fig. 4.1 & 4.8). In saturated clay-rich units (e.g., units 1, 11 and 20) the fault forms a fine dark gouge up to 20mm thick, as shown in figure 4.10. Within 1.5 m of the ground surface, the fault zone widens to form two wedges. The lower-most wedge contains unit 10, a stratigraphically mixed unit, while units 14 and 15 are contained within the upper wedge that is up to 30 cm wide. Inspection of aerial photos and the trench walls suggests that this upper wedge is a fissure infill from the 2016 earthquake. Three secondary faults were mapped in the footwall of the main fault in the SW wall. The uppermost of these faults splays from the main trace at a depth of 0.6 m. Two additional faults were present in the lower-most metre of the trench on the SW wall, where they displace the top basement and extend through unit 4. The total width of the fault zone in the SW wall is approximately 2 m.

The trench provides constraints on the apparent vertical displacement on the fault. Bluff sandstone bedrock is only located in the footwall of the fault in trench SJT-2 (Fig. 4.8). To locate bedrock on the downthrown side of the fault we excavated a pit to a depth of ~4 m about 5 m SE of the trench. This pit encountered only gravels and failed to locate the bedrock, from which we conclude that the apparent vertical displacement on the fault is >~3.5 m. This apparent displacement on the top-bedrock unconformity is significantly larger than the <1 m apparent cumulative displacement during Events 4 and 5 at this site. If our observations are correct, they suggest that Event 3 produced in excess of 2.5 m, significantly larger than vertical displacements for any of the events recorded in the two trenches. More data are required to confirm the Event 3 vertical displacement in SJT-2. Higher in SJT-1, formation of the colluvial wedge filled by unit 10 was associated with apparent vertical displacement of 0.5±0.1 m, while the 2016 earthquake appears to have produced a ~0.1 m. These measurements suggest that in the SJT-2 trench vertical displacements were not similar.

Figure 4.10: Thin linear fault gouge in clay at SJT-2 between units 1 and 20 on the north wall. The photo was taken near the bottom of the trench were the gouge is darker, firmer and lacks fabric. Photograph taken by Kate Pedley.

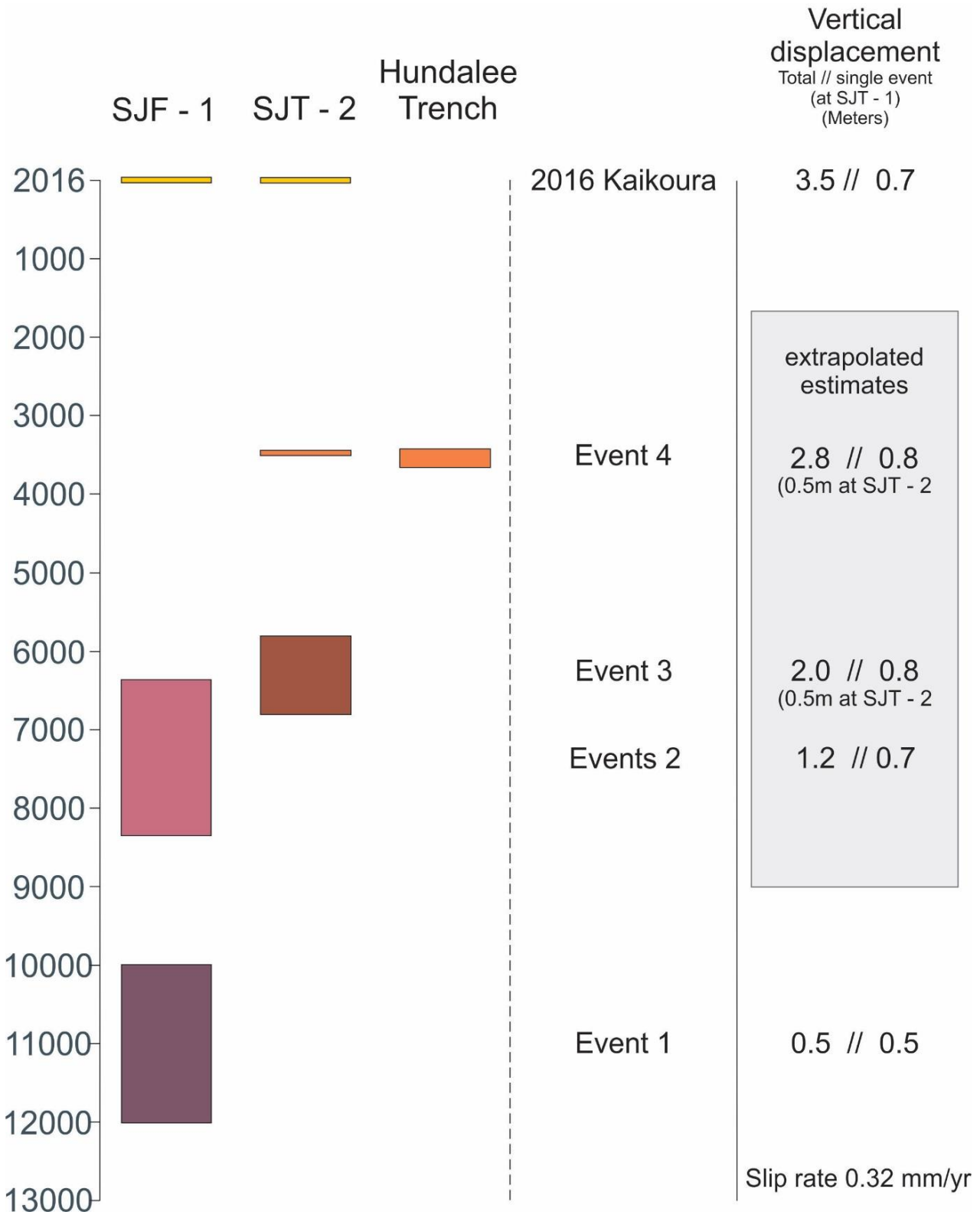

Figure 4.11: Rupture history of the SJF as observed across two trenches. Age ranges for events 3, 4 and 5 are most likely age ranges, not plausible age ranges which are significantly larger and outlined below.

4.5. Paleoseismic history

Interpretation of the stratigraphy and faulting in SJT-1 places constraints on the paleoearthquake history of the SJF during the early Holocene (e.g., post 12 kyr). The trench shows evidence for two paleoearthquakes (in addition to the 2016 event). The oldest event (Event 1) is indicated by unit 3 which is interpreted to be a colluvial wedge derived from a fault scarp generated during a paleoearthquake on the SJF. This wedge rests on unit 1 and was deposited synchronously with unit 2 which is here OSL dated at 9.8±1.1 ka (Table 4.2, sample WLL1370). Therefore, Event 1 ruptured the ground surface prior to deposition of OSL sample WLL1370 and after deposition of the gravels at the bottom of the trench and the paleo Charwell River abandoned the terrace surface. This surface was abandoned at 11±1 ka (1σ) and we suggest that Event 1 most likely occurred between 12 and 10 ka, although could be as old at 13 ka and as young as ~9 Ka. This event may have produced the local depression into which unit 2 was deposited, however, it is also possible that this depression was formed by channelization of the terrace surface prior to its abandonment. Unit 4 is interpreted to form a second colluvial wedge produced by erosion of the fault scarp which was regenerated multiple times during the Holocene. The earliest of these earthquakes (Event 2) is interpreted to have occurred at the boundary between units 2 and 4, and to have triggered the onset of deposition of units 4 and 4b (unit 4a may have formed due to erosion of the scarp generated by Event 1). This event may also have produced fault E, which displaces unit 2 on the west wall of the trench, but does not appear to have displaced the base of unit 4b. There are no OSL samples that directly date the unit 2-4 and 4a-4b contacts. Using the OSL dates of 9.8±1.1 ka in unit 2 and 4.4±0.4 ka in unit 4b (Fig. 4.5) and assuming a uniform sedimentation rate 0.19 mm/yr between the two samples, I infer an age for the 4a-4b contact of approximately 7-5 ka. This age range is assumed to approximately date Event 2. The thickness of the unit 4/4b colluvial wedge and the rarity of large cobbles within the wedge suggest that it most likely formed in multiple small events (e.g., vertical displacement < 1 m). If the wedged formed due to a single large displacement event (e.g., ~2 m throw), the fault scrap would have exposed unit 1 and subsequent erosion of the scarp (which is not observed) would have supplied many large cobbles to the wedge (again which is not observed). The inference that multiple events produced the large colluvial wedge (unit 4) in SJT-1 cannot be substantiated by the available stratigraphy and detailed OSL

dating of the large colluvial wedge was not attempted. The timing of events younger than ~7 ka are inferred from observations in SJT-2 (see the following paragraph).

The SJT-2 trench is thought to record surface ruptures on the fault post 6.3±0.5 kyr BP, the age of this degradation surface estimated by Bull (1991). Interpretation of the trench logs for each wall of the trench is consistent with two paleoseismic events during the mid to late Holocene in addition to the 2016 event. The oldest of these events, which here is referred to as Event 3, is inferred from the secondary faults in the footwall of the primary fault (Fig. 4.8). These faults are interpreted to displace the top of bedrock and the lowermost parts of unit 4 but do not appear to displace unit 7 (Fig. 4.8). I infer that the gravel units in the trench walls were primarily deposited by the Charwell River when it was at, or close to (e.g., within 5m), the altitude of the trenched terrace surface. This inference is supported by the radiocarbon date of 3520±70 cal. yrs BP (Table 4.1, sample SJS2) from unit 10 which post-dates gravel units 11, 12 and 20 and abandonment of the terrace surface by the river. If this argument is correct, then Event 3 dates from near the time of terrace formation at 6.3±0.5 kyr BP. A second younger paleoearthquake is recorded in the SJT-2 trench by unit 10, which comprises chaotic and mixed material and is interpreted to be fault-bound fissure fill. Analysis of 2016 surface ruptures suggests that fissure fill deposits are common and form within two years of the earthquake (as was the case of units 14 and 15 in this trench). Therefore, soil A horizon material that is incorporated into the fissure fill represented by unit 10 provides a means of dating the cessation of soil development and the formation of the fissure. Given that this fissure is located within the fault zone, I suggest that it formed during a surface-rupturing earthquake. This earthquake is here referred to as Event 4 and has been radiocarbon dated at 3520±70 cal. yrs BP (Table 4.1, sample SJS2). This earthquake produced a structural depression along the fault within which the soil A horizon is thickened (compared to the upthrown side of the fault). The last and final earthquake on the SJF occurred in 2016 and here is referred to as Event 5.

Based on the interpretations in the previous paragraphs, five surface-rupturing earthquakes occurred at; 11,000±1000, 7500±1000, 6500±1000, 3500±100 and 3 (2016 Kaikōura Earthquake) years BP. Given errors on the 7500 and 6500 years BP events and the fact they were observed at separate sites, a four-event history for the last ~11ka is possible. The timing of these events produces recurrence intervals that range up to 5000 years and an average recurrence interval of

2750 yrs. Based on the event timings and average recurrence intervals the RI of the penultimate event (i.e. ~3500 yrs) was longer than the 2750 yrs average RI for the entire dataset. It seems that the SJF was well advanced in its seismic cycle at the time of the Kaikōura Earthquake.

Given the paucity of stratigraphic units that can be traced across the faults exposed in the trenches, reliable SEDs are difficult to determine for paleoearthquakes on the fault. It is however possible to calculate an average SED for paleoseismic events in trench SJT-1 using a total vertical displacement of 3.5±0.5 and assuming that this displacement accumulated in five events. For such a model the average SED would be 0.7±0.1 m, which is equal to the 0.7±0.1 m of the 2016 vertical displacement. The similarity of these SED values may suggest that 'typical' events on the SJF produce sub-metre displacements and provide little evidence for the 2016 event being significantly different from previous surface rupturing events on the SJF. A sub-metre SED on the SJF supported by the large colluvial wedge in SJT-1 which I infer was produced by the combined displacements of Events 2, 3 and 4. This wedge mostly comprises pebble-sized clasts and silt which are inferred to have mainly been eroded from the active soil profile following each earthquake, rather than being sourced primarily from unit 1 which is cobble rich.

Slip rates for the SJF can be calculated for the SFT-1 displacement and age data. Using a total vertical displacement of 3.5±0.5 m and an age of 11±1 kyr for the base of the cover beds on the Stone Jug terrace surface, I calculate a vertical displacement rate of 0.32±0.8 mm/yr. I infer that these displacement rates also apply to the Northern section of the fault where it is left-lateral. It is presently unclear whether these Holocene rates are representative of the entire SJF. The absence of a clear mappable fault scarp along the Central and Southern sections of the fault, suggests that the landscape surfaces in these sections are young (e.g., late Holocene) and/or that the displacement rates on these faults are comparable to, or lower than, the ~0.2-0.4 mm/yr at the northern end of the fault.

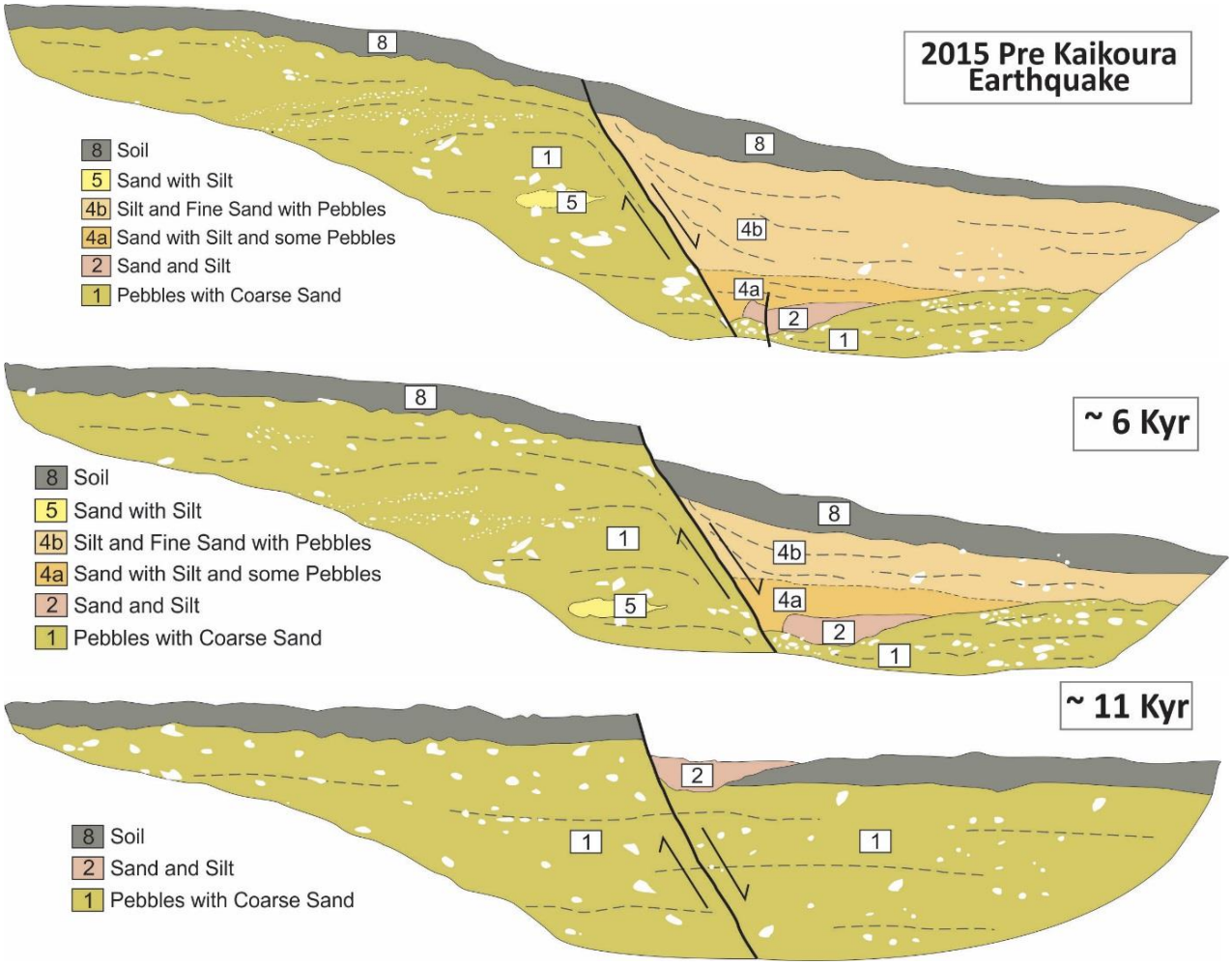

Fig 4.12: This figure schematically shows the evolution of the SJT-1 west wall from the abandonment of the ~11ka surface. Retro-deformation has been achieved by progressively back-slipping the fault, removing sediment deposited in the colluvial wedge and adding sediment eroded from the fault footwall. The figure aids visualisation of how the modern SJT-1 formed over multiple seismic events.

4.6. Discussion

4.6.1. Assumptions and limitations

The results of all trenching studies are constrained by the temporal resolution of the stratigraphy excavated, the ability to date the stratigraphy and correlate it across the fault zone, and by the location (and number) of trenches (McCalpin, 2009). The temporary window of observation in this study is estimated to be ~11±1 kyr, with SJT-1 providing paleoseismic data for the Early Holocene and SJT-2 the Middle and Late Holocene. The timing of the events identified in

the trench log are subject to some uncertainty which is several thousand years for events 1-3. These uncertainties may be reduced by using OxCal, software that employs the means and standard deviations of dates that constrain the timing of paleoearthquakes to calculate the most likely age ranges of the earthquakes (Bronk Ramsey 1995). I have not used OxCal in this thesis, in part because the OSL dates were only made available two weeks before thesis submission. OxCal analysis will be conducted post-thesis examination to help improve the age estimates of the paleoearthquakes for the purposes of publication.

Trenches typically provide information for a single point along a surface trace and on a fault surface that may extend through the brittle crust (McCalpin, 2009; Biasi and Weldon, 2006; Wesnousky, 2008; Nicol et al., 2016). Therefore, when locating trenches consideration should be given to how representative the results from the trench will be of the entire fault. Trench sites in this thesis were excavated within 500m (Fig. 4.1) of each other on the Northern section of the fault. This section of the fault was mapped prior to the earthquake with a scarp height up to 5 m, whereas aerial ortho-photographs pre-dating 2016 displayed no fault scarps on the Central and Southern sections of the fault. Given the northward increase in scarp height, it is possible that the northern end of the SJF is more active than the Central and Southern sections. If this is the case, then the trenching results from this study may not be representative of the entire fault.

The trench logs presented here are both <10 m long and primarily provide timing and displacement near (<5 m) the primary slip surface. However, poorly consolidated gravels, such as those found in the SJT-1, are prone to distributed deformation (Hornblow et al. 2014). While significant distributed deformation was not identified as part of this study, all displacement measurements and calculated displacement rates should be considered minimums.

4.6.2. Long-term displacement rates and recurrence intervals

Information on individual earthquakes is not available prior to ~11 kyr, however, displacement of bedrock strata permit the calculation of long-term (e.g., ~ million year) average displacement rates and earthquake recurrence intervals. The data and assumptions underpinning these calculations carry significant uncertainty and the resulting conclusions are considered tentative. Mapping of the Northern SJF and Monkey Face area was conducted by James Crampton in the 1980s (Crampton, 1988). When georeferenced and combined with Kaikōura surface ruptures along

the SJF, Crampton's mapping suggests an approximate 270±50 m apparent left-lateral displacement of the Torlesse-Bluff Sandstone contact on the Northern SJF (Figure 4.13). This contact dips steeply at approximately 60° to the NW and any vertical displacement down to the SW (the predominant down throw direction in the Holocene) would produce apparent left-lateral strike-slip. Therefore, the apparent left-lateral displacement is exaggerated by vertical displacement. The steep contact angle and strike-slip dominated motion of this segment minimise the effect of vertical long-term displacement of the contact. Assuming that displacement of bedrock was purely left lateral and that present activity on the fault started at 1±0.2 Ma, as suggested for other structures in North Canterbury and immediately offshore (Nicol et al., 1994; Barnes, 1996; Vanderleest et al., 2017), I calculate an average displacement rate of 0.3 ±0.1 mm/year on the SJF. This rate is consistent with the estimated rate for the Holocene and suggests that earthquake activity recorded in the trenches could be representative of the million-year timescale earthquake activity on the fault. For example, using a displacement rate of 0.3 ±0.1 mm/year and a SED of 0.7±0.1 m, the average long-term recurrence interval would be 2.6±0.5 kyr which, within the uncertainties, is comparable to the record post ~11 kyr.

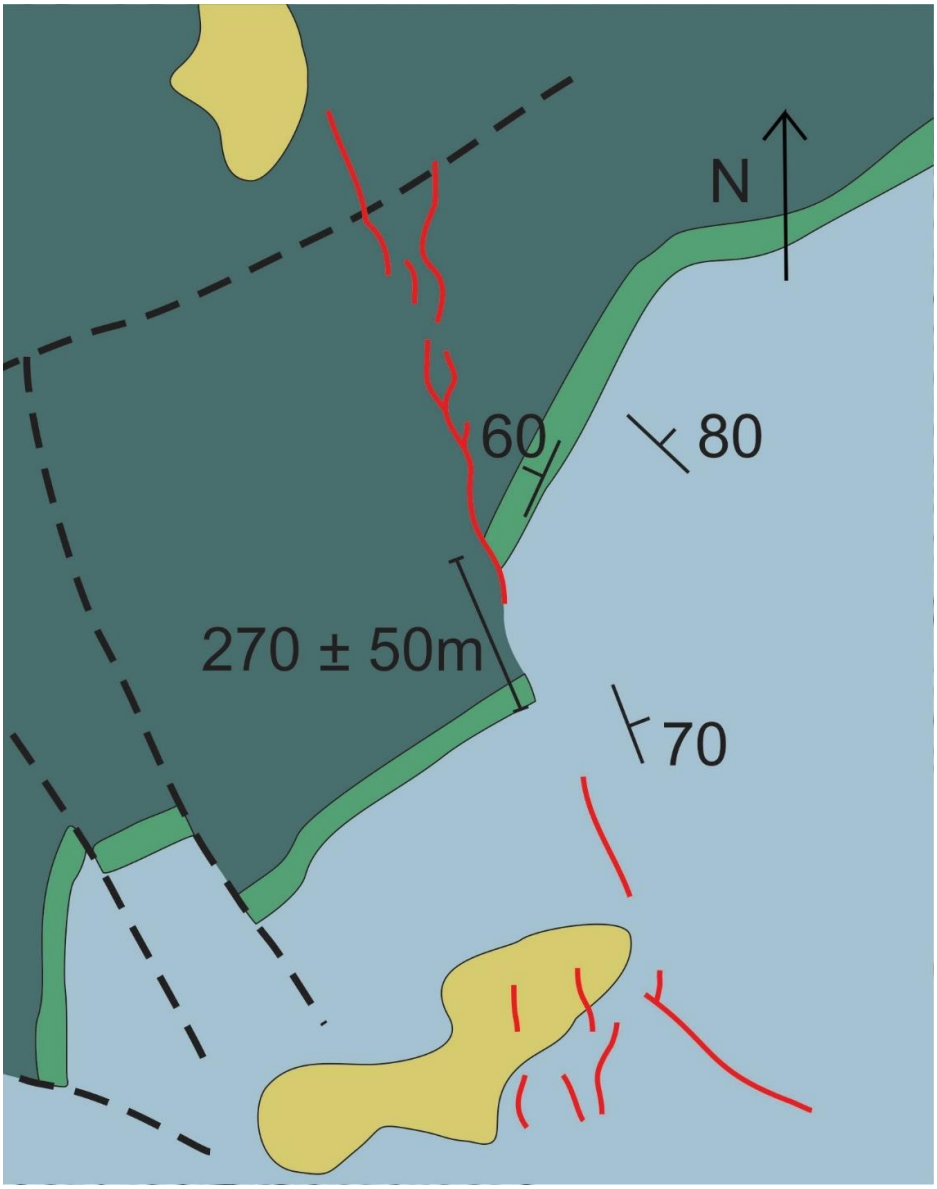

Figure 4.13: Total displacement on the SJF observed by Crampton (1988) at the Bluff Sandstone - Torlesse boundary. The SJF is in red; Yellow is Quaternary deposits; light grey is Torlesse; Green is the Bluff Sandstone Member conglomerate lithofacies and the dark turquoise is Bluff Sandstone Member sandstone lithofacies.

4.6.3. Relations of the SJF to other faults

The Kaikōura Earthquake demonstrated that the SJF is kinematically related to the Hundalee, Conway-Charwell and Leader faults, with all of these faults moving together and interacting. The SJF may repeatedly rupture synchronously with neighbouring faults such as the Humps, Conway-Charwell, Hope and Hundalee faults. It is possible, for example, that Hope Fault events occasionally

trigger slip on the Northern section of the SJF, and that this triggering contributed to the prominence of the pre-2016 fault scarp at the Northern section of the fault (compared to apparent absence of pre-2016 scarps on the Central and Southern sections of the SJF). It is also possible that destressing of the crust adjacent to the Hope Fault arising from a large magnitude earthquake several hundred years ago, contributed to the northward decrease in slip on the SJF during the 2016 event. The Hope fault has a recurrence interval of several hundred years for surface-rupturing events (Langridge 2003, Khajavi et al. 2016, Khajavi et al. 2018), which is an order of magnitude less than the SJF. Therefore, on average, no more than every 10th Hope Fault earthquake results in geologically observable surface rupture of the SJF.

Trenching of the Hundalee Fault recently dated the penultimate Hundalee event to be younger than 3633 years BP (Barrell et al., 2018). This timing is consistent with the age of the penultimate event observed on the SJF suggesting that it is possible that these penultimate events occurred synchronously. Trenching of other faults in the North Canterbury region, including the Humps and Conway-Charwell, suggests that these structures may also have accommodated surface rupturing earthquakes between 1000 and 5000 yr BP (Brough, 2019; Nicol pers. comm, 2019). Therefore, it remains possible that the faults that ruptured in the 2016 event also ruptured together in a single earthquake about 3500 yrs BP. Although more analysis is required to test the temporal links between earthquakes and these faults, at this time I cannot discount the possibility of a Kaikōura type Earthquake at ~3500 yrs BP. If this is the case these events could occur more frequently than the >6000 yrs proposed in publications to date (Litchfield et al., 2018; Nicol et al., 2018).

4.7. Conclusions

Two trenches were excavated across the SJF (SJT-1 and SJT-2) approximately 500 m apart on the Northern section of the fault where it crosses a flight of river terraces formed by the Charwell River. These trenches revealed mainly Holocene stratigraphy displaced by the fault and dated using radiocarbon (N=2) and OSL (N=4) samples. Analysis of the trench data interprets five surface-rupturing paleoearthquakes with likely vertical displacements of <1 m. These events are interpreted to have occurred at the following times: 11,000±1000, 7500±1000, 6500±1000,

3500±100 and 3 (2016 Kaikōura Earthquake) years BP. The timing of these events produces recurrence intervals that range up to 5500 years and an average recurrence interval of 2750 yrs. Comparison of these results from this thesis to unpublished trench data suggests synchronous rupture of the Hundalee, Stone Jug, Conway-Charwell, and Humps faults about 3500 years ago cannot be discounted. Estimated slip rates for the fault since ~11 ka are 0.2-0.4 mm/yr. These rates are comparable to the 0.2-0.4 mm/yr million-year rates inferred from the apparent left-lateral displacement of steeply inclined Cretaceous beds.

Chapter Five: Discussion and Conclusion

5.1. Chapter Conclusions

This thesis focuses on the Stone Jug Fault which ruptured during the 2016 Kaikōura Earthquake. It comprises three main chapters that examine the geometry and kinematics (Chapter 2), the influence of Torlesse basement on fault geometry (Chapter 3) and the paleoseismic history of surface-rupturing earthquakes on the fault (Chapter 4).

Chapter two showed that the SJF is ~19 km long and appears to terminate against the Conway-Charwell and Hundalee faults at its northern and southern ends, respectively. The fault has a roughly sigmodal shape, striking N-S in its Central section and NW approaching each fault tip. The primary slip surface is associated with many (N= 48) secondary faults, which are particularly common near irregularities on the fault surface and near the southern tip. On average the fault displays oblique slip and accommodates approximately equal components of left-lateral and reverse displacement. Locally the orientation of the trace determines the relative values of strike-slip and dip-slip movement. Displacement profiles show two displacement peaks separated by a low that may be due to off fault accommodation of displacement, either through distributed deformation or a blind structure. Analysis of fault kinematics supports the view that he SJF accommodates displacement transfer between the Hundalee and Conway-Charwell faults. However, in previous events it is also possible that the SJF interacted with the Hope and Oaro River faults.

Chapter 3 shows that for most of its length the SJF is contained within Torlesse basement rocks. This demonstrates that there is a strong correlation between the general strike of the SJF and of regional bedding in Torlesse basement. These data suggest that the orientation of the fault surface is at least partly controlled by the basement fabric. Although the bedding surfaces appear to be misaligned for slip in the contemporary stress regime, they may accommodate slip because they represent zones of weakness that are exploited by the active faulting.

Chapter 4 provides a paleoseismic history for the SJF over of the last ~11 ka. Five events were interpreted in two trenches excavated into the eastern Charwell River terraces. Over this time the SJF likely mainly experienced surface-rupturing events with single-event-displacements of <1 m

and an average recurrence interval of approximately 2750 years. Typical event displacement is expected to be similar to Kaikōura except for the northern half of the Northern section of the fault, which displayed anonymously low displacements inconsistent with pre-existing scarp heights during Kaikōura. The Stone Jug Fault has a low activity rate approximately 0.3 mm/yr. Previous events have approximate inferred dates of 11,000±1000, 7500±1000, 6500±1000, 3500±100 and 3 years BP. The penultimate event on the SJF was ~3500 years ago and consistent with the timing of surface-rupturing earthquakes on the Hundalee, Conway-Charwell, Humps and Leader faults. Therefore, it remains possible that all of these faults ruptured together in a single large-magnitude event.

5.2. Was Kaikōura a typical event for the SJF

Several faults that ruptured in the 2016 Kaikōura Earthquake experienced atypical kinematics (Duke et al., 2018; Kearse et al., 2018; Williams et al., 2018), and questions arise as to whether slip on the SJF in 2016 was also 'atypical' of previous surface-rupturing earthquakes. Trenching appears to suggest that the displacement sense and magnitude on the southern end of the Northern section of the SJF were consistent with previous Holocene events. South of the trench sites left-lateral displacement of the Bluff Sandstone and Torlesse unconformity, also suggest that the slip and recurrence intervals during the Holocene could be representative of the long-term fault behaviour. This offset contact provided an approximate activity for the SJF, as calculated from an age for regional seismic activation and total displacement seen at the site. Vertical displacements of <0.25 m in 2016 on the trace west of the Charwell River appears to be inconsistent with scarp heights of up to 5 m on the Stone Jug terrace, as it would require recurrence intervals of <650 years. These recurrence intervals are inconsistent with the results from trenching and are considered unlikely. Taken collectively these data suggest that not all surface-rupturing events on the SJF exhibit the rapid decreases in displacement northwards along the northern section of the fault observed in 2016. Instead, I speculate that some events on the SJF have relatively high displacements (e.g., 1-2 m) on the northern section of the fault which are uniform or diminish southwards along the trace. Such events may be triggered by, or occur co-seismically, with events on the Hope Fault.

5.3. The SJF interaction with nearby faults

The Kaikōura Earthquake demonstrates that the faults in the NCD are capable of interacting kinematically during large-magnitude earthquakes. The faults that interacted in 2016 all appear to have been hard-linked (i.e. intersected each other), with displacement transfer between faults being facilitated by secondary faults in the intersection zone. A key question arising from the Kaikōura Earthquake is how common are these multi-fault ruptures in the geological record? Addressing this question is important for understanding earthquake processes and improving seismic hazard estimates. For example, if multi-fault ruptures are common, then the number of events in some fault systems may be over-estimated, while the maximum magnitudes of these events may be underestimated. Currently there are insufficient data to test the importance of multi-fault ruptures. However, we can say that the trenching results so far do not permit us to preclude the possibility that many of the faults that ruptured in 2016 also accrued slip at the ground surface about 3500 years ago. Even if these NCD faults ruptured in the late Holocene, it remains possible that Kaikōura type ruptures (i.e. that rupture all the faults that accrued slip in 2016) occur 6 kyr timescales or longer (Litchfield et al., 2018; Nicol et al., 2018).

5.4. Further research opportunities

Due to the limited time (12 months) and resources available for a master's thesis, a range of scientific research and data analysis were not explored in this study. Additionally, learnings from this study have raised further research questions that could build on this work. These are briefly listed below:

1) To date, no paleoseismic data is available on the Central and Southern sections of the SJF. Consequently, the trench data presented in this thesis represent a point sample on a fault trace and it remains somewhat unclear how representative our trenching results are for the fault as a whole. In addition to testing the results of this study trenching on the Central and Southern SJF would provide a basis for estimating how typical the 2016 event was of earthquake activity on the fault.

2) Due to the very late arrival of the trenching OSL samples, it was not possible to perform detailed analysis of the dates and the timing of paleoearthquakes from the trench data. Augmenting the present analysis using OxCal (Bronk Ramsey 1995) to analyse groups of paleoseismic events has the potential to provide more detailed insights into the most likely timing of paleoseismic events and will be performed before the current work is published.
3) In addition to the SJF trenches a further six trenches have been excavated across NCD faults that ruptured in 2016. Although beyond the scope of this thesis, it is clear that a detailed comparison of the paleoearthquake histories of these faults will be essential. This comparison will help better constrain the possibility of prehistoric multi-fault ruptures in the NCD. It will also have value for seismic hazard analysis and for improved understanding of regional tectonics.
4) The preliminary analysis of the orientations of the SJF and Torlesse bedding highlight the potential role of this bedding in the locations and orientations of faults. Approximately N-S faulting and Torlesse bedding are observed throughout much of the northeastern South Island and it is possible that the relations described for the SJF apply widely. Further detailed work is required to test the regional impact of Torlesse fabric on faulting.
5) While the Humps (Brough, 2019), Leader (Bushell, PhD in progress) Conway-Charwell (Nicol et al., 2018), Stone Jug (this study) and Hundalee (Williams et al., 2018) fault have been studied in variable depth, little work has been conducted on the Oaro River and Whites faults. Both faults have a northerly strike and may also reactivate basement heterogeneities. The SJF, Oaro River and Whites faults may also exhibit similar kinematics and suggest that left-lateral may be distributed over a wider area than just the SJF. Further research on the Oaro and Whites faults provide an opportunity to further understand fault kinematics of faulting in the northern South Island.

Appendix 1 - Collection of photographs depicting field work

This appendix contains a range of photographs to provide context and clarity to the field conditions, methods, and to illustrate the SJF surface rupture. Apart from most trenching photographs, which were taken by Kate Pedley, a mobile phone camera was used for the images in this appendix. All photos are georeferenced by page and number on the following map.

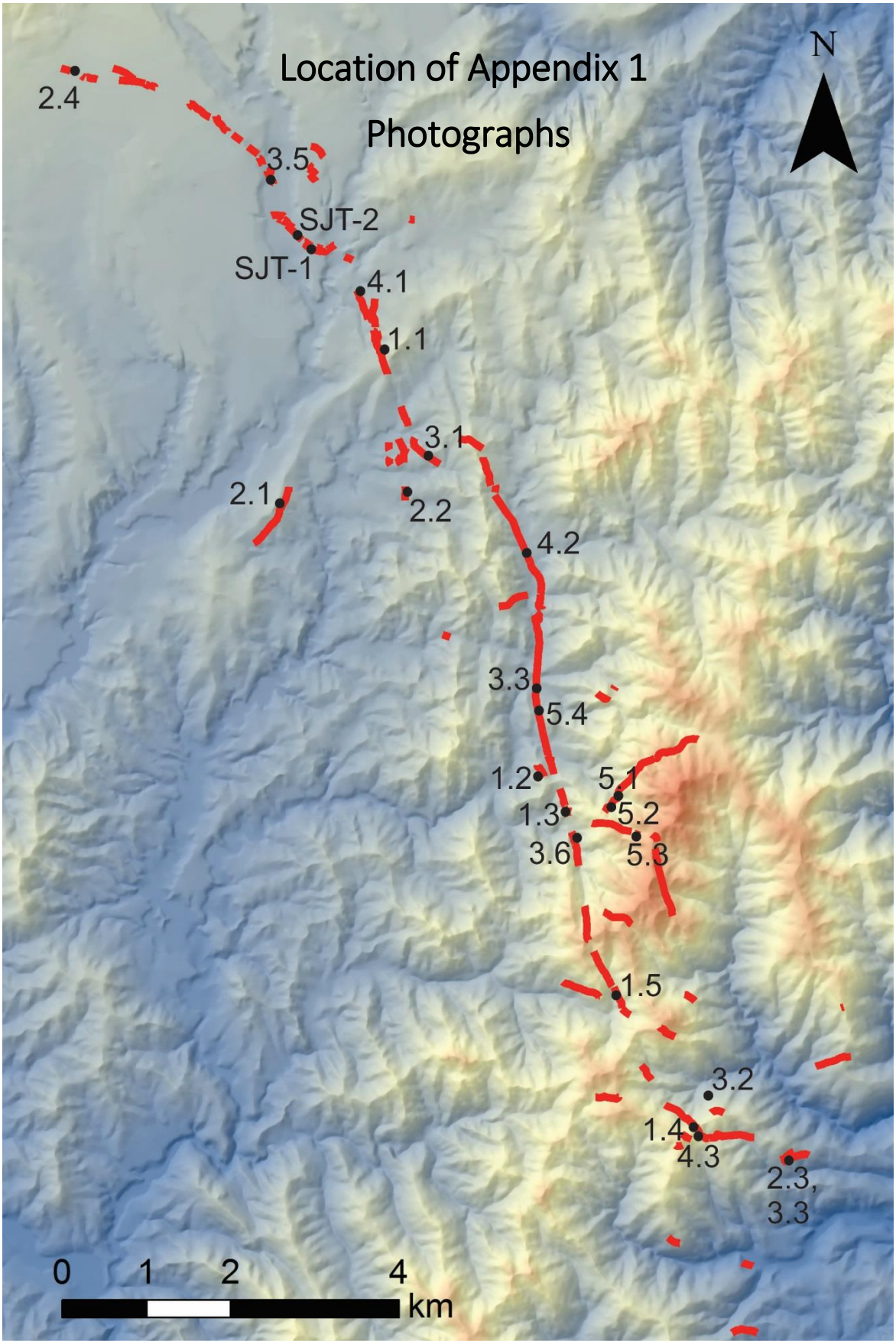
Location of Appendix 1
Photographs
N
2.4
3.5
SJT-2
SJT-1
4.1
1.1
3.1
2.1
2.2
4.2
3.3
5.4
1.2
5.1
1.3
5.2
3.6
5.3
1.5
3.2
1.4
4.3
2.3,
3.3
0
1
2
4
km

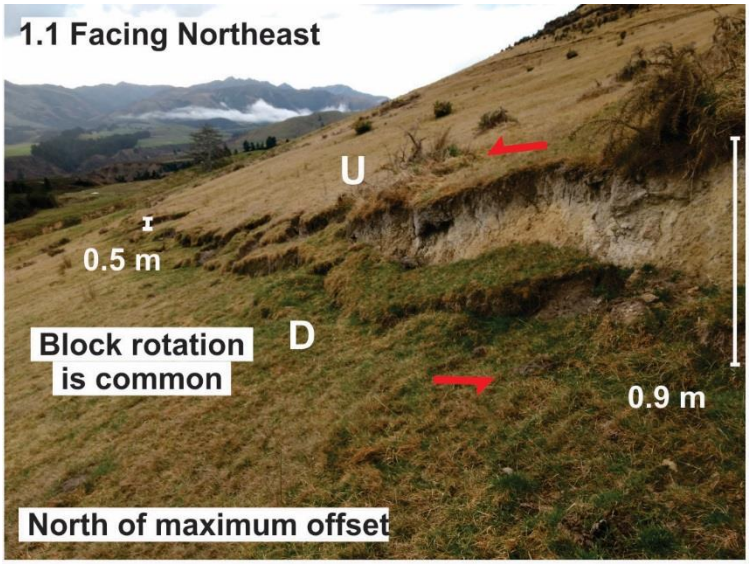
1.1 Facing Northeast
U
0.5 m
Block rotation
is common
D
0.9 m
North of maximum offset

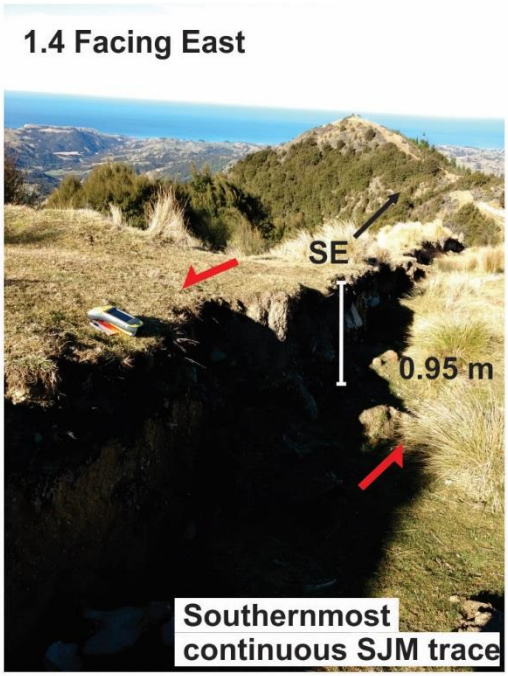
1.4 Facing East
SE
0.95 m
Southernmost
continuous SJM trace

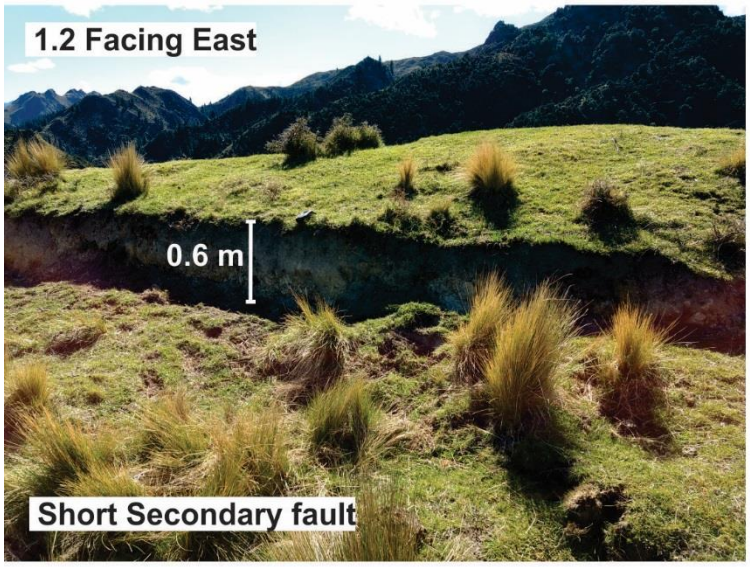
1.2 Facing East
0.6 m
Short Secondary fault


1.5 Facing South
Anomalous SJF trace
0.55m
D
U

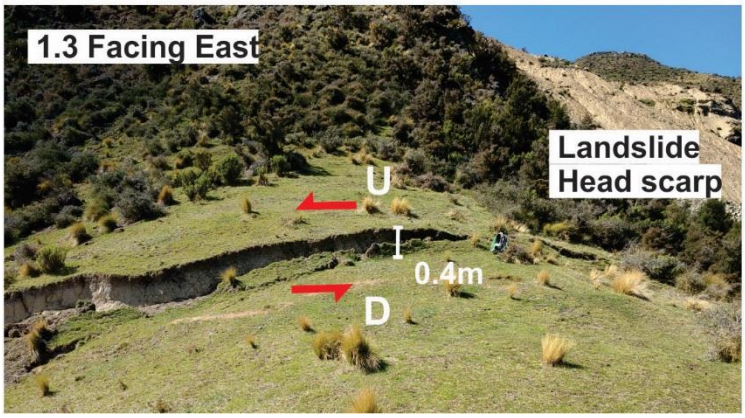
1.3 Facing East
Landslide
Head scarp
U
0.4m
D


2.1 Facing NE
Pre-existing swamp
U
D
Large secondary fault
West of central section

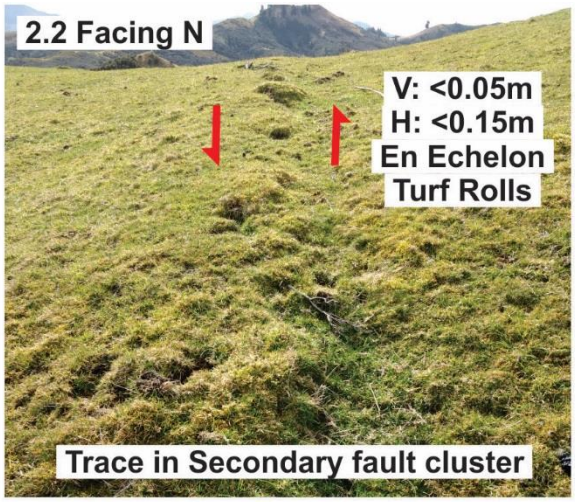
2.2 Facing N
V: <0.05m
H: <0.15m
En Echelon
Turf Rolls
Trace in Secondary fault cluster

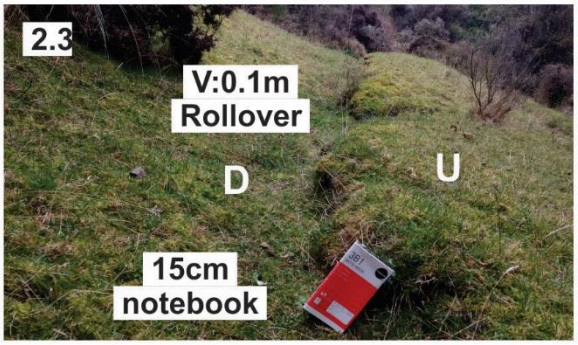
2.3
V:0.1m
Rollover
D
U
15cm
notebook

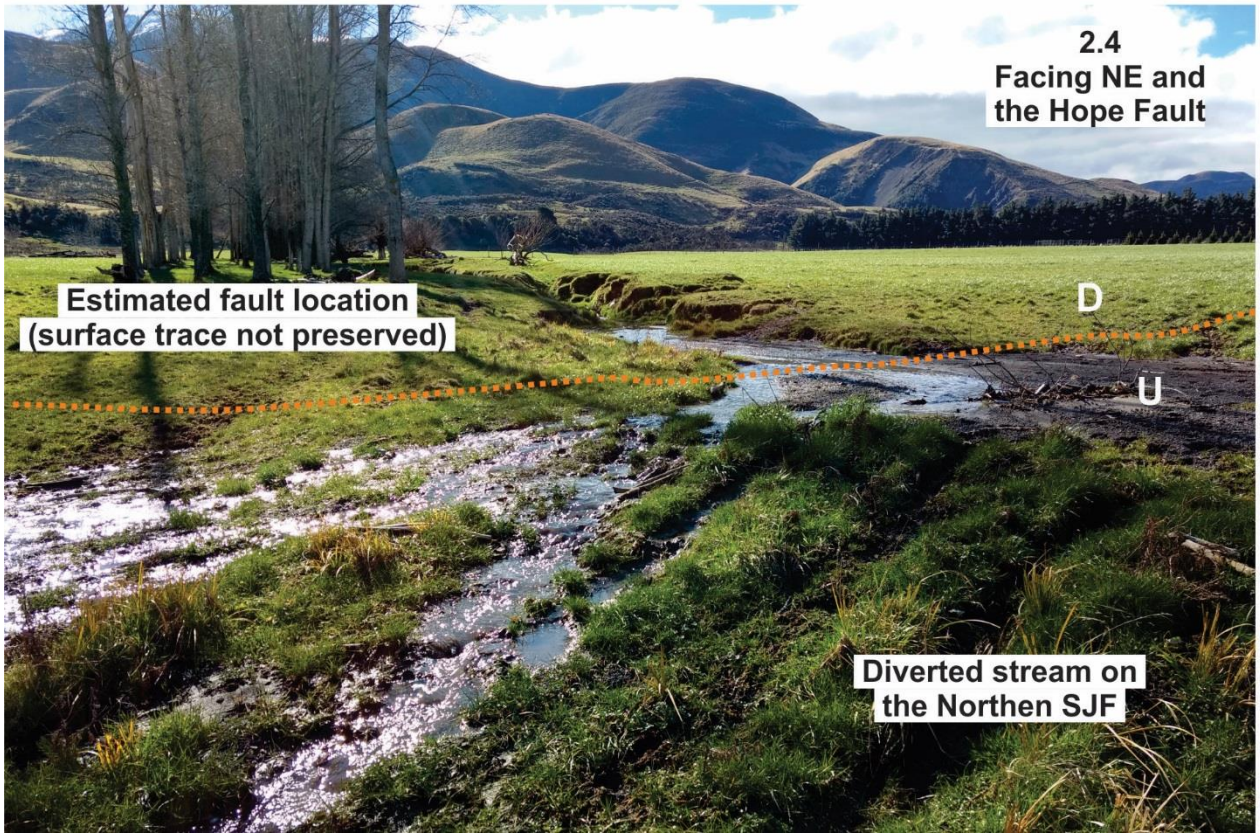
2.4
Facing NE and
the Hope Fault
Estimated fault location
(surface trace not preserved)
D
U
Diverted stream on
the Northen SJF

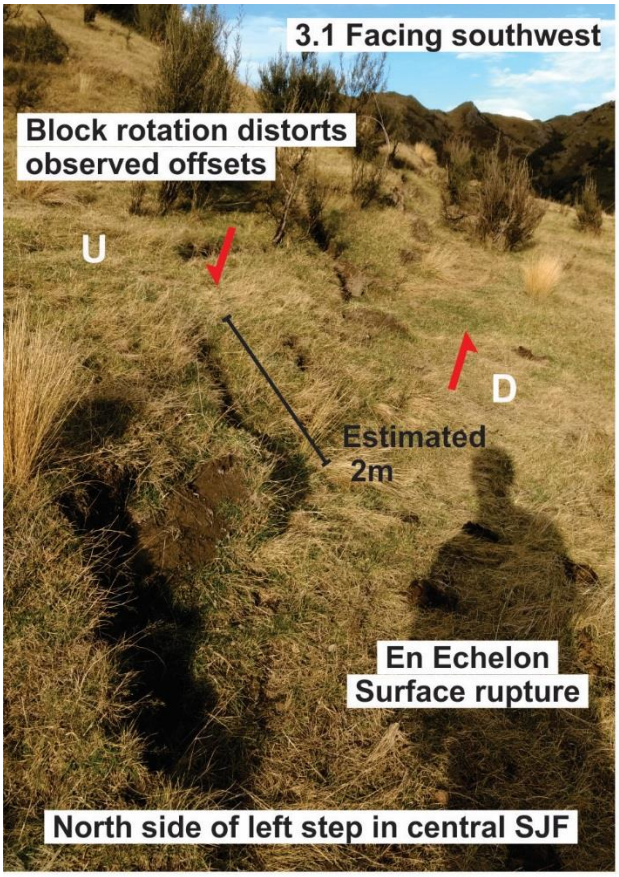
3.1 Facing southwest
Block rotation distorts observed offsets
U
D
Estimated 2m
En Echelon Surface rupture
North side of left step in central SJF

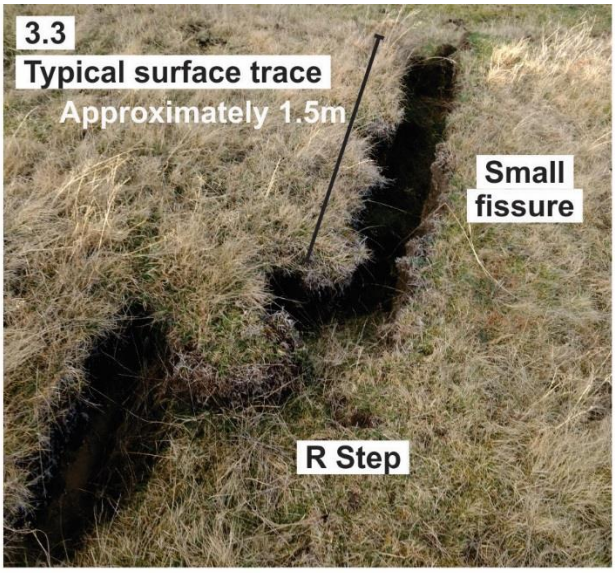
3.3
Typical surface trace
Approximately 1.5m
Small fissure
R Step


3.4
A boulder as an unconventional lateral strain marker (used for estimates)


3.2
One of many gravitational faults that were not mapped

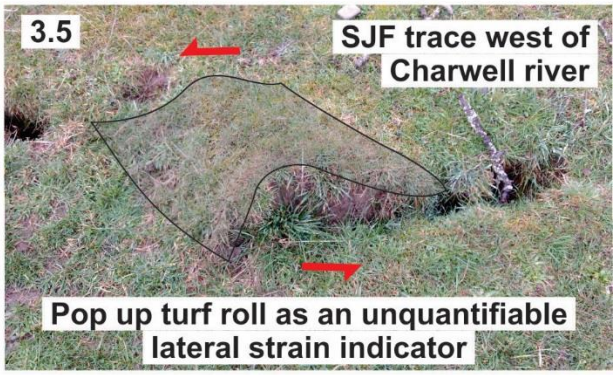
3.5
SJF trace west of Charwell river
Pop up turf roll as an unquantifiable lateral strain indicator


3.6
Landslide dam


4.1
Sinistral offset of a fence

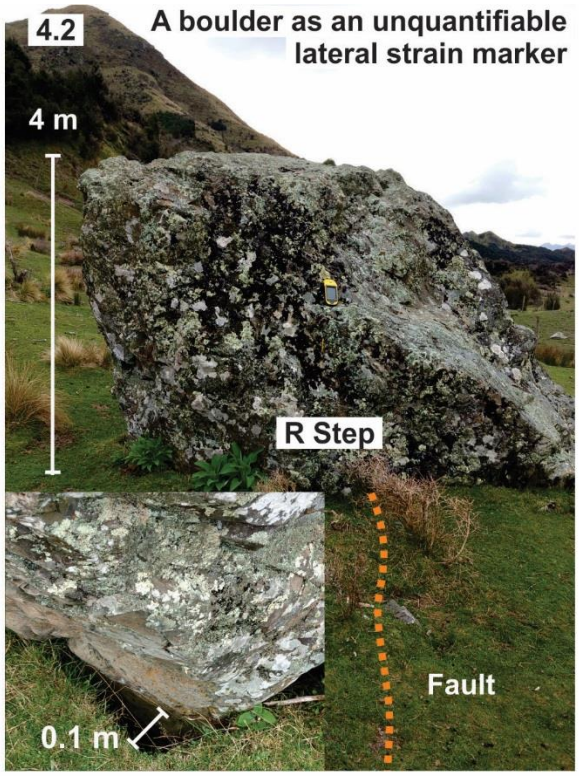
4.2
A boulder as an unquantifiable lateral strain marker
4 m
R Step
Fault
0.1 m


4.3
The few forested areas offered opportunities to try match roots to quantify lateral displacement


4.3
Matching root found
Cobbles were also matched to indents in exceptional circumstances


5.1
Estimated location of large secondary fault not sampled

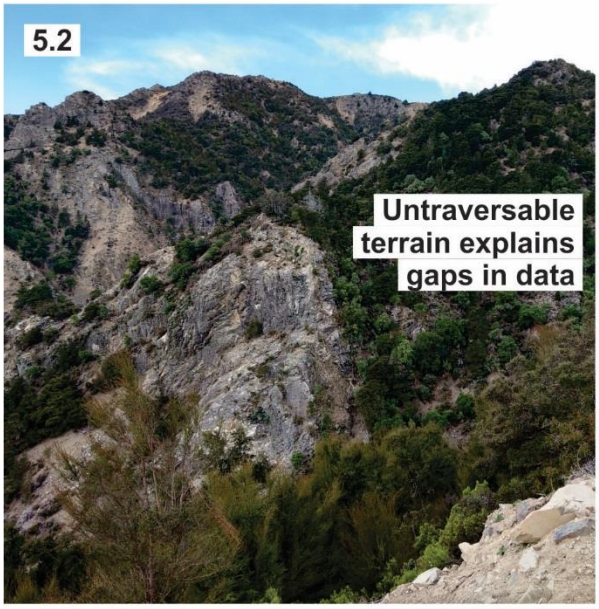
5.2
Untraversable terrain explains gaps in data


5.3
Untraversable scrub fit only for goats


5.4
Good quality acess road in the main valley of the central section


Trench 1
Facing north

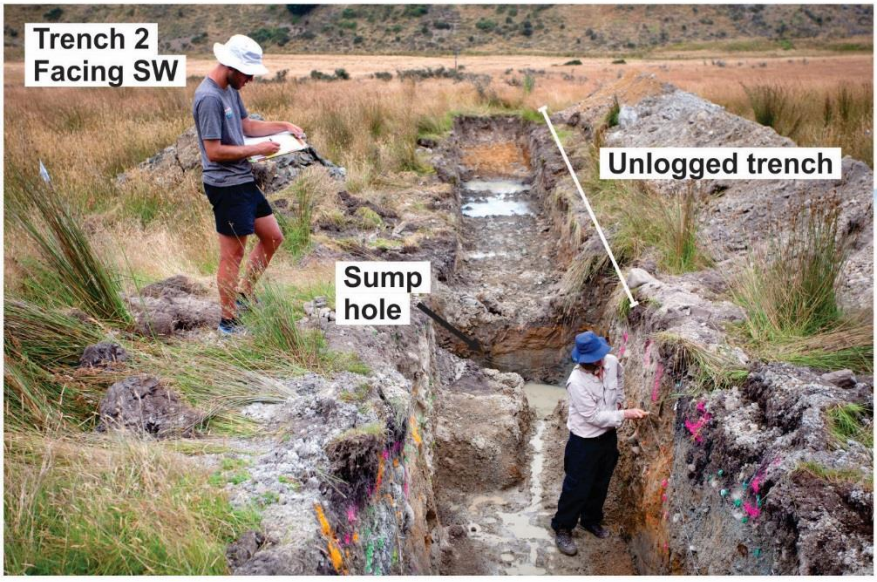
Trench 2
Facing SW
Unlogged trench
Sump
hole


Trench 2
Facing SW


Trench 1
Andy Nicol and me
taking a OSL sample

Appendix 2 - Field data

Below is a summary of key data collected in this study. It does not include previous data points, data sampled from remote sensing, descriptive notes, or derived and calculated values. All samples are sorted north to south and contain a name assigned in the field and an Id relating to their georeferenced linear feature. A '?' denotes a high level of uncertainty regarding the observation. Not all data was used poor quality measurements were kept as estimates for reference. Sample with questionable method or featured measured have 'est' short for estimate beside them.

ID	Fault Name	Maximum Scarp height	Average scarp height	Date	Primary/ secondary fault	L/R Lateral	Horizontal offset	Vertical offset	Feature offset is measured from	Down-thrown quadrant	trace surface geometry	Strike
124	SJF11.2			15/08/2018	p				diverted stream	N	none	SEE
38	SJF11			15/08/2018	p					N	none	SEE
120	SJF10.5			15/08/2018	p					NE	none	SE
122	SJF10.4		20	15/08/2018	p						Continuous	
34	SJF10.3	35	30	15/08/2018	p	L	34	10	Tree roots	NE	Continuous	SE
33	SJF10.2	1.1	20	15/08/2018	p	L	110	20	Fence buckles (est)	W	Continuous	N
32	SJF10.1		5	15/08/2018	s	R?	10?	5?	estimate	E		SE
31	SJF10	40	30	15/08/2018	p	R	30	5	buckled steps (est)	?	R stepping	SE
114	SJF18.1			17/08/2018	p			10	scarp	S		NW
110	SJF18			17/08/2018	p	L		15?	none	NE	R step En Echelon Rollover	SE
98	SJF18.2	55	35	17/08/2018	p	L	15	35	H Fence post angle.	N	Continuous	SE
128	SJF18.3	45	30	17/08/2018	s			40	scarp	S	L Step	NW
98	SJF18.4	60	40	17/08/2018	p	L		40	scarp	N		SW
99	SJF19			17/08/2018	p							
132	SJF20			17/08/2018	p	L		25	Est	NE	R Step En echelon push up	NW
59	SJF21	70	50	17/08/2018	p	L	45	65	Stock Track	W	Continuous	S
132	SJF21.1		25	17/08/2018	p	L	5	25	estimate	W	R step En Echelon	S
59	SJF	80	60	17/08/2018	p			60	estimate	W	R step	S
56	DM2		25	27/09/2018	p	L		25	Scarp trace geo	SW	R step en echelon	S
105	SJF		25	17/08/2018	p	L		25	scarp	W		S
148	DM3		25	27/09/2018	p	L		25	Scarp	W	Parallel segments and blocks	S
54	DM4		35	27/09/2018	p	L	35		road cut	W	multiple segments (4)	S
62	SJF24t		50	17/08/2018	p			50	scarp	W	Continuous parallel ruptures	S
126	SJF24b		15	17/08/2018	p	L		15	scarp	E	R step Continuous parallel ruptures	N
62	SJF24	60	35	17/08/2018	p	L		55	scarp	W	Continuous parallel ruptures	S

ID	Fault Name	Maximum Scarp height	Average scarp height	Date	Primary/ secondary fault	L/R Lateral	Horizontal offset	Vertical offset	Feature offset is measured from	Down-thrown quadrant	trace surface geometry	Strike
61	SJF24.1	110	80	17/08/2018	p	L	105	90	fixed fence post	W	Continuous parallel ruptures	S
150	DM5			27/09/2018	p	L		15	Scarp	SW		S
45	DM6 river ridge		40	27/09/2018	p	L	32	25	animal track	SW	continuous	S
15	SJF6.2	25	20	27/07/2018	s			20	scarp height	NE	L Stepping	SE
16	SJF6	30	8	27/07/2018	s	R	40	30	pop ups fence stay	NW	L stepping En Echelon	NNE
16	SJF6.1		10	27/07/2018	s	R		10	pop ups	NW	L stepping	NNE
66	DM6 shed			27/09/2018	p	L		20	stream bank	W	continuous en echelon R stepping	S
93	SJF15			16/08/2018	s							S
152	DM7			27/09/2018	p	L		35	Scarp	W	r stepping - continuous	S
92	SJF14			16/08/2018	s	L	15	15	Wobbly fence. Est Vert	E	Large 3m Rollover	S
95	SJF17	70	45	16/08/2018	p	L	40	45	Deer Fence	SW	R step En Echelon continuous	SE
94	SJF16		5	16/08/2018	s	L	35	5	Wobbly fence? scarp	W	R step En Echelon	N
67	DM8	50	40	27/09/2018	p	L	31	32	roots	W		S
29	SJF14.1			16/08/2018	s	L		25?	scarp height	E	trampled	N
100	SJF13			16/08/2018	s	L	15?	10?	Estimate - inaccurate	E	rollover & En Echelon R step	S
27	SJF12	30	25	16/08/2018	s	L	6	25	root	W	Continuous parallel ruptures	N
153	DM2.2		80	28/09/2018	p	R	65	80	Roots	W	Continuous	S
1	DM2.1		60	28/09/2018	s	R		60	scarp height	SW	L stepping continuous	S
71	DM2.3		45	28/09/2018	p	L	40	45	fence	W	Continuous	S
82	DM2.4		45	28/09/2018	p	L		45	ridge (Calculated)	SW	Continuous	S
136	DM2.7	58	40	28/09/2018	s	R		45	scarp	W	multiple segments, continuous	S
72	DM2.5			28/09/2018	p	L	100	30	scarp	W	Continuous	S

ID	Fault Name	Maximum Scarp height	Average scarp height	Date	Primary/ secondary fault	L/R Lateral	Horizontal offset	Vertical offset	Feature offset is measured from	Down-thrown quadrant	trace surface geometry	Strike
80	DM2.6		30	28/09/2018	p	L				W	Continuous	S
57 90	DM1		10	27/09/2018	p	L	10	10	boulder 3x4m	W	Continuous	S
76	SJF9	65	55	1/08/2018	p	R	20	65	Roots	NE	Continuous	SE
140	SJF8	25	5	1/08/2018	s	L	5	25	Scarp, Roots	SW	L Steps	NW
25	SJF7	40	30	27/07/2018	s	R	45	40	road	N	Continuous	E
131	SJF1.1		45	26/07/2018	p	L		45	scarp	S	Continuous, L step	SE
87	SJF1	110	95	26/07/2018	p	L	40	95	Cobbles Roots	SW	Continuous, L step	SE
143	SJF5	20	15	27/07/2018			0	0		N	Continuous	
18	SJF2	20		26/07/2018	s	L		20	scarp height	S	L stepping	E
88	SJF1	110	55	26/07/2018	p	L		55	Cobbles Roots	SW	Continuous, L step	SE
19	SJF1	80		26/07/2018	p	L		60	Cobbles Roots	SW	Continuous, L step	SE
89	SJF4	30	20	27/07/2018	p	L?		20	scarp	SW	R steps	NW
144	SJF3.3	15	12	27/07/2018	p	R	13	10	Cobble	NW	L stepping	NE
144	SJF3.2	20	15	27/07/2018	p	R		15	Estimate of fold	NW		NE
144	SJF3.1	10	5	26/07/2018	p	R		8	Estimate of fold	N	L stepping	E
144	SJF3	8	5	26/07/2018	p	R		5	scarp	N	L stepping	SEE
96	14.x			16/08/2018	s					NE	NONE	SE

Appendix 3 – OSL dating lab report

As the SJF was one of several faults that ruptured in 2016 to be trenched, the following report contains several samples not relevant to this study. WLL1368 was collected from trench 2 and WLL1369, WLL1370, WLL1371, were taken from trench 1 as described in Chapter 4. All other samples can be disregarded for the purposes of this study. The report was included in this thesis to provide important information on the techniques used to generate the OSL dates presented. It was produced by Ningsheng Wang from the VUW OSL Dating Laboratory.

Report No. 8/19

Luminescence Dating Technical Report

Luminescence Dating Laboratory
School of Geography, Environment and Earth Sciences
Victoria University of Wellington
Wellington
New Zealand

Reported by: Ms. Ningsheng Wang
Date of Issue: 14-06-2019
Contact: Room 414
Cotton Building
Victoria University of Wellington
Ph: (04) 463 6127

CONTENTS

1. **Summary** **3**
2. **Sample Preparation** **3**
3. **Measurements** **4**
4. **Results** **7**
5. **References** **9**

1. SUMMARY

Ten samples (Field code: SJS-1, SJM-01, SJM-02, SJM-03, C-3, C-4, ATK-19 OSL P1-1, ATK-19 OSL P2-1, HRS-19 OSL P1-1 and DML-19 P4-1) were submitted for luminescence dating by Prof. Andy Nicol, University of Canterbury. The laboratory codes of the samples are WLL1368-WLL1377 respectively.

The fine grain (4-11µm) preparation technique was used. The blue luminescence was measured during infrared stimulation of fine grain feldspar. The luminescence ages were determined by Single Aliquot Regenerative method (SAR). The dose rate was determined based on gamma spectrometry measurements.

2. SAMPLE PREPARATION

The sample preparation consisted of two parts:

(i) Preparation for measurement of equivalent dose (equivalent to the paleodose)

(ii) Preparation for measurement of dose rate

Part 1: The Preparation for Measurement of Equivalent Dose (D_e)

1. Chemical Treatment

Samples had their outer surfaces removed. Of this removed outer scrapings, 100g was weighed and dried in an oven in preparation for gamma spectrometer analysis.
A plastic cube was then filled with remaining scrapings in preparation for water content measuring.

"Fresh" sample material, that had outer surfaces removed earlier (unexposed light sample material), was treated in 10% HCl. This was carried out overnight until all carbonate was removed by the reaction. Following this treatment, the sample was further reacted overnight with 10% H_2O_2 in order to remove organic matter.

The next step involved 200ml CBD* solution being added to the sample for 12 hours to remove iron oxide coatings. Note, after every chemical treatment procedure distilled water was used to wash the sample several times.

*CBD solution: 71g sodium citrate, 8.5 g sodium bicarbonate, and 2g sodium dithionate per litre of distilled water

2. Fine Grain Technique (4-11µm)

After chemical treatment, calgon solution (1g sodium hexametaphosphate per litre distilled water) was added to make thick slurry. This slurry was placed into an ultrasonic bath and mechanically agitated for an hour. The sample was then placed into a 1L measuring cylinder, filled with a certain amount of distilled water to separate out the 4-11µm grains according to Stokes' Law.

The 4-11µm grains were then rinsed with ethanol and acetone and a suspension of these grains were then deposited evenly onto 70 aluminium disks.

Part 2: The Preparation of Measurement of Dose Rate

The dry, ground and homogenised sample material were weighed and sealed in air tight perspex containers and stored for at least four weeks. This storage time minimizes the loss of the short-lived noble gas ^{222} Rn and allows ^{226}Ra to reach equilibrium with its daughters ^{214} Pb and ^{214} Bi.

3. MEASUREMENTS

Luminescence age was determined by two factors: the equivalent dose (D_e) and the dose rate.

Equivalent dose: obtained from the lab equivalents to the paleodose absorbed by samples during the burial time in the natural environment since their last exposure to the light.
Dose rate: amount dose received by the sample each year.

Part 1: Determination of Equivalent Dose (D_e)

D_e was obtained by using SAR.

Single Aliquot Regenerative Method (SAR)

The Single Aliquot Regenerative Method (SAR) was used to determine the equivalent doses. This technique is described by Murray and Wintle (2000).

For the SAR method, a number of aliquots (disks) were subjected to a repetitive cycle of irradiation, preheating and measurement. Firstly, natural shining down curves was measured after preheating. Then shining down curves were measured for the next four or five cycles for different beta doses. Then from the variety of shining down curves, a luminescence growth curve (β induced luminescence versus added dose) was established. This was used to determine the equivalent dose (equivalent to the palaeodose). The measurement for the aliquots resulted in a variety of equivalent doses, so called dose distribution. D_e given in the report were used the arithmetic mean of the data.

In order to correct potential sensitivity changes from cycle to cycle, the luminescence response to a test dose was measured after preheat between cycles.

The blue luminescence of 12 aliquots of each sample (excluding WLL1373, which had 8 aliquots) were measured at 50^0C for 100s using a Riso TL-DA-20 reader with infrared diodes at 880nm used to deliver a stimulated beam. Blue luminescence centre about 410nm from feldspar was then detected by an EMI 9235QA photomultiplier fixed behind two filters consisting of a Schott BG39 and Kopp5-58. Beta irradiation were done on the Riso TL-DA-20 ^{90}Sr/Y β irradiator, calibrated against ^{60}Co gamma source, SFU, Vancouver, Canada with about 3% uncertainty. Preheat and cut heat temperature were chosen to be 260 ^{o}C for 10 seconds. According to Huntley's fading test (Huntley and Lamothe, 2001), no fading tendency was observed.

Luminescence growth curve (β induced luminescence intensity versus added dose) was constructed by using the initial the first a few seconds of the shine down curves

and subtracting the average of the last 20 seconds, along with the so-called late light which was thought to be a mixture of background and hardly bleachable components. Interpolation of this growth curve to the dose axis was yielded the equivalent dose D_e which was used as a paleodose. The measurements of 12 or 8 aliquots obtained 12 or 8 D_e's, the D_e's were accepted within 10% recycling ratio. D_e used for the age determination was used the arithmetic means of the data. A dose recovery test and a zero dose were checked no anomalies.

a-value

a-value is measured by comparing the luminescence induced by alpha irradiation with that induced by beta or gamma irradiation. The a-value was for dose rate calculation. For this study, a- value was estimated.

Part 2: Determination of Dose Rate

Dose rate consisted of two parts.
(i) Dose rate from sample's burial environment
(ii) Dose rate from cosmic rays.

(i) *Dose rate from burial environment*

Dose rate from sample's burial environment was determined by radionuclide contents of ^{238}U, ^{232}Th and ^{40}K, a-value and water content.

Determination of Contents of U, Th and K by Gamma spectrometry

Gamma rays produced from sample material was counted for a minimum time of 24 hours by a high resolution and broad energy gamma spectrometer. The spectra were then analysed using GENIE2000 software. The contents of U, Th and K were obtained by comparison with standard samples. The dose rate calculation was based on the activity concentration of the nuclides ^{40} K, ^{208}Tl, ^{212}Pb, ^{228} Ac, ^{214} Bi, ^{214}Pb, ^{226} Ra, using dose rate conversion factors published by Guérin, G., Mercier, N., Adamiec, G. 2011.

Measurement of Water Contents

Water content was measured as weight of water divided by dry weight of the sample taking into account a 25% uncertainty.

(ii) ***Dose rate from cosmic rays***

Dose rate from cosmic rays were determined by the depth of sample below the surface along with its longitude, latitude and altitude, convention formula and factors published by Prescott, J.R. & Hutton, J.T. (1994).

4. RESULTS

Table 1 Cosmic dose rates

Table 2 Water contents, radionuclide contents

Table 3 a- Values, equivalent doses, dose rates and luminescence ages

Table 1: Cosmic Dose Rates

Laboratory Code	Depth Below the Surface(m)	Cosmic Dose Rate (Gy/ka)	Field Code
WLL1368	1.1	0.1913±0.0096	SJS-1
WLL1369	1.3	0.1865±0.0093	SJM-01
WLL1370	1.65	0.1778±0.0089	SJM-02
WLL1371	0.8	0.1998±0.0010	SJM-03
WLL1372	1.7	0.1785±0.0089	C-3
WLL1373	2.0	0.1715±0.0086	C-4
WLL1374	1.0	0.1890±0.0094	ATK-19 OSL P1-1
WLL1375	1.0	0.1891±0.0095	ATK-19 OSL P2-1
WLL1376	0.5	0.2015±0.0101	HRS-19 OSL P1-1
WLL1377	1.2	0.1826±0.0091	DML-19 P4-1

Table 2: Water Contents, Radionuclide Contents

Laboratory Code	Water Content (%)	U(ppm) from ^{234}Th	U(ppm) from ^{226}Ra, ^{214}Pb, ^{214} Bi	U(ppm) from ^{210}Pb	Th(ppm) From ^{208}Tl ^{212} Pb ^{228} Ac	K(%)	Field Code
WLL1368	17.9	2.93±0.37	2.27±0.17 /2.76±0.17	3.07±0.30	9.88±0.13	2.10±0.04	SJS-1
WLL1369	20.0	2.46±0.32	2.60±0.16	2.93±0.27	9.66±0.12	2.27±0.04	SJM-01
WLL1370	37.3	3.14±0.41	3.00±0.20	3.43±0.34	11.25±0.14	1.94±0.04	SJM-02
WLL1371	18.0	1.94±0.33	2.54±0.17	2.26±0.28	9.84±0.12	2.05±0.04	SJM-03
WLL1372	21.7	2.44±0.37	2.66±0.19	2.62±0.31	9.27±0.13	2.05±0.04	C-3
WLL1373	24.1	2.67±0.41	2.32±0.20	2.13±0.33	10.22±0.14	2.36±0.05	C-4
WLL1374	19.8	3.48±0.41	2.98±0.20	2.85±0.31	11.57±0.14	1.83±0.04	ATK-19 OSL P1-1
WLL1375	21.2	3.50±0.44	3.72±0.22	3.55±0.35	12.23±0.15	1.81±0.04	ATK-19 OSL P2-1
WLL1376	16.5	2.26±0.39	2.67±0.20	1.74±0.31	8.57±0.13	1.77±0.04	HRS-19 OSL P1-1
WLL1377	20.7	3.00±0.36	2.55±0.17	2.85±0.29	9.97±0.12	1.79±0.04	DML-19 P4-1

Table 3: a-Values, Equivalent Doses, Dose Rates and Luminescence Ages

Laboratory Code	a-values*	D_e (Gy)	Dose Rate (Gy/ka)	**Luminescence Age(ka)**	Field Code
WLL1368	0.06±0.03	76.84±0.42	3.82±0.33	**20.1±1.8**	SJS-1
WLL1369	0.06±0.03	111.49±0.57	3.81±0.33	**29.3±2.5**	SJM-01
WLL1370	0.06±0.03	31.96±0.25	3.25±0.35	**9.8±1.1**	SJM-02
WLL1371	0.06±0.03	16.12±0.17	3.70±0.34	**4.4±0.4**	SJM-03
WLL1372	0.06±0.03	42.63±0.34	3.54±0.32	**12.0±1.1**	C-3

WLL1373	0.06±0.03	484.19±9.12	3.69±0.33	**131.2±12.0**	C-4
WLL1374	0.06±0.03	78.78±0.60	3.74±0.37	**21.1±2.1**	ATK-19 OSL P1-1
WLL1375	0.06±0.03	77.92±0.79	3.96±0.41	**19.7±2.1**	ATK-19 OSL P2-1
WLL1376	0.06±0.03	25.87±0.12	3.44±0.31	**7.5±0.7**	HRS-19 OSL P1-1
WLL1377	0.06±0.03	105.26±0.77	3.39±0.32	**31.1±3.0**	DML-19 P4-1

*a-value is estimated

5. REFERENCES

Guérin, G., Mercier, N. & Adamiec, G. 2011: Dose- rate conversion factors: update. Ancient TL, Vol.29, No.1, 5-8.

Huntley D.J. & Lamothe, M. 2001: Ubiquity of anomalous fading in K-feldspars and the measurement and correction for it in optical dating. Canadian Journal of Earth Sciences.38, 1093-1106.

Murray, A.S. & Wintle, A.G. 2000: Luminescence dating of quartz using an improved single aliquot regenerative dose protocol. Radiation Measurements 32, 57-73.

Prescott, J.R. & Hutton, J.T. 1994: Cosmic ray contributions to dose rates for luminescence and ESR dating: Large depths and long-term time variations. Radiation Measurements. Vol.23,Nos.2/3, 497-500.

Appendix 4 – Radiocarbon dating lab report

Appendix 4 is the radiocarbon lab report which details the specific process and accuracy of each sample. Both samples were dated by the Waikato University Radiocarbon Laboratory. Refer to trench logs in Chapter 4 for locations of samples.

THE UNIVERSITY OF WAIKATO
Te Whare Wānanga o Waikato

Private Bag 3105
Hamilton,
New Zealand.
Ph +64 7 838 4278
email c14@waikato.ac.nz

Wednesday, 3 April 2019

Radiocarbon Dating Laboratory

Report on Radiocarbon Age Determination for Wk- 48973

Submitter	A Nicol
Submitter's Code	SJS-2
Site & Location	Stone Jug Swamp Trench, New Zealand
Sample Material	Soil, organics
Physical Pretreatment	Visible contaminants removed.
Chemical Pretreatment	Washed in hot 10% HCl, rinsed and treated with hot 1% NaOH. The NaOH insoluble fraction was treated with hot 10% HCl, filtered, rinsed and dried.

$D^{14}C$	-340.0 ±	1.4 ‰
$F^{14}C$%	66.0 ±	0.1 %
Result	**3337 ± 18 BP**	

(AMS measurement)

Comments

Please note: The Carbon-13 stable isotope value ($\delta^{13}C$) was measured on prepared graphite using the AMS spectrometer. The radiocarbon date has therefore been corrected for isotopic fractionation. However the AMS-measured $\delta^{13}C$ value can differ from the $\delta^{13}C$ of the original material and it is therefore not shown.

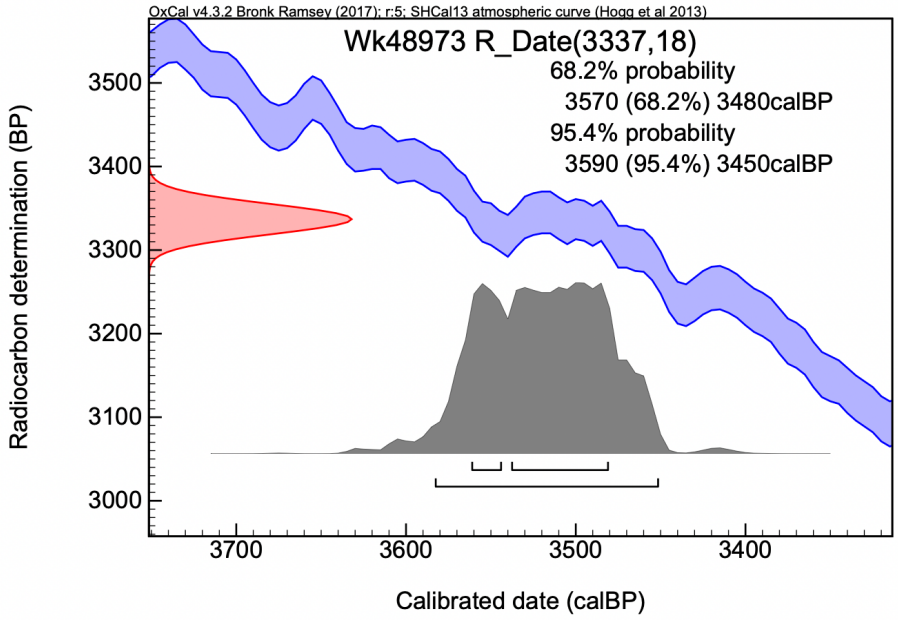

- Explanation of the calibrated Oxcal plots can be found at the Oxford Radiocarbon Accelerator Unit's calibration web pages (http://c14.arch.ox.ac.uk/embed.php?File=explanation.php)
- Result is *Conventional Age or Percent Modern Carbon (pMC)* following Stuiver and Polach, 1977, Radiocarbon 19, 355-363. This is based on the Libby half-life of 5568 yr with correction for isotopic fractionation applied. This age is normally quoted in publications and must include the appropriate error term and Wk number.
- Quoted errors are 1 standard deviation due to counting statistics multiplied by an experimentally determined Laboratory Error Multiplier.
- The isotopic fractionation, $\delta^{13}C$, is expressed as ‰ wrt PDB and is measured on sample CO_2.
- $F^{14}C$% is also known as *Percent Modern Carbon (pMC)*.

THE UNIVERSITY OF WAIKATO
Te Whare Wānanga o Waikato

Private Bag 3105
Hamilton,
New Zealand.
Ph +64 7 838 4278
email c14@waikato.ac.nz

Wednesday, 3 April 2019

Radiocarbon Dating Laboratory

Report on Radiocarbon Age Determination for Wk- 48974

Submitter	A Nicol
Submitter's Code	SJS-3
Site & Location	Stone Jug Swamp Trench, New Zealand
Sample Material	Soil, organics
Physical Pretreatment	Visible contaminants removed.
Chemical Pretreatment	Washed in hot 10% HCl, rinsed and treated with hot 1% NaOH. The NaOH insoluble fraction was treated with hot 10% HCl, filtered, rinsed and dried.

$D^{14}C$	-71.2 ±	2.0 ‰
$F^{14}C$%	92.9 ±	0.2 %
Result	**593 ± 17 BP**	

(AMS measurement)

Comments

Please note: The Carbon-13 stable isotope value ($\delta^{13}C$) was measured on prepared graphite using the AMS spectrometer. The radiocarbon date has therefore been corrected for isotopic fractionation. However the AMS-measured $\delta^{13}C$ value can differ from the $\delta^{13}C$ of the original material and it is therefore not shown.

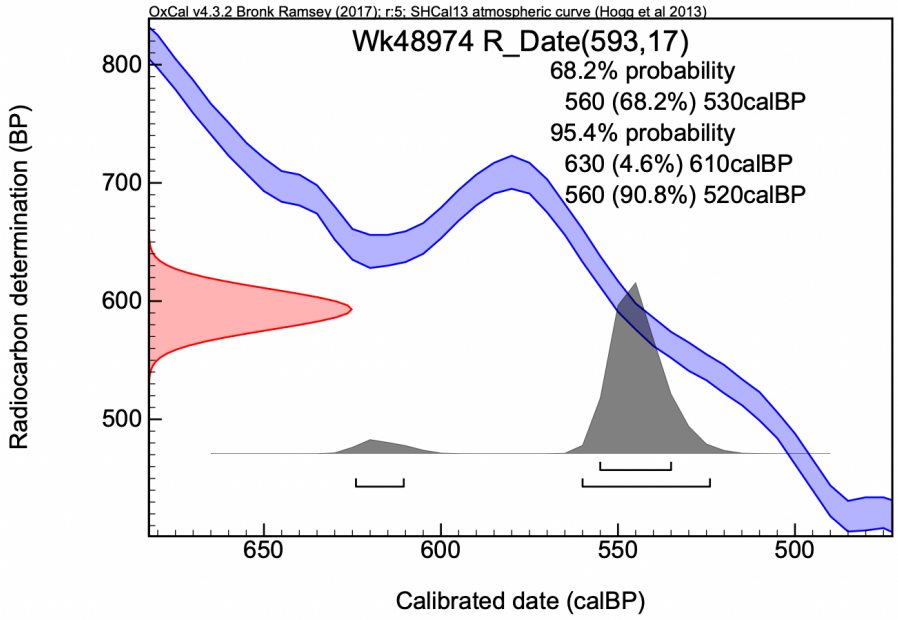

- Explanation of the calibrated Oxcal plots can be found at the Oxford Radiocarbon Accelerator Unit's calibration web pages (http://c14.arch.ox.ac.uk/embed.php?File=explanation.php)
- Result is *Conventional Age or Percent Modern Carbon (pMC)* following Stuiver and Polach, 1977, Radiocarbon 19, 355-363. This is based on the Libby half-life of 5568 yr with correction for isotopic fractionation applied. This age is normally quoted in publications and must include the appropriate error term and Wk number.
- Quoted errors are 1 standard deviation due to counting statistics multiplied by an experimentally determined Laboratory Error Multiplier.
- The isotopic fractionation, $\delta^{13}C$, is expressed as ‰ wrt PDB and is measured on sample CO_2.
- $F^{14}C$% is also known as *Percent Modern Carbon (pMC)*.

References

Barnes, P.M. (1996). Active folding of Pleistocene unconformities on the edge of the Australian-Pacific plate boundary zone, offshore North Canterbury, New Zealand. *Tectonics.* **15**, 623–640.

Barrell, D.J.A., and Townsend, D.B. (2012). General distribution and characteristics of active faults and folds in the Hurunui District, North Canterbury. *GNS Science.* Report 2012/113.

Barrell, D. J. A., Canterbury, I., and Monitoring, G. (2015). General distribution and characteristics of active faults and folds in the Kaikoura District, North Canterbury. Christchurch. *Environment Canterbury Regional Council.*

Barrell, D., Stirling, M., Williams, J., Sauer, K., and van den Berg, E. (2018). Kaikōura Earthquake: Hundalee Fault paleoseismology. P. 19 In: Sagar, M.; Prebble, J. (Editors). Abstract Volume: Geosciences 2018, Napier, New Zealand. *Geoscience Society of New Zealand Miscellaneous Publication*. **151**. 313.

Berryman K., Cochran, U.A., Clark, K.J., Biasi, G.P., Langridge, R.M., Villamor, P. (2012). Major Earthquakes Occur Regularly on an Isolated Plate Boundary Fault. *Science.* **336,** 1690.

Biasi G.P., and Weldon R.J. (2006). Estimating Surface Rupture Length and Magnitude of Paleoearthquakes from Point Measurements of Rupture Displacement. *Bull. Seismol. Soc. Am*. 1612–1623,

Bronk Ramsey, C. (1995). Radiocarbon Calibration and Analysis of Stratigraphy: The OxCal Program. Radiocarbon. **37**, 425-430.

Brough, T. (2019). Tectonic geomorphology and paleoseismology of the Humps Fault zone, North Culverden basin. (Masters Thesis) *University of Canterbury*. Retrieved from https://ir.canterbury.ac.nz/handle/10092/841

Bull, W. (1991) Geomorphic responses to climatic change. New York, *Oxford University Press*.

Bull, W., and Knuepfer, P. (1987). Adjustments by the Charwell River, New Zealand, to uplift and climatic changes. *Geomorphology*, 15-32, https://doi.org/10.1016/0169-555X(87)90004-3.

Bushell, T. (2019). History, structure and kinematics of The Humps and Leader Fault relays, North Canterbury (working tittle). (PhD Thesis in progress). *University of Canterbury.*

Cesca, S., Zhang, Y., Mouslopoulou, V., Wang, R., Saul, J., Savage, M., Kufner, K., Oncken, O., and Dahm, T. (2017). Complex rupture process of the Mw 7.8, 2016, Kaikoura earthquake, New Zealand, and its aftershock sequence. *Earth Planet. Sci. Lett.* ***478***, 110-120.

Crampton J. (1988). Stratigraphy and structure of the Monkey Face area, Marlborough, New Zealand, with special reference to shallow marine Cretaceous strata. *New Zeal J Geol Geophys.*

Clark, K., Nissen, E.K., Howarth, J.D., Hamling, I.J., Mountjoy, J., Ries, and W. *et a*l. (2017). Highly variable coastal deformation in the 2016 MW7.8 Kaikōura earthquake reflects rupture complexity along a transpressional plate boundary. *Earth Planet. Sci. Lett.*

Coulter, R.F., (2007). Tectonic geomorphology and seismic hazard of the Mt Fyffe section of the Hope Fault. (Masters thesis), *University of Canterbury*. Retrieved from https://ir.canterbury.ac.nz/handle/10092/841

Duputel, Z., and Rivera, L. (2017). Long-period analysis of the 2016 Kaikoura earthquake. *Phys Earth Planet In, **265***, 62–66. doi:10.1016/j.pepi.2017.02.004

Esri. "World Imagery" [basemap]. (2017). Scale Not Given. "World Imagery Map". https://services.arcgisonline.com/ArcGIS/rest/services/World_Imagery/MapServer. (August 25, 2018).

Fumal, T.E., Pezzopane, S.K., Weldon, R.J., and Schwartz, D.P. (1993). A 100-year average recurrence interval for the San Andreas fault at Wrightwood, California. *Science*. **259,** 199-203.

Warren, G. (1995). Geology of the Parnassus area. Lower Hutt: Institute of Geological & Nuclear Sciences. *Institute of Geological & Nuclear Sciences geological.* map 18 36 p.

Hamling, I. J., Hreinsdóttir, S., Clark, K., Elliott, J., Liang, C., Fielding, E., Litchfield, N., Villamor, P., Wallace, L., Wright, T., *et al*. (2017). Complex multi-fault rupture during the 2016 Mw 7.8 Kaikoura earthquake, New Zealand, *Science.* **356**, no. 6334, doi: 10.1126/science.aam7194.

Hornblow S, Quigley M, Nicol A, Van Dissen R, and Wang N. (2014). Paleoseismology of the 2010 Mw 7.1 Darfield (Canterbury) earthquake source, Greendale Fault, New Zealand. *Tectonophysics*. **637**, 178-190.

Howell, A., K. Clark, E. Nissen, T. Stahl, P. Villamor and K. Jones. (2018). 3D Co-seismic offsets during the 2016 Mw 7.8 Kaikoura earthquake from aerial photogrammetry. P. 129 In: Sagar, M.; Prebble, J. (Editors). Abstract Volume: Geosciences 2018, Napier, New Zealand. *Geoscience Society of New Zealand Miscellaneous Publication.* **151**, 313.

Kaiser, A., Balfour, N., Fry, B., Holden, C., Litchfield, N., Gerstenberger, M., D'Anastasio, McVerry, N., Ristau, G., D., Gledhill, K. *et al,* (2017). The 2016 Kaikōura, New Zealand, Earthquake: Preliminary Seismological Report. *Seismological Research Letters.* **88**, 727-739. doi:10.1785/0220170018

Kearse, J., Little, T. A., Van Dissen, R. J., Barnes, P. M., Langridge, R., Mountjoy, J., Reis, W., Villamor, P., Clark, K., Benson, A., Hemphill-Haley, M. *et al,* (2018). Onshore to Offshore Ground-Surface and Seabed Rupture of the Jordan–Kekerengu–Needles Fault Network during the 2016 Mw 7.8 Kaikōura Earthquake, New ZealandOnshore to Offshore Ground-Surface and Seabed Rupture of the Jordan–Kekerengu–Needles Fault Network. *Bull. Seismol. Soc. Am.* **108(3B),** 1573-1595. doi:10.1785/0120170304

Khajavi, N., Langridge, R.M., Quigley, M.C., Smart, C., Rezanejad, A. and Martín-González, F., (2016). Late Holocene rupture behavior and earthquake chronology on the Hope fault, New Zealand. *Geological Soc. Am. Bull.*

Knuepfer, P. L. K. (1984). Tectonic geomorphology and present-day tectonics of the alpine shear system, South Island, New Zealand. (Doctorial Thesis), *The University of Arizona*, Available from Dissertation Abstracts International. **46,** 93.

Knuepfer, P. (1992). Temporal variations in latest Quaternary slip across the Australian-Pacific Plate Boundary, northeastern South Island, New Zealand. *Tectonics.* **11**, 449-464. doi:doi:10.1029/91TC02890

Langridge, R., J. Campbell, N. Hill, V. Pere, J. Pope, J. Pettinga, E. Estrada, and K. Berryman (2003). Paleoseismology and slip rate of the Conway segment of the Hope fault at Greenburn Stream, South Island, New Zealand, Ann. Geophys. **46**, 1119–1139.

Langridge, R., Campbell, J., Hill, N., Pere, V., Pope, J., Pettinga, J., Estrada, J., and Berryman, K. (2003). Paleoseismology and slip rate of the Conway Segment of the Hope Fault at Greenburn Stream, South Island, New Zealand. *Ann. Geophys*. 46.

Langridge, R.M., Ries, W.F., Litchfield, N.J., Villamor, P., Van Dissen, R.J., Barrell, D.J.A., Rattenbury, M.S., Heron, D.W., Haubrock, S., Townsend, D.B., *et al*, (2016). The New Zealand Active Faults Database. *New Zeal J Geol Geophys.* **59**, 86-96. doi: 10.1080/00288306.2015.1112818.

Langridge, R. M., J. V. Rowland, P. Villamor, J. Mountjoy, C. Madugo, D. Townsend, A. Canva, K. Clark, R. J. Van Dissen, W. Ries *et al*., (2018). Geology, co-seismic rupture and slip across the Papatea fault and its role in the 2016 Kaikōura Earthquake, New Zealand., *Bull. Seismol. Soc. Am*.

Litchfield, N. J., R. Van Dissen., Sutherland, Barnes, P., Cox, Norris, Bevan, Landridge, Rob villamor *et al.* (2014). A model of active faulting in New Zealand. *New Zeal J Geol Geophys.*

Litchfield, N. J., Villamor, P., Dissen, R. J. V., Nicol, A., Barnes, P. M., A. Barrell, D. J., Pettinga, J., Langridge, R., Little, T., Mountjoy J., *et al*. (2018). Surface Rupture of Multiple Crustal Faults in the 2016 Mw 7.8 Kaikōura, New Zealand, Earthquake. *Bull. Seismol. Soc. Am*. **108**, 1496–1520. doi: https://doi.org/10.1785/0120170300

Litchfield N.J., Villamor P., Van Dissen R., Nicol A., Barnes P., Barrell D., Pettinga J., Langridge R., Little T., *et al*. Surface ruptures and paleoseismology of the Mw 7.8 2016 Kaikōura earthquake reveal end-member complexity. *Geology* (in review).

Little, T., Van Dissen, R., Kearse, J., Norton, K., Ningsheng, W., (2018). Kekerengu fault, New Zealand: timing and size of Late Holocene surface ruptures. *Bull. Seismol. Soc. Am*. **108,** 1556–1572.

Massiot, C., Seebeck, H., Nicol, A., McNamara, D.D., Lawrence, M.J., Griffin, A.G., Thrasher, G.P., O'Brien, G., and Viskovic, P. (2019). Effects of regional and local stress variations on slip tendency in the southern

Taranaki Basin, New Zealand. *Marine and Petroleum Geology.* **107**, 467-483. doi.org/10.1016/j.marpetgeo.2019.05.030

McCalpin, J.P. (ed.) (2009). Paleoseismology, 2nd Edition: International Geophysics Series, Vol. 95, *Elsevier Publishing.* 647.

McMorran, T. J. (1991). The Hope Fault at Hossack Station east of Hanmer Basin, North Canterbury. (Masters Thesis), *University of Canterbury*. Retrieved from https://ir.canterbury.ac.nz/handle/10092/9947

Meghraoui, M., Philip, H., Albarede, F., and Cisternas, A. (1988). Trench investigations through the trace of the 1980 El Asnam thrust fault. *Bull. Seismol. Soc. Am*. **78,** 979-999.

Mouslopoulou, V., Saltogianni, V., Nicol, A., Oncken, O., Begg, J., Babeyko, A., Cesca, S., and Moreno, M., (2019). Breaking a subduction-termination from top to bottom: the large 2016 Kaikōura Earthquake, New Zealand. *Earth Planet. Sci. Lett.* **506**, 1-10.

Nicol, A., Alloway, B.V., and Tonkin, P.J. (1994). Rates of deformation, uplift and landscape development associated with active folding in the Waipara area of North Canterbury, New Zealand. *Tectonics* **13**, 1321-1344.

Nicol, A., Robinson, R., Van Dissen, R., and Harvison, A., (2016). Variability of recurrence interval and single-event slip for surface-rupturing earthquakes in New Zealand. *New Zeal J Geol Geophys.* **59**, 97-116. doi:10.1080/00288306.2015.1127822

Nicol A., Van Dissen, R., Stirling M., and Gerstenberger, M., (2016). Completeness of the paleoseismic active fault record in New Zealand. *Seismological Research Letters.* **86**, 1299-1310. doi:10.1785/0220160088.

Nicol A., J. Pettinga, C. Fenton, T. Stahl, S. Bannister, K. Pedley, N. Hyland, T. Bushell, I. Hamling, J. Ristau, D. Noble, and S. McColl,. (2018). Preliminary geometry, slip and kinematics of fault ruptures during the 2016 MW 7.8 Kaikōura Earthquake in the North Canterbury region of New Zealand. *Bull. Seismol. Soc. Am.* doi: 10.1785/0120170329

Pettinga, J.R. & Yetton, M.D. & Van Dissen, R.J. and Downes, Gaye. (2001). Earthquake source identification and characterisation for the Canterbury Region, South Island, New Zealand. *Bull. New Zeal. Soc. Earthq. Eng*. **34,** 282-317.

Pope, J.G., (1994). Secondary structures, Holocene displacements and paleoseismicity of the Conway segment of the Hope Fault, Greenburn Stream to Sawyers Creek. BSc (Hons) thesis, *University of Canterbury*.

Ramsey, C. B. (1995). Radiocarbon calibration and analysis of stratigraphy: the OxCal program. *Radiocarbon*. ***37***, 425-430.

Rattenbury, M. S., D. B. Townsend, and M. R. Johnston (2006). Geology of the Kaikōura area, *Institute of Geological & Nuclear Sciences* 1:250,000 Geological Map 13, 1 sheet + 70 pp., GNS Science, Lower Hutt, New Zealand.

Shi, X., Wang, Y., Liu-Zeng, J., Weldon, R., Wei, S., Wang, T., and Sieh, K. (2017). How complex is the 2016Mw 7.8 Kaikoura earthquake, South Island, New Zealand?. *Science Bulletin.* ***62***, 309-311. doi:https://doi.org/10.1016/j.scib.2017.01.033

Sibson, R., F. Ghisetti, and J. Ristau (2011). Stress control of an evolving strike-slip fault system during the 2010–2011 Canterbury, New Zealand, earthquake sequence, *Seismol. Res. Lett.* **82**, 824-832.

Sieh, K. E. (1978). Prehistoric large earthquakes produced by slip on the San Andreas Fault at Pallett Creek, California, *J. Geophys. Res.*, **83**, 3907– 3939,

Stirling, M.; Gerstenberger, M.; Litchfield, N.; McVerry, G.; Smith, W.; Pettinga, J. and Barnes, P. (2007). Updated probabilistic seismic hazard assessment for the Canterbury region. Prepared for Canterbury Regional Council, CRC Report No. U06/6.

Stirling, M., McVerry, G., Gerstenberger, M., Litchfield, N., Van Dissen, R., Berryman, K., Barnes, P., Wallace, L., Villamor, P., Langridge, R., *et al*. (2012). National Seismic Hazard Model for New Zealand: 2010 Update. *Bull. Seismol. Soc. Am.* **102**: 1514–1542,

Stirling, M. W., N. J. Litchfield, P. Villamor, R. J. Van Dissen, A. Nicol, J. Pettinga, P. Barnes, R. M. Langridge, T. Little, D. J. A. Barrell*, et al*. (2017). TheMw 7.8 Kaikōura earthquake: Surface rupture, and seismic hazard context, *Bull. New Zeal. Soc. Earthq.* Eng. **50**, 73–84.

Stein, R., A. Barka, and J. Dieterich, (1997). Progressive failure on the North Anatolian Fault since 1939 by earthquake stress triggering. *Geophys. J. Int.* **128**, 594-604.

Vanderleest, R.A., D.M. Fisher, D.O.S. Oakley, and T.W. Gardner (2017). Growth and seismic hazard of the Montserrat anticline in the North Canterbury fold and thrust belt, South Island, New Zealand, J. *Struct. Geol*. **101**, 1-14.

Van Dissen, R. J. (1989). Late Quaternary faulting in the Kaikoura region, southeastern Marlborough, New Zealand. (Masters Thesis), Available from Oregon State University ScholarsArchive@OSU database.

Wang, T., Wei, S., Shi, X., Qiu, Q., Li, L., Peng, D., Weldon, R., and Barbot, S. (2018). The 2016 Kaikōura earthquake: Simultaneous rupture of the subduction interface and overlying faults. *Earth Planet. Sci. Lett.* **482**, 44-51. doi:https://doi.org/10.1016/j.epsl.2017.10.056

Weldon, R., Scharer, K., Fumal, T., and Biasi, G., (2004). Wrightwood and the earthquake cycle: what a long recurrence record tells us about how faults work. *GSA Today.* **14**.

Williams, J. N., D. J. A. Barrell, M. W. Stirling, K. M. Sauer, G. C. Duke, and K. X. Hao (2018). Surface rupture of the Hundalee fault during the 2016 Mw 7.8 Kaikōura earthquake, *Bull. Seismol. Soc. Am.*

Woods, R., McBride, S., Wotherspoon, L., Beavan, S., Potter, S., Johnston, D., Wilson, T., Brunsdon, D., Grace, E., Becker, J. *et al* (2017). Science to emergency management response: Kaikōura earthquakes 2016, *Bull. New Zeal. Soc. Earthq.* Eng. **50,** 329-337.